Integration of aeromagnetic data, borehole hyperspectral measurements and ASTER satellite images for 3D geological modelling in the Omaheke region, Namibia

JONATHAN ALEXANDER FRANCO HEMPENIUS
February, 2018

SUPERVISORS:
Prof.Dr.Mark van der Meijde
Dr. Harald van der Werff

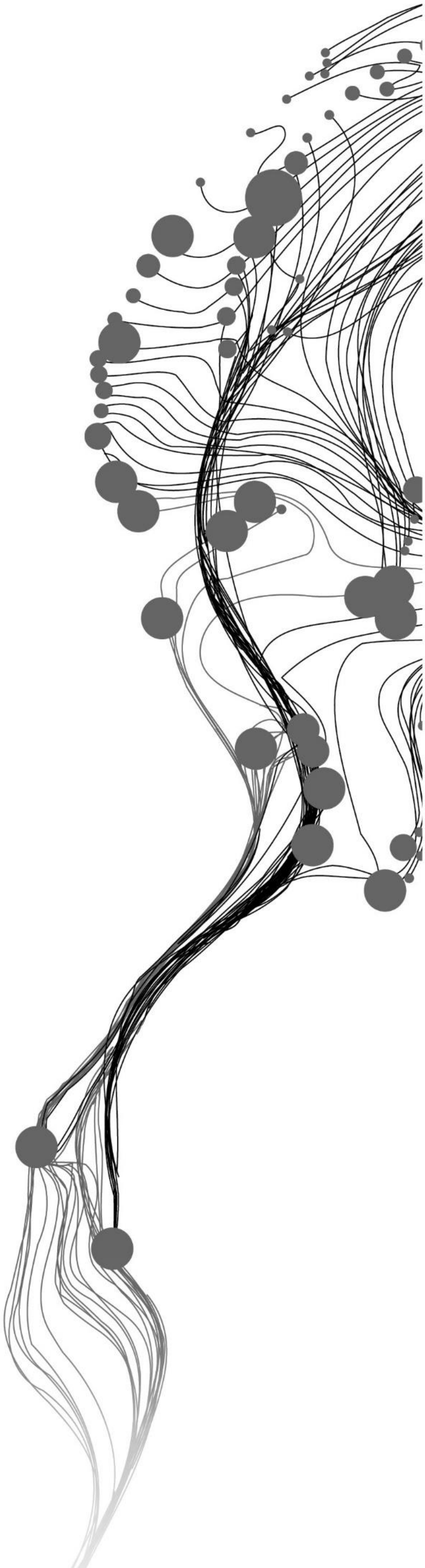

Integration of aeromagnetic data, borehole hyperspectral measurements and ASTER satellite images for 3D geological modelling in the Omaheke region, Namibia

JONATHAN ALEXANDER FRANCO HEMPENIUS
Enschede, The Netherlands, [February, 2018]

Thesis submitted to the Faculty of Geo-Information Science and Earth Observation of the University of Twente in partial fulfilment of the requirements for the degree of Master of Science in Geo-information Science and Earth Observation.
Specialization: Applied Earth Sciences

SUPERVISORS:
Prof.Dr.Mark van der Meijde
Dr. Harald van der Werff

THESIS ASSESSMENT BOARD:
Prof.Dr. Freek van der Meer (Chair)
Dr. Mike Buxton (External Examiner, Technical University of Delft)

DISCLAIMER
This document describes work undertaken as part of a programme of study at the Faculty of Geo-Information Science and Earth Observation of the University of Twente. All views and opinions expressed therein remain the sole responsibility of the author, and do not necessarily represent those of the Faculty.

ABSTRACT

3D geological modelling helps to understand geological structures that control mineral and hydrocarbon deposits. Typically, surface geology data and subsurface geophysical data are combined with drill core logging to obtain a 3D geological model. For currently unexplored areas that have a high mineral resource potential, such as Namibia it would be useful to assess how the available datasets could be integrated and to determine their added value for 3D geological modelling. However, much of the country lacks such a detailed geological mapping. The Geological Suervey of Nambia has therefore developed what they call *"implicit"* 3D geological model in Omaheke region. This *"implicit"* model was developed with the available 1:250.000 geological maps, digital terrain model, borehole logs and processed geophysical data to model the different lithological units that are underlying the Kalahari Tertiary cover. However, the use of geophysical data to obtain subsurface information, such as aeromagnetics is limited by the principle of non-uniqueness. This leads to an ambiguity in the interpretation of the subsurface, therefore there is a need of using surface data obtained from multi- and hyperspectral images and gamma-ray surveys in conjunction with drill core logging. Therefore, an iterative joint interpretation was done ASTER satellite image and aeromagnetic data sets in conjunction with laboratory VNIR-SWIR spectral measurements from borehole samples and analyse the added value of integrating different datasets for 3D geological modelling study area located in Omaheke region. Four data sets where processed to evaluate if integrating gives an added value for 3D geological modelling. The first dataset is a pre-processed aeromagnetic data that is the total magnetic intensity with a spatial resolution of 50 meters. The second dataset consists of geological and mineral maps on a scale of 1:1.500.000 developed by the GSN in 1998. The third dataset consists of spectral measurements made in 2017 on eight boreholes that where drilled between 1994 and 1995. These boreholes where made for water exploration, therefore the samples consist only of chips that represent a larger interval. The description logs as well as the borehole samples were provided by the Geological Survey of Namibia. The fourth dataset consists of cross talk corrected level 2B ASTER images taken between 2002 and 2008. For ASTER images and borehole measurements a total of 13 band ratios, proposed by Cudahy (2012) where produced. For the hyperspectral borehole measurements, a total of 11 band ratio combinations and for ASTER images a total of 3 band ratio combinations were done to be able to visualize which combinations could be more useful to highlight lithological changes. With 3D Euler deconvolution a total of 20 depth range maps where produced. During the processing four values of structural index (SI) were used: 0, 0.25, 0.5 and 0.75 and the Euler solutions where divided into different depth ranges 70-130m, 90-150m, 110-170m and 130-190m. Regarding the integration between borehole spectral measurements and aeromagnetic data, it appeared not to be possible to integrate these datasets as there is no clear pattern in the borehole data that allows to distinguish between the Kalahari group and the Damara groups through band ratio combinations. For the aeromagnetic data, to validate which of the depth range maps best fits to the study area, it was decided to use only the boundary between the Kalahari and the Damara group that is described in the borehole log descriptions, since the borehole band ratios did not provide any additional information of the lithological boundaries. Based on this information, it was concluded that the best depth map that fits these data is the one processed using a structural index of 0 and a depth range between 70-130m.

ACKNOWLEDGEMENTS

I want to thank my supervisors, Mark van der Meijde and Harald van der Werff, for their guidance and support throughout the development of this research and for the encouragement to always improve my work. Without out them this would not have possible.

I am grateful, to John-Paul Mubita and Nortin Titus, from the Geological survey of Namibia for their support when visiting Namibia, and for helping me in the process of acquiring the data provided by the Geological Survey of Namibia. This thesis would not have been possible without their support.

I am grateful to Rob Hewson, for his help and guidance for the interpretation of the ASTER images thought the development of this research.

Finally, my greatest thanks to my family: my mother, Maija, my father, Rodolfo and my sister, Paloma for always supporting, loving me and encouraging me to always push myself further. I would not have reached this far without your enormous support.

TABLE OF CONTENTS

LIST OF FIGURES

LIST OF TABLES

1. INTRODUCTION

1.1. Problem statement

3D geological modelling helps to understand geological structures that control mineral and hydrocarbon deposits (Wang et al., 2011). "The type of data integrated within a 3-D model depends on data availability, density, and distribution, as well as project objectives and working scale" (Fallara et al., 2006). Typically, surface geology data and subsurface geophysical data are combined with drill core logging to obtain a 3D geological model. Surface geology is obtained by combing fieldwork data with satellite and airborne remote sensing data. Fieldwork data involves field mapping and drill core logging. Remote sensing data involves the interpretation of multi- and hyperspectral satellite/airborne images, aerial photographs and airborne geophysical data.

Multi- and hyperspectral images are frequently used in mineral exploration. This technique allows geologists to generate mineral and lithological maps, by looking at key absorption features of various minerals that are spectrally active within the VNIR, SWIR and IR spectrum (Mielke et al., 2016; van der Meer et al., 2012). Such maps aid geologists in the identification of mineralization vectors and geological structures, to establish if there is a suitable area where mineralizations might have occurred (Gandhi & Sarkar, 2016). In the United States, the Cuprite mining region in Nevada is a well-known hydrothermal deposit that has been extensively studied with multispectral and hyperspectral images. Here, it was possible to identify different alteration zones by obtaining the spatial distribution of iron-bearing minerals, micas and clay minerals (Swayze et al., 2014). In Spain, in the Rodalquilar caldera complex, HyMap images where used in combination with field spectral measurements to improve the characterization of the different mineral alteration zones in the Rodalquilar epithermal gold deposit (Bedini et al., 2009).

For areas that have a complex structural geology, multi- and hyperspectral images are often combined with aeromagnetic data, to allow the visualization and interpretation of geological structures such as faults, dikes or lineaments. Such structures are often characterized by a lower or higher magnetic susceptibility and differences in the mineralogical composition of lithological units (Belocky et al., 1997). Aeromagnetic data can also be used to measure changes of magnetic properties at depth by using inversion methods. However, this method for obtaining subsurface data is limited by the principle of non-uniqueness, as each sub-surface structure displays a field that closely resembles the measured field (Baptiste et al., 2016; Chen et al., 2007). This leads to an ambiguity in the 3D interpretation of the subsurface. Therefore, it is useful to cross check aeromagnetic data and surface data form multi- and hyperspectral images with borehole logging. This technique provides information on the different composition of the rocks and their variation with depth. Borehole data are particularly useful in the interpretation of aeromagnetic data, allowing to cross check the aeromagnetic data (Baptiste et al., 2016; Finn & Morgan, 2002).

Remote sensing and geophysical data for geological modelling has been utilized for the characterization of different types of mineral deposits around the world. In the Panorama district, Australia, hyperspectral images and the K channel from the gamma ray images were used to map hydrothermal alterations in VMS deposits, distinguishing areas which have Al-poor and Al-rich white mica and have enrichment or depletion of potassium. This allowed to identify discharge and recharge areas that characterize these types of deposits (Tex, 2006). In the Broken Hill, Cobar and Wagga Wagga areas in Australia, ASTER images and geophysical data were used for identifying different lithological units, regolith and mineralization zones. Here, aeromagnetic data provided information to identify the geological structures that control the mineral deposits (Hewson et al., 2003, 2005; Hewson & Robson, 2014). In the Rocklea Inlier Iron Ore, Australia, it was possible to obtain a coherent pattern between drill cores and Hymap images. This allowed to identify advanced argillic alteration and phyllic alteration zones from the deposit and to develop a 3D subsurface map of the area (Cudahy & Thomas, 2016). In the Luchan Ore region in China, they successfully surface geology and drill core logging in conjunction with magnetic and gravitational data merged to develop a 3D geological model (Chen et al., 2007). In Central Nigeria aeromagnetic and pseudogravity data was processed using 3D Euler deconvolution to identify the structures that might have caused rich mineralization within the pegmatite rich zones (Olawuyi et al., 2016).

According to the afore mentioned examples the combination of remote sensing, field and borehole data provide valuable information of the geology in an area to generate a 3D geological model, which can be used for mineral exploration. For currently unexplored areas that have a high mineral resource potential, such as Namibia (Eberle et al., 1995) it would be useful to assess how the available datasets could be integrated and to determine their added value for 3D geological modelling. The Geological Survey of Namibia (GSN) has made geological maps on a scale of 1:2500.000 that cover almost the entire country. In addition, the survey also has aeromagnetic data that covers approximately 85% of the country. Although the GSN has a large amount of data, but not all has been processed for 3D geological modelling. In addition, the geological map at a scale of 1:2500.000, is not sufficiently detailed to carry out 3D geological modelling. In some areas in Namibia, like the western margin of the Kalahari desert, ASTER images have been interpreted to improve the geological detail (Gomez et al., 2005). However, much of the country lacks such a detailed geological mapping. The GSN has therefore developed an what they call *"implicit"* 3D geological model in Omaheke region (pers. Comm. Joh-Paul Mubita, Geological Survey of Namibia). This *"implicit"* model was developed with the available 1:250.000 geological maps, digital terrain model, borehole logs and processed geophysical data to model the different lithological units that are underlying the Kalahari Tertiary cover(Burney et al., 2015). However, the use of geophysical data to obtain subsurface information, such as aeromagnetics is limited by the principle of non-uniqueness (Baptiste et al., 2016; Chen et al., 2007). This leads to an ambiguity in the interpretation of the subsurface, therefore there is a need of using surface data obtained from multi- and hyperspectral images and gamma-ray surveys in conjunction with drill core logging. Furthermore, the borehole data used, was interpreted for water exploration and not mineral exploration. As a result, only chips where recovered from the drilling and the logs lack a detailed description of the lithology. Therefore, the current *"implicit"* 3D geological model requires further study of the surface as well as the borehole logs to be able to determine if these data sets can provide further information to improve the 3D modelling. Furthermore, it would be useful to evaluate how these different datasets integrate with each other, by doing an iterative joint interpretation. This iterative joint interpretation consists of interpreting each dataset by taking into account the different interpretation of the other datasets. This could possibly determine if one dataset can aid in the interpretation of another dataset. Since using the 3D Euler deconvolution method on the aeromagnetic data does not require *a priori* knowledge of the geology in the area to locate the depth of the source of the magnetic anomalies. Different depth range maps can be produced. These depth range maps can be then compared with the results obtained from the band ratios of the ASTER images and the spectral measurements at different depths from the available boreholes. By comparing with different might aid in the determination of some variable required for the 3D Euler deconvolution, like for example the structural index or windows size.

The geology is mainly comprised of metamorphic and sedimentary rocks which are product of the amalgamation between the Kalahari craton and the Congo-Sao Francisco craton (Frimmel et al., 2011; Miller, 2008). These rocks display a variation of strongly magnetic and non-magnetic lithologies. Also, these rocks are composed of minerals that belong to the AlOH, MgOH and ferric oxide groups which are active within the VNIR and SWIR ranges. This means that, in this area, it would be useful to integrate aeromagnetic data with the multispectral data to characterise surface geology. A combination of ASTER, airborne geophysical data sets can be used in conjunction with VNIR-SWIR and geophysical measurements from the borehole samples to correlate surface and subsurface data.

1.2. Objectives and research questions

1.2.1. General objective

The objective of this study is to make a joint interpretation of ASTER satellite image and aeromagnetic data sets in conjunction with laboratory VNIR-SWIR spectral measurements from borehole samples and analyse the added value of integrating different datasets for 3D geological modelling study area located in Omaheke region.

1.2.2. Specific objectives

- Generate lithological geological maps of the study area based on multispectral images in combination with aeromagnetic data.
- Compare the band ratios in the VNIR and SWIR wavelength regions between the ASTER images and the hyperspectral drill core measurements.
- Compare the depth estimates of the 3D Euler deconvolution of aeromagnetic data with changes of lithology in the borehole data.

1.2.3. Research questions

- Is it possible to relate hyperspectral signatures obtained with a field spectrometer on drill cores with the multi-spectral signatures obtained from multispectral images?
- Are there lithological units that are not distinguishable on the surface or underground through spectral signatures or through magnetic anomalies?
- What are the differences between depth estimates from the 3D Euler deconvolution and the depth of change in lithology from the borehole data?
- Does the use of band ratios on the spectral measurements from the boreholes provide additional geological information that 3D Euler deconvolution does not provide?

1.3. Study area

The Omaheke study area is located in the western part of Namibia, between longitude 19.7°E to 20.1°E and latitude 19.7°S to 21°S (Figure 1). Geologically, the study area is located in the Damara Belt, which is comprised of metamorphic and sedimentary rocks resulting from the merging of the Kalahari craton and the Congo-Sao Francisco craton (Frimmel et al., 2011). According to the 1:1.500.000 geologic map (Andritzky et al., 1998), these stratigraphic units are only exposed in the north-eastern part of the study area, and the rest of the area is covered by sands from the Tertiary Kalahari Group. The rocks that comprise the Damara Belt are composed of minerals that belong to the AlOH, MgOH, and ferric oxide groups which are active within the VNIR and SWIR ranges. Also, they display a variation of strongly magnetic and non-magnetic lithologies (Miller, 2008).

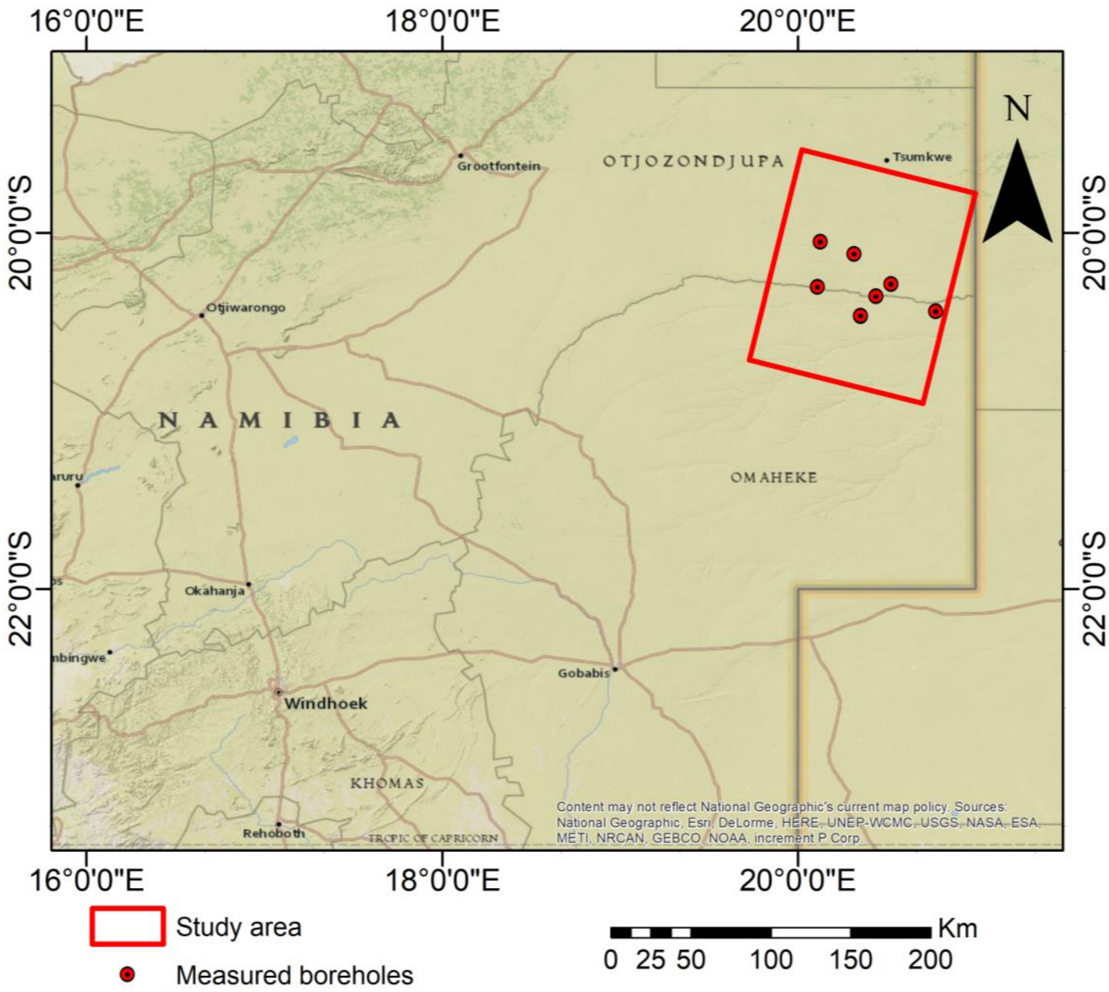

Figure 1. Study area (14208 Km^2) within the Omaheke region, Namibia.

2. DATA AND METHODOLOGY

2.1. Data

Four data sets where processed to evaluate if integrating gives an added value for 3D geological modelling. The first dataset is a pre-processed aeromagnetic data that is the total magnetic intensity with a spatial resolution of 50 meters. This dataset was provided by the Geological Survey of Namibia and was collected in 1994 during a geophysical campaign the was carried out throughout the entire country. The second dataset consists of geological and mineral maps on a scale of 1:1.500.000 (Figure 2) which where developed by the geological survey of Namibia in 1998. The third dataset consists of spectral measurements made in 2017 on eight boreholes that where drilled between 1994 and 1995 (Figure 2). These boreholes where made for water exploration, therefore the samples consist only of chips that represent a larger interval. The description logs as well as the borehole samples were provided by the Geological Survey of Namibia. The fourth dataset consists of cross talk corrected level 2B ASTER images taken between 2002 and 2008, acquired from the metadata and service discovery tool Reverb, developed by the NASA (https://reverb.echo.nasa.gov/reverb).

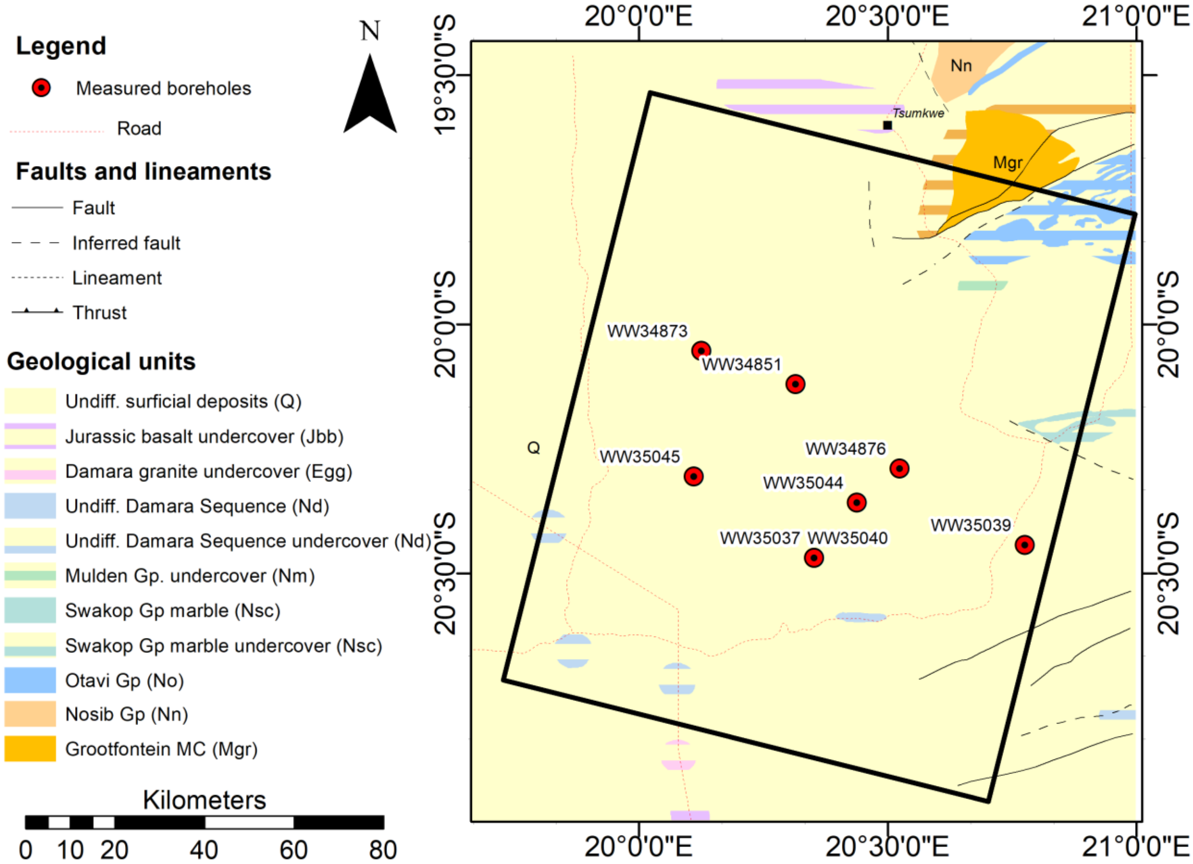

Figure 2. Location of the measured boreholes and mineral map 1:1.000.000 (modified from Andritzky et al., 1998)

2.2. Methodology

The methodology is divided into 2 stages: The first is the data processing of the ASTER images, airborne geophysical data and the drill core logging data. The second stage is data integration where all data sets are combined to evaluate their added value for 3D geological modelling.

2.2.1. Data processing

2.2.1.1. Spectroscopy on boreholes

Hyperspectral measurements were carried out in the Geological Survey of Namibia facilities using the ASD Terraspec HALO, which makes measurements of 2150 bands within the VNIR and SWIR wavelength ranges. To ensure a representative spectrum of each borehole sample, a total of three measurements where done and then averaged. The average spectra were resampled to the spectral resolution of the ASTER sensor. Following the resampling, band ratios defined by Cudahy, 2012 where calculated for each collected sample so that they can be compared with the satellite ASTER band ratios Cudahy, 2012. Finally, different band ratios where combined based on the suggestion made by Cudahy, 2012 and through visual inspection of the band ratio graphs, to select the band ratios that provide the best contrast between the two geological units (Kalahari group and Damara group).

2.2.1.2. ASTER band ratios and lithological maps

All available level 2 crosstalk corrected ASTER surface reflectance and emissivity products between 2002 and 2008 where displayed in false colour composite and green vegetation content was calculated. Subsequently, the images with least cloud content were selected and green vegetation content band ratio product (Table 1) was calculated for each image (Figure 3) to be able to select the images with least green vegetation content. The images that met these requirements previously stated where taken on 30/04/2002 and 28/08/2005 (Figure 4).

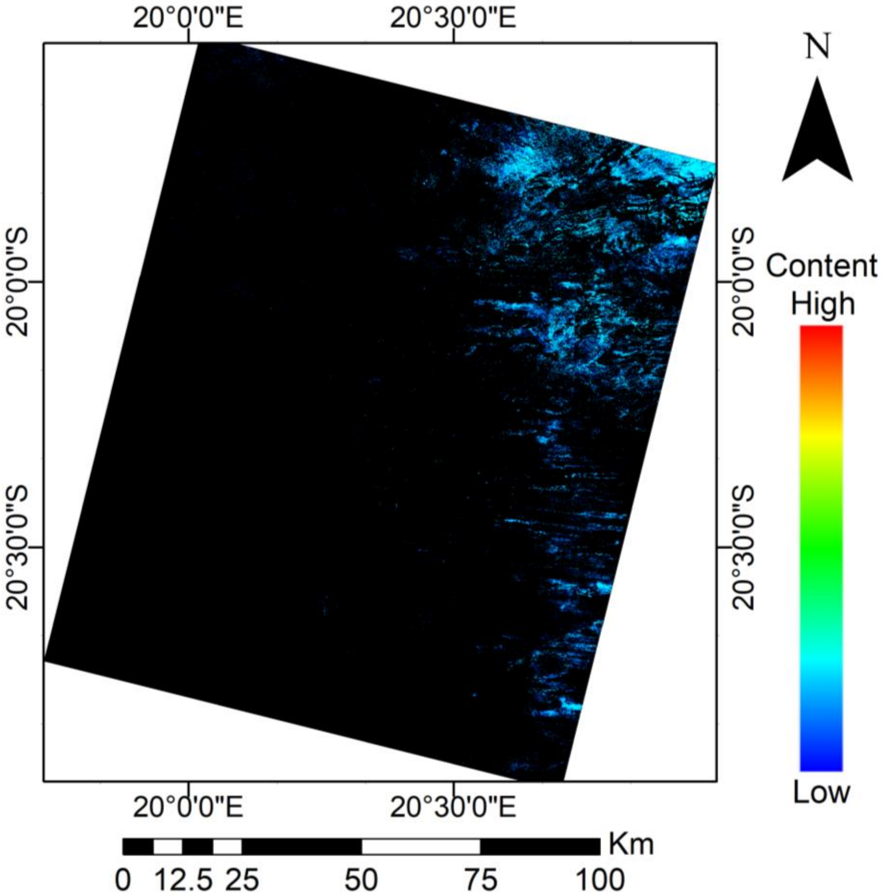

Figure 3. Green vegetation content band ratio on 30/04/2002 and 28/08/2005 ASTER images from the study area.

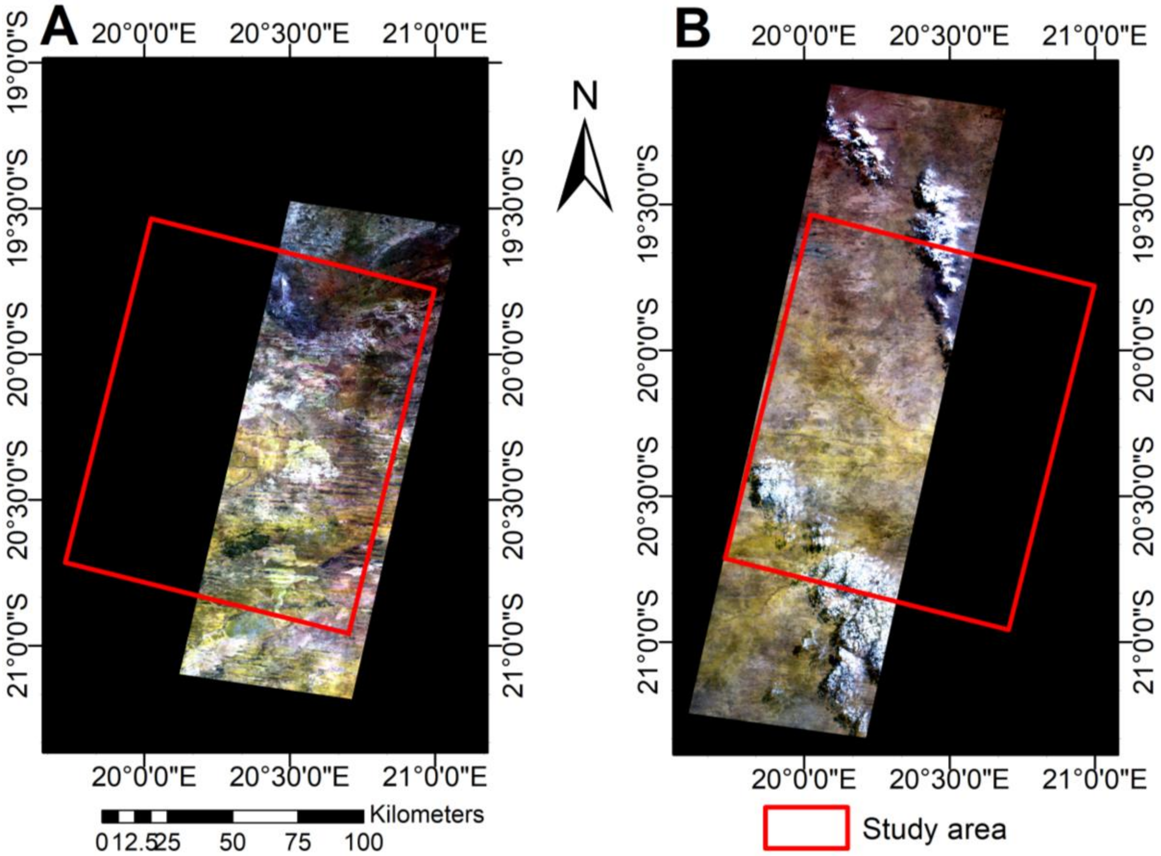

Figure 4. False colour composite (3N,2, 1) ASTER images. A) Images taken in 30/04/2002 and B) images taken in 28/08/2005. Notice the presence of clouds only occurs in the ASTER scene captured in 2005.

Once the ASTER images were selected, SWIR bands 4 to 9 were resampled from 30 meter pixel resolution to 15 meter resolution so that all 9 bands within the VNIR and SWIR wavelengths can be stacked. Although according to Cudahy, 2012 the three bands from VNIR should be resampled to 30 meter pixel resolution. But when resampling these bands to 30 meter pixel resolution, a diagonal stripping in the images appeared, which affected all the band ratios that where generated. However, in this study is was not analysed what was the cause of this stripping. The next processing step was to remove anomalies that were caused by thick cloud tops and low albedo areas such as deep shadows, by masking them. This was only done on the mosaic of the ASTER scenes taken in 2005, since these where the ones to contain some cloud cover. To remove clouds and cloud shadows the following procedure was carried out:

1. Using ENVI, a region of interest (ROI) was created using band 1 and band 4 thresholds: For the cloud cover, band 1 threshold was set so that the maximum reflectance is 250 and for cloud shadows band 4 threshold was set so that the minimum reflectance is 250.
2. Since these thresholds do not cover the edges of the clouds, a buffer zone of 150 pixels surrounding the ROI was generated, the resulting raster file would be used to create a mask in which it excludes all pixel that are 150 pixels or less from these buffer zone in the ASTER scenes from 2005 (Figure 5).

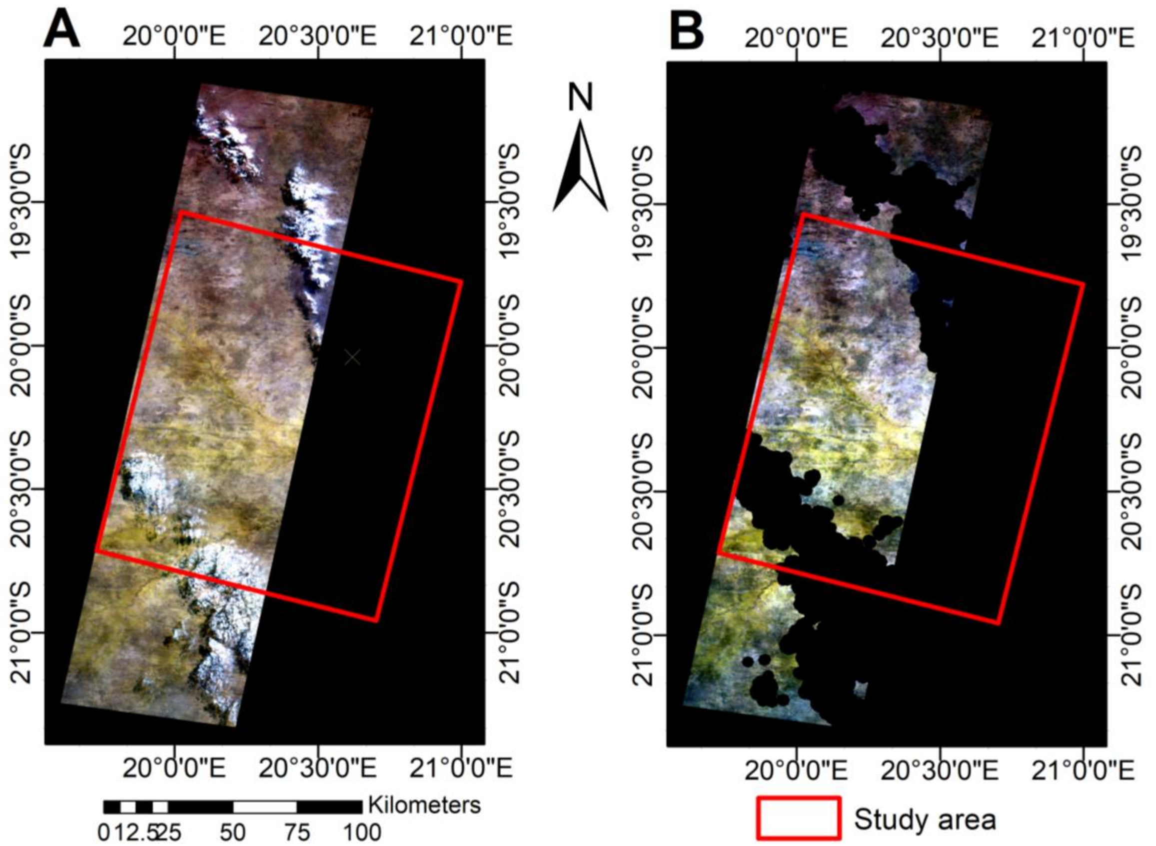

Figure 5. A) 2005 ASTER false colour composite (3N,2,1) without masking. B) 2005 ASTER false colour composite (3N, 2, 1) with clouds and cloud shadows masked.

Once clouds and cloud shadows were masked, the ASTER scenes from 2002 and 2005 were mosaicked. To differentiate lithological units at the surface, band ratios of the ASTER images were created. Various band ratios have been suggested to map mineral abundance and mineral composition. For each band ratio of Ferrous iron index, AlOH group composition, Kaolin group index, FeOH group content, MgOH group content, MgOH group composition and Ferrous iron in MgOH, a green vegetation mask vas applied (Table 1) to remove any false anomalies. Also, for the compositional band ratios of each mineral group a mask of the content band ratio of each mineral group was applied in other to include in the pixels that are above the low content threshold. Also for each histogram stretch parameters (Table 1)(Cudahy, 2012). Finally, ER mapper software was used to create RGB image with the different band ratio image products to generate different maps that show spatial contrast in mineralogy and lithology. ER Mapper is chosen over ENVI as it allows a better histogram stretching option for each of the band ratios.

2.2.1.3. 3D Euler deconvolution

Since there is no detailed information on the geology in the study area, it is required a technique that doesn't require an *a priori* knowledge of the geology but is able to use the existing aeromagnetic data to obtain information of the geology in the subsurface. Such technique is known as 3D Euler deconvolution, developed by Reid et al. (1990) which is an extension of Euler deconvolution for profile data developed by Thompson (1982). The technique developed by Reid et al., (1990) allows to generate a 2D grid which contains the location and depth estimates of magnetic anomalies that satisfies Euler's homogeneity equation (Equation 1) (Thompson, 1982). In this equation (Equation 1) x_0, y_0 and z_0, are the position of magnetic source, B is the regional value of the total field, and T is the total field detected at an x, y and z location. In Euler's homogeneity equation the N value corresponds to the structural index, which Ried et al. (1990) defines as "a measure of the rate of change with distance of a field". For further information on 3D Euler deconvolution the reader is referred to Reid et al. (1990) and Thompson (1982).

$$(x - x_0)\frac{\delta T}{\delta x} + (y - y_0)\frac{\delta T}{\delta y} + (z - z_0)\frac{\delta T}{\delta Z} = N(B - T) \qquad (1)$$

The standard 3D Euler deconvolution processing was done using Oasis Montaj 9.3 (20171105.126) (http://www.geosoft.com), which is a semiautomatic process. This method "uses a least squares method to solve Euler's equation simultaneously for each grid position within a sub-grid (window). A square window, say 10 by 10, is moved along each grid row. At each grid point there will be 100 equations (for a 10 by 10 window), from which the four unknowns (location X, Y, Z, and a background value B) and their uncertainties (standard deviations) are obtained for a specified structural index" (Geosoft, 2018). The input file is the grid of the total magnetic intensity of the study area. This is used to calculate to calculate the X, Y and Z derivates (**Error! Reference source not found.**) which will be used as input for solve the 3D Euler equation.

Name	Algorithm	Mask	Stretch (min, max)
Green vegetation content	B3/B2	none	Linear (1.4-4.0)
Ferric oxide content	B4/B3	none	Linear (1.1-2.1)
Ferric oxide composition	B2/B1	ferric oxide content>1.05	Gaussian (0.5-3.3)
Ferrous iron index	B5/B4	green vegetation content<1.75	Linear (0.75-1.025)
Opaque index	B1/B4	B4<260	Linear (0.4-0.9)
AlOH group content	(B5+B7)/B6	none	Linear (2.00-2.25)
AlOH group composition	B5/B7	green vegetation content<1.75+AlOH content>2.0	Gaussian (0.9-1.3)
Kaolin group index	B6/B5	Green vegetation<1.4	Linear (1.0-1.125)
FeOH group content	(B6+B8)/B7		Linear (2.03-2.25)
MgOH group content	(B6+B9)/(B7+B8)		Linear (1.05-1.2)
MgOH group composition	B7/B8	Green vegetation<1.4+MgOH content>1.06	Equalisation (0.6-1.4)
Ferrous iron in MgOH	B5/B4		Equalisation (0.1-2.0)
Silica index	B13/B10	none	Linear (1.0-1.35)

Table 1. ASTER Band ratio products, with masks and histogram stretch values for each band ratio (adapted from Cudahy, 2012)

Besides the X, Y and Z derivatives, two more variables are required to solve Euler's equation. These are the Structural index (SI) and the window size. The structural index (SI) corresponds to a measurement of the rate of change in relation with the distance from the magnetic field. The structural index value can vary between 0 and 3. The SI is determined by type of geological features we are interested in mapping. Since the purpose of the study is to locate contacts between geological units, a SI value between 0 and 1 must be selected, where 0 is for completely horizontal boundaries and 1 to completely vertical boundaries. Since there is no accurate knowledge of which type of contact are present in the study area different values of SI where used: 0, 0.25, 0.5 and 0.75 to calculate the Euler solution and determien during the integration phase which SI best fits for the study area. The window size determines the depth range at which solutions can be calculated. The window size must be small enough to not include solutions that are affected from surrounding sources, and has to be big enough to an adequate variant of the field. For this study a window size of 3x3 pixels was used, which corresponds to a size of 150x150m.

Once the 3D Euler solution was calculated, a filtering (windowing) of the solutions has to be applied, since the software produces calculates all the possible solution even if they are on a greater distance from the window size. The following parameters where used to filter (window) the Euler solutions:

1. Depth to a maximum of 350 meters.
2. X and Y offsets maximum of 50 meters
3. Location uncertainty (dXY) to a maximum of 5%.
4. Percentage depth uncertainty maximum of 5%.

The maxim depth was set to include a few meters more than the maximum depth of the 8 boreholes within the study area. The x and Y offsets refer on the distance from which these solutions are from the centre of the search window. Since the resolution of the aeromagnetic data is 50 meters, it was determined that for this study to limit the solution to be no greater than 50 meters away from the centre of the search window. The case for depth and location uncertainties, according to Reid (1990) this must be the lowest value possible, but without filtering too many of the solutions. Therefore, a value of 5% uncertainty was considered the optimal value in which removed most of the solution but keeping enough solutions to be able to use kriging to generate the depth range maps.

Once the windowing of the Euler solution is done, the Euler solution can be gridded using kriging. However, since some solutions with different depth may be close together, this is difficult to determine the depth of the different contact present in the area. To solve this, a further filtering of the solutions was carried out to limit solutions in different depth ranges: 0-350, 70-130, 90-150, 110—170, 130-190. This allow to generate through kriging different depth range maps which allow a better visualization of the different geologic contacts.

2.2.2. Data integration

For data integration, the interpretations from each individual dataset will be analysed in relation to other available datasets. Borehole band ratio combinations which have a high contrast between lithological units were be compared with identical RGB band ratio combinations from the ASTER images. This is to determine if borehole spectral measurements can be used to help produce more accurate band ratio combination for developing lithological maps. For the aeromagnetic data, the different depth range maps were compared with the borehole band ratio interpretation borehole logs to determine which parameters for calculating the 3D Euler deconvolution best fit these datasets. Once these datasets have been compared to each other, it will be discussed if by combining these they provide additional information for 3D geological modelling instead of looking individually at each dataset.

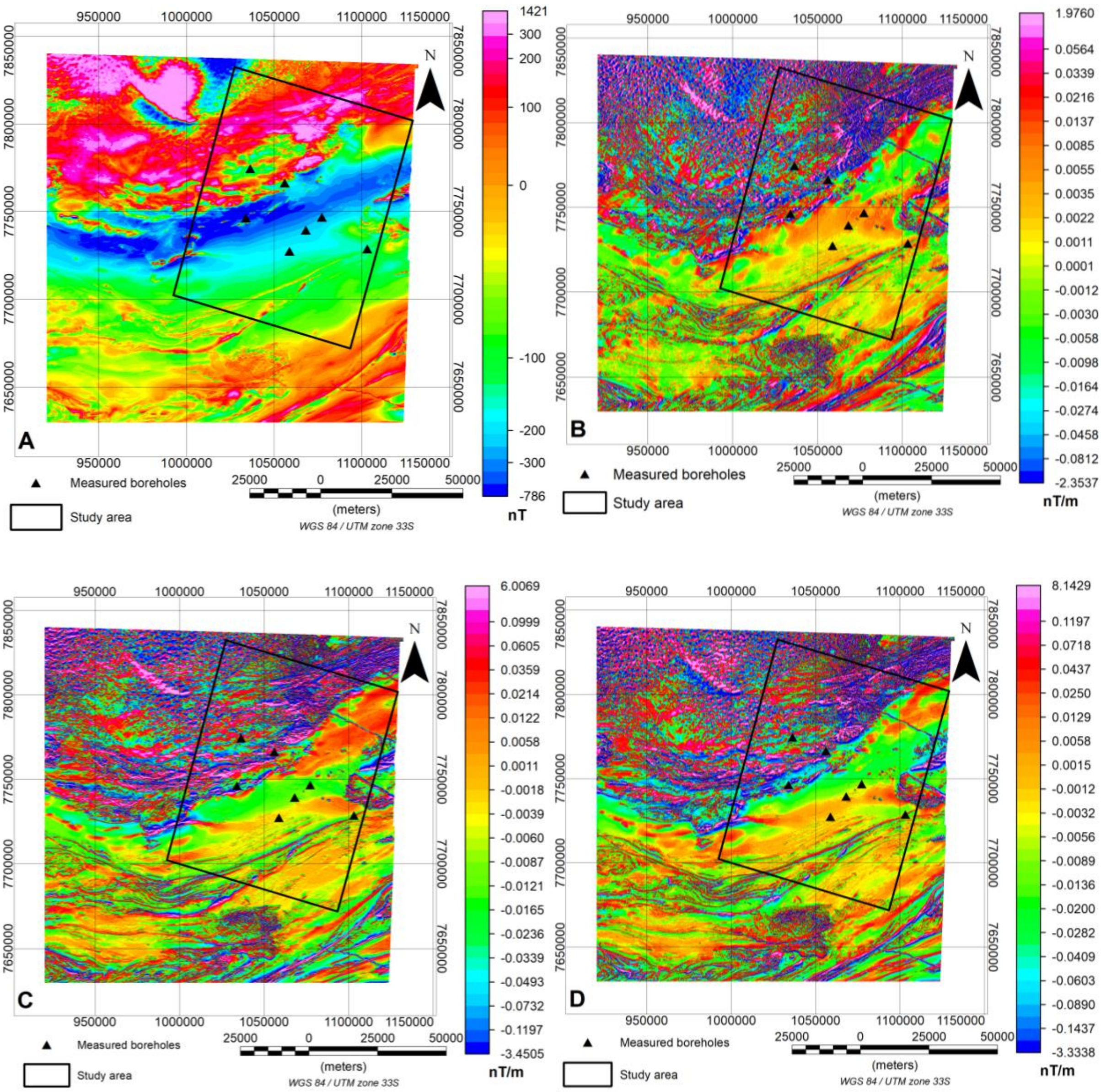

Figure 6. Total magnetic intensity and input maps to the 3-D Euler deconvolution equation: A) Total magnetic intensity, B) X derivative, C) Y derivative and D) Z derivative.

3. RESULTS

3.1. Borehole spectroscopy

For the spectroscopy measurements a total of 8 boreholes were measured. The samples are comprised of recovered chips, as the main goal of the drilling was for water exploration, and not mineral exploration. The maximum depth and the number of samples (Table 2) and interval at which each sample was taken varied for each borehole (Annex 1: Borehole log descriptions, Annex 2: Borehole resampled spectral measurements tables and Annex 3: Borehole band ratio combination graphs)

Borehole code	Depth (m)	# of samples	Interval of lithological change according to Log description (m)
WW34851	221	15	2
			113
WW34873	250	7	68
			91
			175
WW34876	363	21	2
			32
WW35037	201	29	5
			32
			81
			181
WW35039	191	13	29
WW35040	205	21	32
			83
			185
WW35044	110	11	10
			45
			103
WW35045	116	10	19
			45
			104

Table 2. Borehole depths, number of samples and depth of lithological boundaries. Cell highlighted in red mark the lithological boundary between the Kalahari and Damara groups according to the borehole description logs.

As stated in the methodology section, using the ASD spectra that were resampled to ASTER band definitions, band ratios were calculated (Annex 1) taking into account the indices suggested by Cudahy (2012) (Table 1), with the exception of the green vegetation index and silica index. The green vegetation content was not calculated as none of the sample contain any vegetation, and for the silica index could not be calculated as the ASD Terraspec HALO does not measure in the thermal infra-red wavelengths.

To compare the band ratios calculated from the ASD Terraspec with the band ratios ASTER RGB band, ratio combinations band ratio combination graphs where created, using the proposed combinations by Cudahy (2012). But instead three band ratios, two band ratios were displayed together in relation to the depth (Annex 3). Through the log description of each borehole (Annex 1) each lithological boundary (Table 2) was graphed in each band ratio combination. A total of 11 band ratio combinations were done to be able to visualize which combinations could be more useful to highlight lithological changes (Annex 2 and Annex 3). The band ratios combinations are listed below:

1. Ferric oxide content/Opaque index
2. Ferric oxide content/FeOH group content
3. AlOH group composition/Ferric Oxide composition
4. Ferrous iron index/MgOH group content
5. Ferrous iron index/FeOH group content
6. Opaque index/AlOH group content
7. Opaque index/AlOH group composition
8. FeOH group content/MgOH group content
9. FeOH group content/Ferrous iron content in MgOH
10. MgOh group content/MgOH group composition
11. FeOH group content/MgOh group content

The data stretch values proposed by Cudahy (2012) fit only to three of the band ratios calculated on the borehole data. These band ratios where the ferric oxide composition, AlOH group composition and MgOH composition. For this reason, for each band ratio the parameters where set to the best fit that would show all the values of each sample measured to be able to visualize how the band ratios change in relationship with depth.

3.2. ASTER band ratios and lithlogical maps

For ASTER images a total of 13 band ratios where produced (Figure 7). Due to the use of two sets of ASTER images from different years and different months, in all the band ratio processed it can be seen differences in the band ratio value between the two years. Despite this issue a continuity of lithological units can be seen through both sets of images. The images the images that where taken in 2005 have lower values in comparison to the images taken in 2002. Possible causes for these changes in band ratio values will be addressed in Chapter 4- Discussion.

From the band ratios, the content for Ferric oxide group, Ferrous iron index, Kaolin group and MgOH group vary from low to moderate. For the AlOH and FeOH groups the content through the whole study area remains low, in the case of the AlOH group these are mostly located in multiple concentrated patches spread though the study area. Meanwhile, for the Silica index and the ferrous iron in MgOH the content varies from moderate to high through the study area. Lastly, the opaque index band ratio indicates that the no content of opaque minerals in the study area.

Based on band ratio combinations done for the borehole spectroscopy, and the result obtained from the band ratios from the ASTER Images, RGB combinations using different ratios where put together to generate lithological maps. Since the band ratios on the ASTER images for FeOH group index and the opaque index were very low and none respectively, these were be discarded for usage in a RGB combination. This leaves three possible RGB band ratio combinations (Figure 8) that can be compared with band ratios from the borehole data.

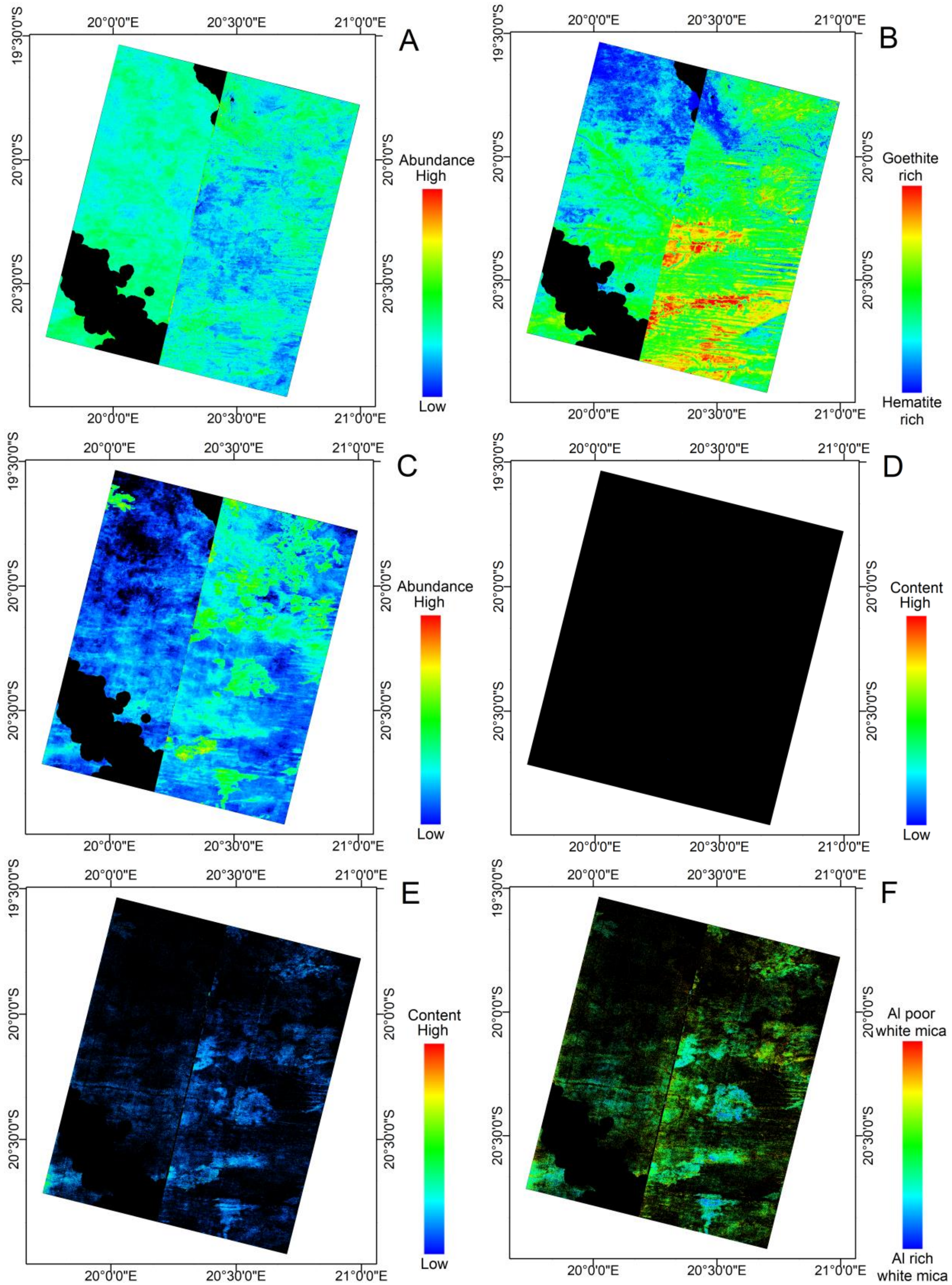
A
Abundance
High
Low
B
Goethite
rich
Hematite
rich
C
Abundance
High
Low
D
Content
High
Low
E
Content
High
Low
F
Al poor
white mica
Al rich
white mica
20°0'0"E
20°30'0"E
21°0'0"E
19°30'0"S
20°0'0"S
20°30'0"S

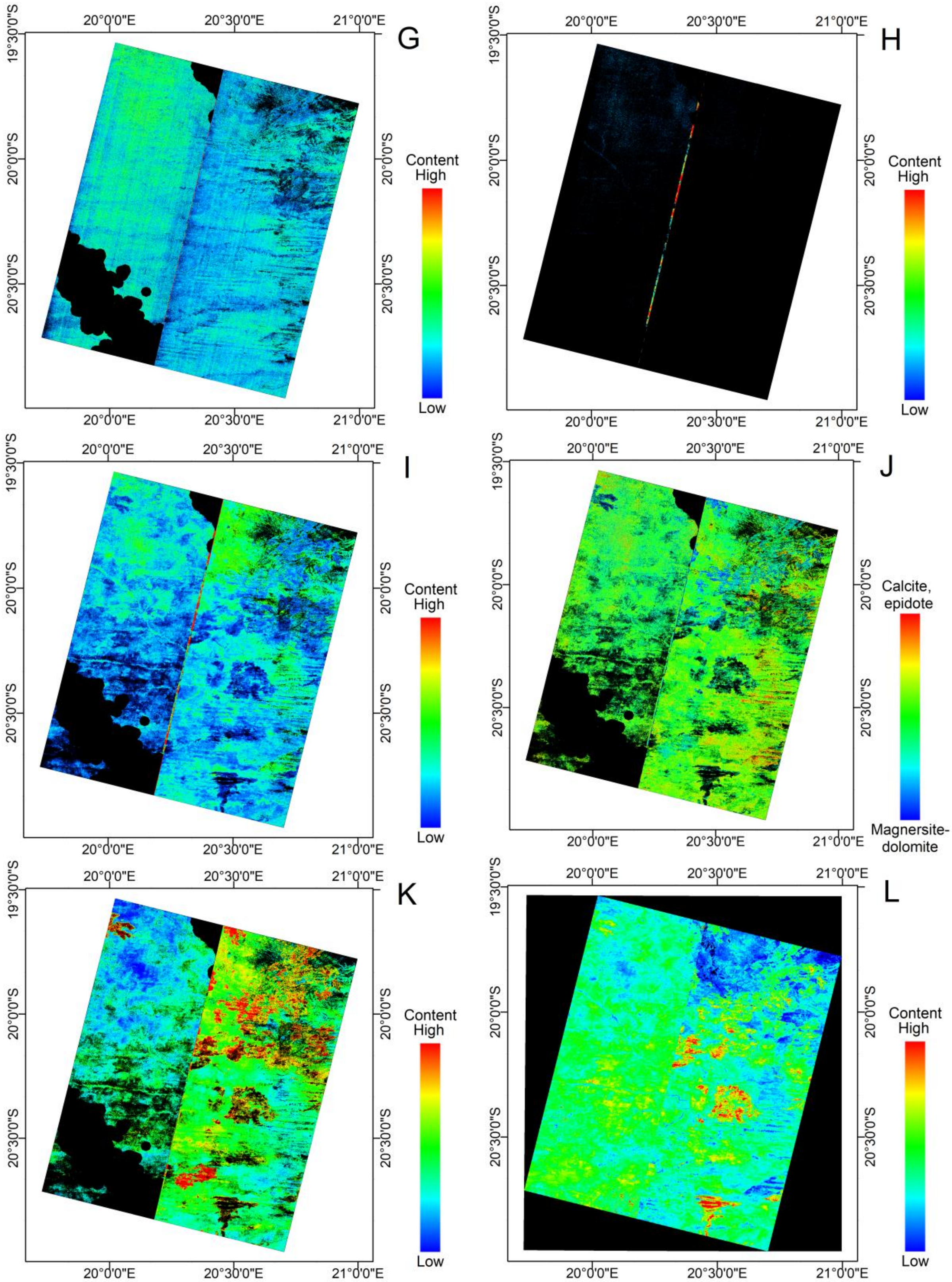

Figure 7. A) Ferric oxide content, B) Ferric oxide composition, C) Ferrous iron index, D) Opaque index, E) AlOH group content, F) AlOH group composition, G) Kaolin group content, H) FeOH group content, I) MgOH group content, J) MgOH group composition, K) Ferrous iron in MgOH and L) Silica index.

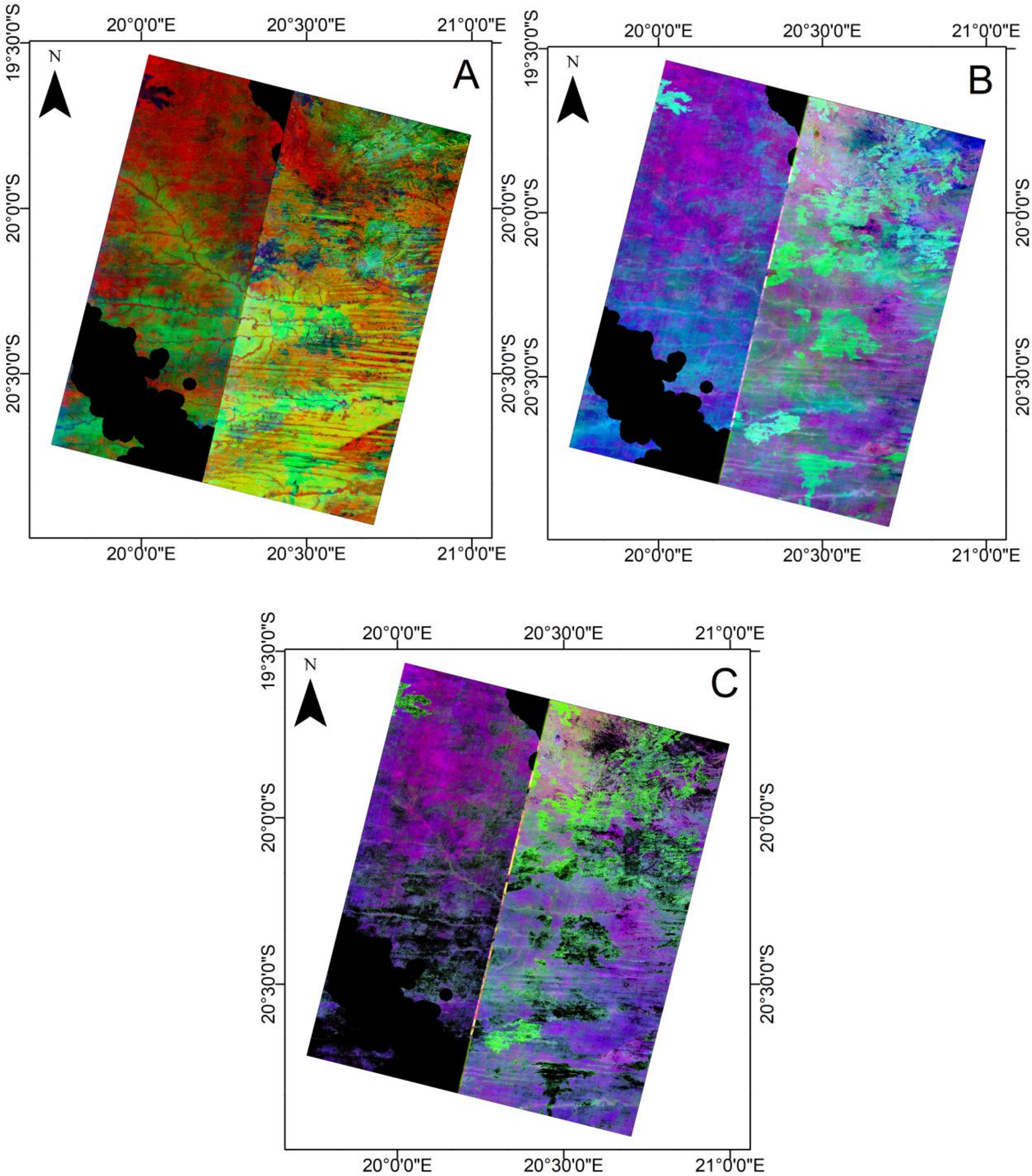

Figure 8. RGB ASTER band ratio combinations A) R: MgOH group composition, G: Ferric oxide composition and B: AlOH group composition. B) R: MgOH group content, G: Ferrous iron index and B: Ferric oxide content. C) R: MgOH group content, G: Ferrous iron in MgOH and B: MgOH group composition

3.3. 3D Euler deconvolution

With 3D Euler deconvolution a total of 20 depth range maps where produced. During the processing four values of structural index (SI) were used: 0, 0.25, 0.5 and 0.75 and the Euler solutions where divided into different depth ranges 70-130m, 90-150m, 110-170m and 130-190m (Figure 9 and Annex 4). This depth values where selected based on the different depth of the boundaries described in the borehole logs. Finally, for kriging, the grid cell size was set to 200 meters, to facilitate the interpretation with the boreholes.

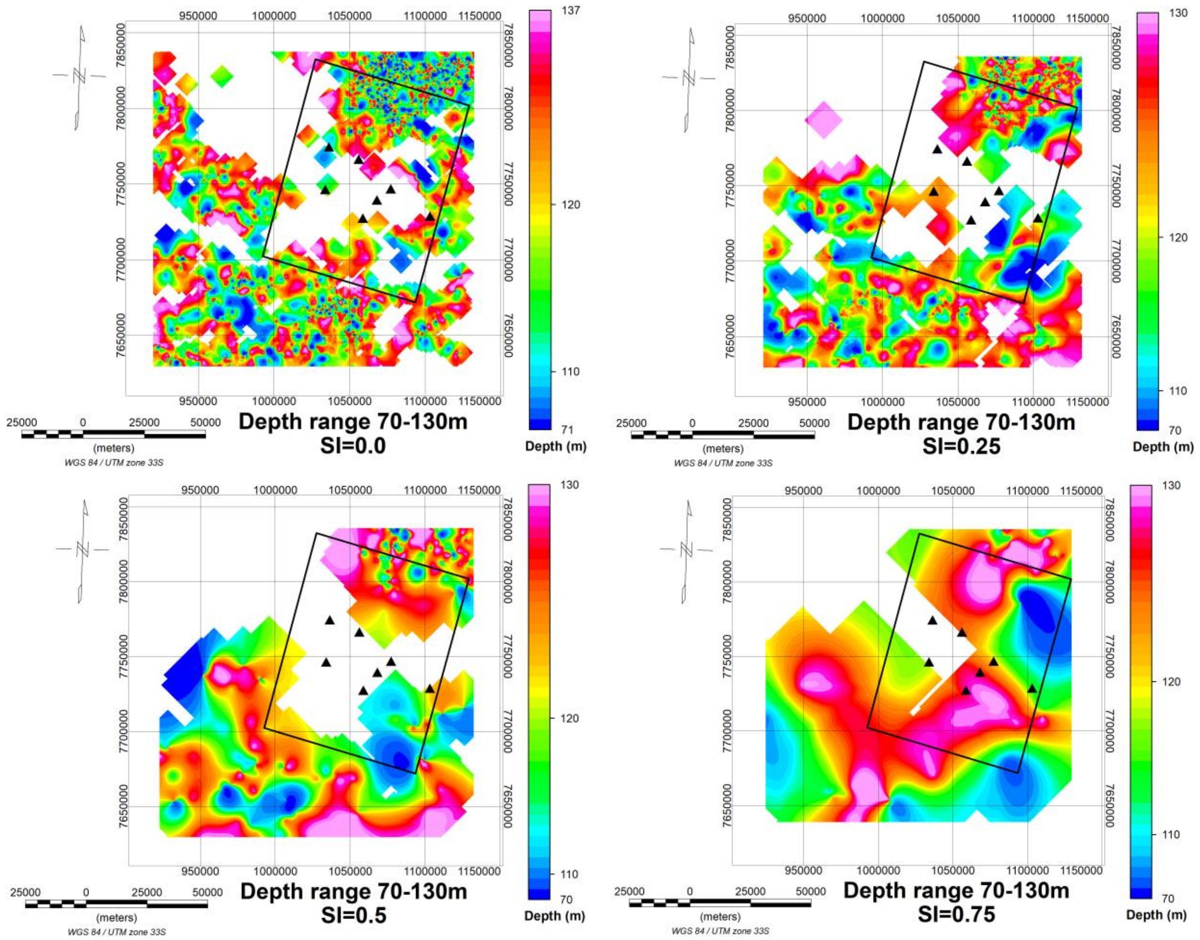

Figure 9. 3D Euler deconvolution depth maps. Depth range between 70-130 meters. Structural index varies between 0 and 0.75.

Based on Reid's assumption that "a real data set is likely to contain anomalies from sources with various structural indices" (Reid et al., 1990), there would be no unique structural index that satisfies the whole data set. This means that features that do not fit one index will be poorly represented but will be clearly outlined in another index. This would explain why the depth values for some boreholes show in one map but will not show in another map that has different structural index. However, as the structural index is increased in general for the borehole locations the depth value on the map increases. This is consistent with Reid's statement that "An index that is too low gives depths that are too shallow; one that is too high gives estimates that are too deep. Even if the index is correct, depth estimates are more precise for high-index sources than for low" (Reid et al., 1990) and even after choosing wrong structural index he states that "gross structural trends can still be outlined.". However, with the last statement this is not seen for the case of the maps generated for this study as the SI value is increased some structural trends disappear. This is clearly seen in the maps with depth range between 70-130 where the map becomes less detailed as we increase the structural index from 0.0 to .075 (Figure 9). This would suggest that the better structural index out of the four chosen ones would be 0.

When comparing the depth range map and the borehole depth values between the Kalahari and the Damara only boreholes WW34851, WW34873 and WW35045 have similar value of depth for the maps that where generated using a structural index of 0.0. However, it is important to mention that since a window size of 3x3 was selected for calculating the 3D Euler deconvolution, shallow boundaries cannot be detected with Euler deconvolution. This is due to the limitation of Euler deconvolution in which the minimum depth that it can be calculated is half of the window size (Reid et al., 1990), and since the pixel size of the aeromagnetic data set is 50, this would mean that the minimum depth that can be calculated is 75 meters. This would not allow to compare the depth range maps with boreholes WW35039 and WW34876. For the case of boreholes WW35037, WW35040 and WW35044 none of the depth maps had similar depth value compared to the boundaries describe in the borehole logs.

4. DISCUSSION

When comparing the borehole band ratios and the ASTER band ratios, these cannot be integrated directly to each other. There are several reasons why this is, related to type of measurement, different sensors, and sample sizes and distances. First of all, the stretch parameters proposed by Cudahy (2012) for the ASTER band ratios do not fit with the values obtained in the band ratios from the borehole measurements, except for the Ferric oxide, AlOH group and MgOh group composition band ratios. Furthermore, the stretch values where determined only taking into consideration the conditions which affect the ASTER measurements. Next to that, the measurements where done with different sensors. Each of the sensor has not only different sensitivity values for each wavelength but the ASTER sensor is a passive sensor, therefore the measurements depend on the sun angle elevation, while the ASD Terraspec Halo is an active sensor, in which the source light is controlled. Lastly, the distance from sensor to the sample will affect the reflectance values, since the satellite sensor is orbiting around the earth, and the measurements will be highly affected by atmospheric conditions, where the where sunlight will undergo reflection, reflection and absorption. While for the borehole measurements, the distance between the sample and the sensor is usually a few millimetres, so the effect of atmospheric gases is not as significant. Another variable that influenced how the ASTER stretch values where determined, was the effect of dry vegetation, which is not removed in the masking process when processing the band ratios. This is not an issue for the borehole measurements since there is no influence of vegetation in the samples.

Besides the previously mentioned factors that affect the stretch values for the borehole and ASTER band ratios, it is necessary to take into consideration the studies used for the proposed band ratios by Cudahy, 2012. For the ASTER dataset Cudahy (2012) determined these stretch values based on a wide variety of studies, in which ASTER images where used for mineral mapping in Australia and USA. These maps where validated using different classification techniques on hyperspectral images, gamma ray surveys and ground control points(Cudahy et al., 2002, 2005, 2008; Haest et al., 2012; Hewson et al., 2005; Ninomiya et al., 2005; Rowan et al., 2003). In addition, to determine the specific thresholds Cudahy,2012 used data from a quantitative mineralogy using VNIR and SWIR wavelengths carried out on drill cores from the Rocklea channel iron deposit in Western Australia. This quantitative measurements of abundance and compositional variations where validated using XRF (X-ray fluorescence) and XRD (X-ray diffraction)(Haest et al., 2012). However, as it was mentioned above, for this study, the upper and lower thresholds of each borehole band ratio combination were determined based on the best fit to display all the band ratio values. This "best fit display" of the data only allow us to determine relative abundance and compositional changes within each borehole but will not allow us to determine the actual abundance of each mineral group (Ferric oxide, AlOH, MgOH, Ferrous iron). Also, it must be considered that the borehole samples could not be washed. So, the bentonite used in the drilling process might be mixed with the sample and it could affect the mineral content displayed in each band ratio. But to assess how significant the influence of bentonite is in the spectral signature it would be necessary to carry out geochemical analysis and determine if there is a significant amount of bentonite present in the sample.

Looking at the ASTER images and the band ratio products the reflectance value of the images captured in 2002 are higher than the values of the images collected in 2005. This could be caused mainly by two factors: sun angle elevation and atmospheric influence. Looking at the metadata from each ASTER scene sun angle elevation seems to not be the cause of the difference in reflectance values since they are relatively similar, being 48º for the images from 2002 and 52º for the images from 2005. Since the sun angle elevation difference is not significant enough to explain the difference in reflectance values between the two ASTER scenes it is most likely that atmospheric influences are the main cause for the difference in the reflectance value between the two ASTER scene. This is also supported by the fact that the images collected in 2002 have thick clouds in parts of the image while the images from 2005 have no cloud cover.

Despite the limitations that both ASTER and borehole band ratios have, it still possible to compare changes in band ratios patterns. However, there is already a limitation, since the band ratio values for FeOH group index and Opaque index derived from the ASTER images, where very low and none respectively. This does not allow comparison with most of the possible band ratio combination from the borehole spectral measurements with the ASTER band ratio combination images. These only leaves from the 11 possible borehole band ratio combination a total of 3 band ratio combinations to be compared with ASTER band ratio combination images:

1) Ferric oxide composition/AlOH group composition
2) Ferrous iron index/ MgOH group composition
3) MgOH group content/MgOH group composition

However, for each boreholes these band ratio combinations (Annex 2) do not display the same pattern when there is a change from the Kalahari group to the Damara group (Table 2). Through this lithological change the values increase or decrese , with no clear pattern. This could be also related to horizontal lithological changes which further complicate the integration of these datasets. Similar integration problems where encountered by Cudahy (2017), who tried to integrate hyperspectral image from drill cores with ASTER images. The drill core hypespectral image where resampled to simulate ASTER, and together with mineral interpretation, XRD,XRF, scanning electron microscope and electron microprobe he determined the threshold for each band ratio to be able to see pattern changes in abundance and compositions. So, in the case of this study, to be able to integrate ASTER band ratios with borehole band ratios it would be necessary to carry out a geochemical analysis, like XRD or XRF of each sample of the boreholes, and establish threshold values for each band ratio as also it is suggested by Cudahy (2017). It would be also necessary to remove the effect of dry vegetation by using unmixing technique, although Cudahy (2017) states that, there are still errors in masking the effects of dry vegetation, which would still affect any direct integration between the ASTER and the borehole spectral measurements. However, such geochemical analysis and dry vegetation masking is beyond the scope of this study.

Despite the difficulties with the ASTER images and the fact the study area is mostly covered by silica, from the sand and sandstone deposits from the Kalahari group (Figure 7 L), it is still possible to see lithological changes. From Figure 8 A it can be seen that the areas that where mapped as the Kalahari group (Figure 2) the band ratio combination suggest that there is calcite present at the surface, where it is also in the borehole log description where it is described as calcrete. Also, in this image it is observed that the calcite is no longer present in the outcrops of the Damara group, located in the north-eastern part of the study area (Figure 2). Instead, according to these images, the Damara group contains mostly hematite, based on the Ferric oxide band ratio. Furthermore, based on the AlOH it can interpreted that the mica in these units is well ordered white mica, like muscovite or illite. However, these presence of AlOH group minerals, like the well-ordered white mica is also present in the Kalahari group. This could indicate that possibly the Kalahari group was formed through transport of material derived from the erosion from the exposed Damara group. From figures 8 B and C it is possible interpret that in the area the MgOH group content is high as well as the content of ferric oxide indicating that the Kalahari group besides containing high abundance of silica it also contains high abundance of ferric carbonates like ferroan dolomite, ankerite or siderite. For the case of the north-eastern outcrop from the Damara group it can be interpreted that these rocks have undergone strong weathering, which is consistent with the observation that probably the Kalahari group is a product of the erosion of the Damara group.

Regarding the integration between the borehole spectral measurements and the aeromagnetic data, it is not possible to integrate these datasets. There is no clear pattern that allows to clearly distinguish the boundaries between the Kalahari and the Damara groups through band ratio combinations. Therefore, with this current study there is no additional information that can be obtained from the borehole data, besides the lithological description from the borehole logs for aiding in the aeromagnetics interpretation. Also, for the aeromagnetic data, it would not be sufficient to carry out geochemical analysis to determine the thresholds for the band ratios, as this would only display information on already established boundaries, which are the intervals in which each sample was collected. So, to integrate aeromagnetic data with the borehole data t would be required to have a continuous sampling of each drill hole. Since it was not possible to determine other lithological boundaries through the borehole band ratio combinations, the lithological boundaries from the borehole log description are the only information for establishing the lithological boundaries at depth. Taking these boundaries together with the assumption that the boundary between the 2 lithological units is horizontal the best depth map that fits these data is the map which was processed using a structural index of 0 and a depth range between 70-130m (Figure 10). Based on this map we could assume that this display an approximate of depth of the boundary between the Kalahari and the Damara group. However, if more detailed and deeper borehole information was available, greater depth range maps may also display the deeper lithological boundaries. However, from borehole log there is no information on a lithological change beyond 130 meter depth.

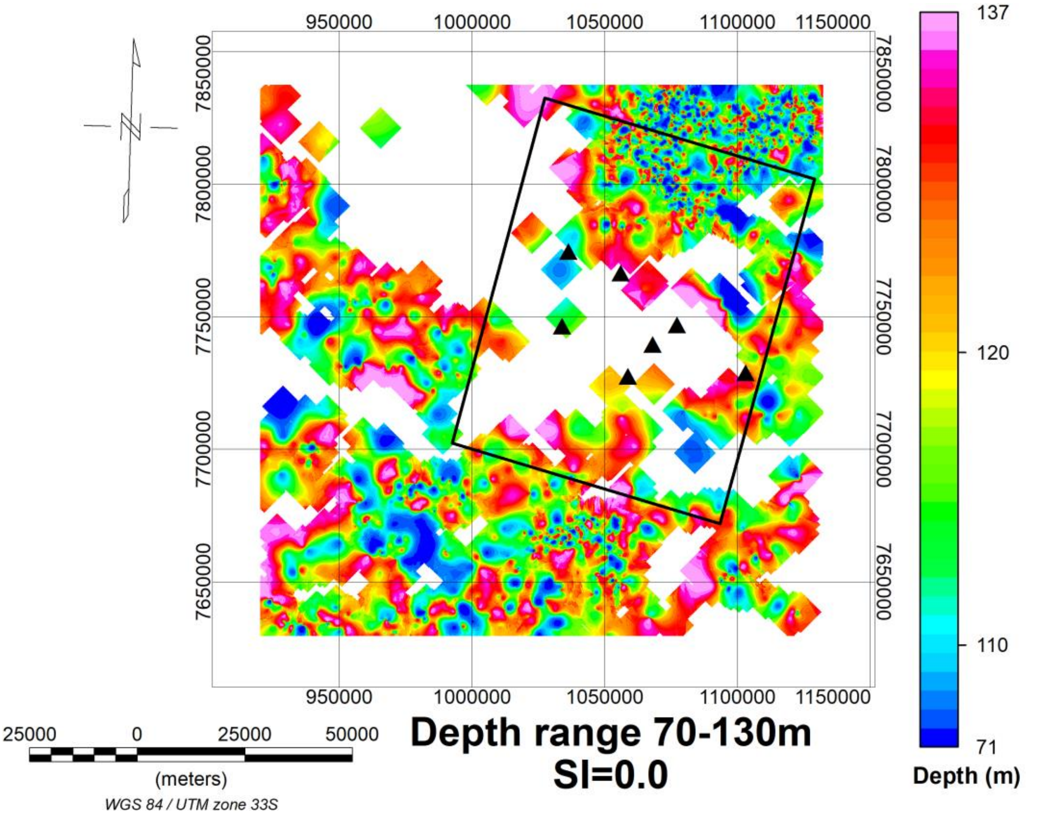

Figure 10. 3D Euler deconvolution map, using structural index of and limiting source of the magnetic anomalies between 70-130 meter depth. This would indicate the approximate lithological boundary between the Kalahari group and the Damara group throughout the study area.

When comparing the 3D Euler deconvolution maps (Figure 10 and Annex 4) with the ASTER band ratio combinations (Figure 8) , it can be seen that the north-eastern outcrops match with shallow magnetic anomalies reaching a depth between 0 to 110. The change in depth of the anomalies might be the result of the weathering on the Damara group, in which most of the magnetic minerals have undergone geochemical reactions forming new minerals with no, or much lower, magnetic properties.

Although, the ASTER and borehole band ratios and the 3D Euler deconvolution maps could not be successfully integrated, it was seen that bot, the ASTER and borehole data, displayed variations in their band ratios values. For the ASTER data it was possible to identify some difference between the north-eastern outcrops from the Damara group and the Kalahari group, still the high abundance of silica in the area complicates the spectral characterization of these lithological units. In the case of borehole data, it was observed that at depth the values of the band ratios changed (Annex 3). However, due to the lack of geochemical analysis it is not possible to determine if both units can be differentiated uniquely through band ratio analysis. Without geochemical data the threshold parameters to determine the abundance and composition of each mineral group (AlOH, MgOH, Ferric oxide, ferrous iron group) cannot be set. Therefore, it is not possible to conclude if any of the lithological units, could be identified through band ratio analysis. Regarding the aeromagnetic data, the only information that proved to be useful for establishing the parameters of the 3D Euler deconvolution where boreholes logs, since in this study it was not possible to obtain further information through the band ratio analysis. Although the 3D Euler deconvolution showed a strong relationship of shallow magnetic anomalies in the area where the north-eastern outcrops are located, still this did not provide any additional information to aid in determine the best parameters for processing the Euler deconvolution. Also, the ASTER band ratios, did not provide any validation for which of the 3D Euler deconvolution maps best fit the existing geology. However, in all the 3D Euler deconvolution maps the shallow anomalies where displayed in this area where these outcrops where located. Although the it is not possible to determine the 3D structure in the subsurface with the 3D Euler deconvolution maps, still the consistent contrast, in the north-eastern outcrops, between the different depth range maps allow validate the in fact there is shallow lithologic boundary. Which, allow to assume that the depth estimates in the rest of the study area can be also considered an approximate depth at which the boundary between the Kalahari group and the Damara group occurs.

5. CONCLUSION

Throughout this research, it was studied if a combination of remote sensing, field and borehole data could integrated to determine their added value for 3D geological modelling, in currently unexplored areas that have a high mineral resource potential, such as Namibia. Borehole hyperspectral measurements band ratio combination graphs where made to display how mineral abundance and lithological composition changes with depth. ASTER data was processed to obtain band ratio combination images to display spatial contrasts in surface mineralogy and lithology throughout the study area. Aeromagnetic data was processed using 3D Euler deconvolution to estimate the depth of magnetic anomalies in the study area. These results enabled the making of depth range maps which show how sources of magnetic anomalies where distributed throughout the study area. Finally, it was studied the added value of integrating these datasets for 3D geological modelling study area located in Omaheke region.

Although borehole band ratios values varied with depth, it appeared not to be possible to semi-quantitatively determine the abundance or composition of each of the mineral group (AlOH, MgOH, Ferric oxide, Ferrous iron groups). The index stretch values that were proposed by Cudahy (2012) do not fit with the borehole band ratios. Instead, the stretch values for the borehole band ratios; were adjusted to display all values optimally. This can mainly be attributed to the fact that the spectra for ASTER and the borehole measurements where done in different conditions and by different sensor which do not allow a direct comparison and integration of both datasets. Even; if there were spectral contrast variations in each borehole, this did not display a pattern which would allow to highlight a lithological change between the Damara group and the Kalahari group. It is therefore concluded that to establish threshold values for the band ratio, geochemical analysis, such as X-ray diffraction (XRD) or X-ray fluorescence (XRF), of the borehole sample should be done.

Regarding the integration between borehole spectral measurements and aeromagnetic data, it appeared not to be possible to integrate these datasets as there is no clear pattern in the borehole data that allows to distinguish between the Kalahari group and the Damara groups through band ratio combinations. In order to validate which of the depth range maps best fits to the study area, it was decided to use only the boundary between the Kalahari and the Damara group that is described in the borehole log descriptions, since the borehole band ratios did not provide any additional information of the lithological boundaries. Based on this information, it was concluded that the best depth map that fits these data is the one processed using a structural index of 0 and a depth range between 70-130m.

The ASTER RGB band ratio combination images do allow to differentiate the Damara outcrops located in the north-eastern part of the study area. This is mainly caused by calcite which is present in the Kalahari group and not in the Damara group. However, this interpretation is strongly affected by the high content of silica in the Kalahari group, which masks most of the mineral occurrences. Also, the Kalahari group besides containing high abundance of silica it also contains high abundance of ferric carbonates like ferroan dolomite, ankerite or siderite, according to the band ratio combination images. For the case of the north-eastern outcrop from the Damara group it can be interpreted that these rocks have undergone strong weathering. This is seen in the band ratio combination images, where the Damara group contains mostly hematite and well-ordered white mica, like muscovite or illite. However, these presence of AlOH group mineral, like the well-ordered white mica is also present in most of the study area. This could possibly indicate that the Kalahari group was formed through of transport material derived from the erosion from exposed Damara group. Regarding the relationship between the 3D Euler deconvolution depth range maps and ASTER band ratio combination, these showed a strong correlation where the north-eastern outcrops seen in the north-eastern part of the study area display shallow magnetic anomalies in all the depth range map that where generated using different structural indices. Although the ASTER images did not provide additional information to be able to establish which structural index best fit the study area. However, the fact that all the 3D Euler deconvolution maps displayed shallow magnetic anomalies in location of the outcrops this would indicate that other 3D Euler deconvolution depth range maps could also be used to identify structures that are not horizontal, like inclined normal or thrust faults.

During this research it the proposed objective of integration of the different datasets was partially achieved. The ASTER satellite images and the aeromagnetic data could be integrated successfully as both showed strong correlation of distinguishing the north-eastern outcrops of the Damara group which also allowed to validate that all depth range maps displayed possible subsurface lithological boundaries between the Damara and the Kalahari groups. Although it was not possible to establish clear structure. since the 3D Euler deconvolution does not provide unique enough solutions. It was not possible to integrate the borehole hyperspectral measurements with any of the other datasets, due to the problem with the band ratio stretch values that where stated above. But it was concluded that it spectral contrast between each sample was observed, but geochemical analysis is required to further validate the added value of the borehole band ratio in 3D geological modelling.

Regarding the research questions stated in the introduction section, it was possible to answer them through the development of these research. Here, the hyperspectral signatures obtained with a field spectrometer on drill cores could not be directly related with the multi-spectral signatures from multispectral images due to the different condition in which the measurements where acquired. This in turn affected the band ratio products for the borehole measurements which it was concluded that geochemical analysis is required to be able to establish their stretch values to be comparable with the band ratios obtained from the ASTER images.

Concerning the question if there are any lithological units that are not distinguishable on the surface or underground through spectral signatures or through magnetic anomalies, it was concluded that through spectral measurement or multi-spectral images all three lithological units could be distinguished. It is important to mention that although it was not possible to determine through band ratio the mineral abundance and composition, still it could be seen that there where differences in the spectral contrast of each sample. This indicates that if the stretch values for these band ratios could be determined through further geochemical analysis, this would allow to correlate easier with ASTER band ratios and determine if both of them provide similar lithological and mineral information. Regarding the aeromagnetic data, not all of the lithological units where distinguishable. Here, the Damara group was the only lithological unit which displayed magenta anomalies, which could be identified in the 3D Euler deconvolution depth range maps.

The 3D Euler deconvolution maps displayed different depth estimates for the boundary between the Kalahari and the Damara groups when compared with the depth in the borehole logs. The depth difference range between 30 to 100 meters. The difference got greater as the SI increased. It is important to consider that the lithological boundaries from the borehole logs are not 100% accurate since these boreholes were not drilled with the purpose of mineral exploration, so the sampling is not done at a regular interval, which make it difficult to establish an accurate depth of the lithological change.

Finally, through this research it was concluded that with the current analysis done for the borehole data, the band ratios done on the resampled hyperspectral measurements did not prove any additional information that the 3D Euler deconvolution depth range maps and the borehole description logs already provide. But as it was stated in multiple occasions, this could change if geochemical analysis is available to determine the stretch value of the borehole band ratios. As these data could display better any change in the mineral abundance or composition of the lithological unit.

LIST OF REFERENCES

Andritzky, G., Ajagbe, S., Brunett, R., Petzel, V., Roesener, H., & Schneider, G. (1998). Mineral map of Namibia. Geological Survey of Namibia.

Baptiste, J., Martelet, G., Faure, M., Beccaletto, L., Reninger, P. A., Perrin, J., & Chen, Y. (2016). Mapping of a buried basement combining aeromagnetic, gravity and petrophysical data: The substratum of southwest Paris Basin, France. *Tectonophysics*, *683*, 333–348.

Bedini, E., Van Der Meer, F., & Van Ruitenbeek, F. (2009). Use of HyMap imaging spectrometer data to map mineralogy in the Rodalquilar caldera, southeast Spain. *International Journal of Remote Sensing*, *30*(2), 327–348.

Belocky, R., Heiss, G., & Salzer, F. (1997). Structural analysis and lithological classification in humid areas using satellite remote sensing and airborne geophysics - a case study from the Bohemian Massif/lower Austria. *Earth Surface Remote Sensing. Proc. SPIE Conference, London, 1997*, 351–356.

Burney, C., Gibson, H., Mubita, J. P., & Titus, N. (2015). First 3D modelling of the sub- surface of east-central Namibia using combining geophysics with distal geological data. In *South African Geophysical Association's 14th Biennial Conference and Exhibition 2015* (pp. 3–5). Johannesburg, South Africa.

Chen, X., Warner, T. A., & Campagna, D. J. (2007). Integrating visible, near-infrared and short-wave infrared hyperspectral and multispectral thermal imagery for geological mapping at Cuprite, Nevada. *Remote Sensing of Environment*, *110*(3), 344–356.

Cudahy, T. (2012). Geoscience Product Notes for Australia (EP-30-07-12-44), 1–26. Retrieved from http://c3dmm.csiro.au/Australia_ASTER/Australian ASTER Geoscience Product Notes FINALx.pdf

Cudahy, T., Caccetta, M., Cornelius, A., Hewson, R., Wells, M., Skwarnecki, M., Halley, S., Hausknecht, P., Mason, P., & Quigley, M. (2005). *Regolith, Geology and Alteration Mineral Maps from New Generation Airborne and Satellite Remote Sensing Technologies, and Explanatory Notes for the Kalgoorlie-Kanowna 1: 100,000 Scale Map Sheet Remote Sensing Mineral Maps. MERIWA Report 252*.

Cudahy, T., Jones, M., Thomas, M., Laukamp, C., Caccetta, M., Hewson, R., Rodger, A., & Verrall, M. (2008). Next Generation Mineral Mapping : Queensland Airborne HyMap and Satellite ASTER Surveys 2006-2008. *CSIRO Exploration & Mining Report P2007 / 364*, 152.

Cudahy, T., Okada, K., Cornelius, A., & Hewson, R. (2002). Regional to prospect scale exploration for porphyry-skarn-epithermal mineralisation at Yerington, Nevada, using ASTER and Airborne Hyperspectral data. Exploration and mining report No 1122, (1122), 5–11.

Cudahy, T., & Thomas. (2016). Mineral Mapping for Exploration: An Australian Journey of Evolving Spectral Sensing Technologies and Industry Collaboration. *Geosciences*, *6*(4), 52. Retrieved from http://www.mdpi.com/2076-3263/6/4/52

Eberle, D., Andritzky, G., & Wackerle, R. (1995). The new magnetic data set of Namibia : Its contributions to the understanding of crustal evolution and regional distribution of mineralization. *Communications - Geological Survey of Namibia*, *10*, 143–152.

Fadel, I., Kerle, N., & van der Meijde, M. (2014). 3-D object-oriented image analysis of geophysical data. *Geophysical Journal International*, *198*(1), 357–365.

Fallara, F., Legault, M., & Rabeau, O. (2006). 3-D integrated geological modeling in the Abitibi subprovince (Québec, Canada): Techniques and applications. *Exploration and Mining Geology*, *15*(1–2), 27–42.

Finn, C. A., & Morgan, L. A. (2002). High-resolution aeromagnetic mapping of volcanic terrain, Yellowstone National Park. *Journal of Volcanology and Geothermal Research*, *115*(1–2), 207–231.

Frimmel, H. E., Basei, M. S., & Gaucher, C. (2011). Neoproterozoic geodynamic evolution of SW-Gondwana: A southern African perspective. *International Journal of Earth Sciences*, *100*(2), 323–354.

Gandhi, S. M., & Sarkar, B. C. (2016). *Essentials of mineral exploration and evaluation*. Saint Louis: Elsevier Science.

Geosoft. (2018). Grav/Mag Interpretation. Retrieved February 19, 2018, from https://my.geosoft.com/elearning/lessons/#/reading/843

Gomez, C., Delacourt, C., Allemand, P., Ledru, P., & Wackerle, R. (2005). Using ASTER remote sensing data set for geological mapping, in Namibia. *Physics and Chemistry of the Earth, Parts A/B/C*, *30*(December 2004), 97–108.

Haest, M., Cudahy, T., Laukamp, C., & Gregory, S. (2012). Quantitative Mineralogy from visible to shortwave infrared spectroscopic data. I. Validation of Mineral Abundance and Composition Scripts

at the Rocklea Channel Iron Deposit in Western Australia. *Economic Geology*, *107*, 209–228.
Hewson, R., Cudahy, T., Mizuhiko, S., Ueda, K., & Mauger, A. (2005). Seamless geological map generation using ASTER in the Broken Hill-Curnamona province of Australia. *Remote Sensing of Environment*, *99*(1–2), 159–172.
Hewson, R., Mah, A., Dunne, M., & Cudahy, T. (2003). Mapping Mineralogical and structural relationships with satellite- borne ASTER and airborne geophysics at Broken Hill. *ASEG 16th Geophysical Conference and Exhibition*, (February), 1–4.
Hewson, R., & Robson, D. (2014). Using ASTER and geophysical mapping for mineral exploration in Wagga Wagga and Cobar area, N.S.W. *Geological Survey of New South Wales*, (140). https://doi.org/ISSN 0155-3410
Mielke, C., Muedi, T., Papenfuss, A., Boesche, N. K., Rogass, C., Gauert, C. D. K., Altenberger, U., & de Wit, M. J. (2016). Multi- and hyperspectral spaceborne remote sensing of the Aggeneys base metal sulphide mineral deposit sites in the Lower Orange River region, South Africa. *South African Journal of Geology*, *119*(1), 63–76.
Miller, R. M. (2008). *The geology of Namibia*. Windhoek, Namibia: Ministry of Mines and Energy, Geological Survey.
Ninomiya, Y., Fu, B., & Cudahy, T. J. (2005). Detecting lithology with Advanced Spaceborne Thermal Emission and Reflection Radiometer (ASTER) multispectral thermal infrared "radiance-at-sensor" data. *Remote Sensing of Environment*, *99*(1–2), 127–139.
Olawuyi, A. K., Ako, B. D., Omosuyi, G. O., & Adelusi, A. O. (2016). Application of 3D Euler deconvolution of aeromagnetic data and pseudogravity transforms in mineral exploration: a case study of the pegmatite-rich zones of Lafiagi, Central Nigeria. *Arabian Journal of Geosciences*, *9*(16).
Reid, A. B., Allsop, J. M., Granser, H., Millett, A. J., & Somerton, I. W. (1990). Magnetic interpretation in three dimensions using Euler deconvolution. *GEOPHYSICS*, *55*(1), 80–91.
Rowan, L. C., Hook, S. J., Abrams, M. J., & Mars, J. C. (2003). Mapping Hydrothermally Altered Rocks at Cuprite, Nevada, Using the Advanced Spaceborne Thermal Emission and Reflection Radiometer (ASTER), a New Satellite-Imaging System. *Economic Geology*, *98*(5), 1019–1027.
Swayze, G. A., Clark, R. N., Goetz, A. F. H., Livo, K. E., Breit, G. N., Kruse, F. A., Sutley, S. J., Snee, L. W., Lowers, H. A., Post, J. L., Stoffregen, R. E., & Ashley, R. P. (2014). Mapping Advanced Argillic Alteration at Cuprite , Nevada , Using Imaging Spectroscopy, 1179–1221.
Tex, I. den. (2006). *Hydrothermal alteration processes related to VMS deposit genesis in the Panorama district , Pilbara*. ITC. Retrieved from www.itc.nl/library/papers_2006/general/dentex_hyd.pdf
Thompson, D. T. (1982). EULDPH: A new technique for making computer- assisted depth estimates from magnetic data. *GEOPHYSICS*, *47*(1), 31–37.
van der Meer, F. D., van der Werff, H. M. A., van Ruitenbeek, F. J. A., Hecker, C. A., Bakker, W. H., Noomen, M. F., van der Meijde, M., Carranza, E. J. M., de Smeth, J. B., & Woldai, T. (2012). Multi- and hyperspectral geologic remote sensing: A review. *International Journal of Applied Earth Observation and Geoinformation*, *14*(1), 112–128.
Wang, G., Zhang, S., Yan, C., Song, Y., Sun, Y., Li, D., & Xu, F. (2011). Mineral potential targeting and resource assessment based on 3D geological modeling in Luanchuan region, China. *Computers and Geosciences*, *37*(12), 1976–1988.

ANNEX 1 – BOREHOLE DESCRIPTION LOGS

—1974-75—30 000 O.f-S

DW 57

Verwysing / Reference No. 211/

BOORGATVOLTOOIINGSVERSLAG (Privaat Kontrakteur)
BOREHOLE COMPLETION REPORT (Private Contractor)

(Goewermentskennisgewing R. 74 van 14 Januarie 1966, soos gewysig)
(Government Notice R. 74 of 14 January 1966, as amended)

0 ° 750' S
20 ° 537' E
20

B2

'n Afsonderlike verslag moet vir elke boorgat voltooi word.
A separate report to be completed in respect of each borehole.

A. Algemeen/General

1. Volle naam van applikant / Full name of applicant: MINISTRY OF LANDS AND RESETTLEMENT
2. Plaas / Farm: —
3. No.: —
4. Distrik / District: GAM / EAST HERERO
5. Boorterrein aangewys deur / Boring site selected by: GEOLOGIST
6. Geologiese terrein No. / Geological site No.: TGI 13
7. Boorgat No. / Borehole No.: ~~WW 33453~~ 34451
8. Poging / Attempt: 1 [X] 2 3 4
9. Datum van begin van werk / Date of commencement of work: 31/08/93
10. Datum van voltooiing van werk / Date of completion of work: 02/09/93
11. Boorwerk gestaak na goeddunke van / Boring stopped at discretion of: Applikant / Applicant; Inspekteur / Inspector: X
12. Gee 'n kort beskrywing van ligging van boorgat (bv. 100 meter noordwes van woonhuis) / Give a short description of site of borehole (e.g. 100 metres north-west of dwelling-house): ±14 km down DANEIB OMURAMBA from GAM ROAD

* Merk toepaslike blok met 'n kruis/Mark applicable block with a cross.

B. Geologie/Geology

Diepte van oppervlakte (meter) / Depth from surface (metres)	Strata	Dikte / Thickness (meter, metre)
0 – 2,5m	dry, mid grained sand with rounded	2,5
2,5 – 5m	calcrete + sand	2,5
5 – 40	calcrete + silcrete + sand	35
40 – 80	clayey sandstone occ. calcrete bands	40
80 – 92	brown, sandstone occ. schist	8
92 – 97	white porous, sandstone	5
97 – 109	brown, sandstone	12
109 – 110	polymict assemblage sandstone, schist, qz – alluvial	1

FOR CASING SKETCH SEE OVERLEAF

C. Deursnee en diepte van boorgat/Diameter and depth of borehole

1. 200mm mm van oppervlakte af tot op / mm from surface to 105 m
2. 150mm mm van / mm from 105 m af tot op / m to 110 m
3. Totale diepte van oppervlakte af / Total depth from surface: 110m

D. Water

1. Diepte van oppervlakte af waarop water gevind is / Depth from surface at which water was struck: 102,5 m
2. Diepte van oppervlakte af tot waar water styg / Depth from surface to which water rises: 50m
3. Opbrengs per sekonde / Yield per ~~second~~: 2,5m³/hr
4. Skynbare gehalte van water / Apparent quality of water: GOOD
5. Doel waarvoor die water gebruik sal word / Purpose for which water will be used: DOMESTIC + STOCK

E. Pomptoets/Pumping test

1. Binnedeursnee van pompsilinder / Inside diameter of pump cylinder: mm
2. Lengte van slag / Length of stroke: mm
3. Getal slae per minuut / Number of strokes per minute:
4. Diepte waarop pompsilinder geplaas was / Depth to which pump cylinder was inserted: m
5. Begin van toets: Datum / Commencement of test: Date 02/09/93 tyd/time 09:00
6. Voltooiing van toets: Datum / Completion of test: Date 02/09/93 tyd/time 13:00
7. Duur van toets / Duration of test: 4 (AIR LIFT) uur/hours
8. Nege-uur toets / Nine-hour test: liter tenk gevul in / litre tank filled in min.

L.W.—'n Skeplepel- of blaastoets is nie aanvaarbaar nie/N.B.—A bailer or air-blast test will not be acceptable.

F. Boorkoste/Drilling costs

	R	c
1. m geboor @ per m / m drilled @ per m		
2. Toets van boorgat / Testing of borehole: 4HRS DEVELOPMENT		
3. Voering in boorgat gelaat na voltooiing / Casing left in borehole on completion:		
(a) Gewoon: Lengte / Plain: Length 99 m @ per m		
(b) Geperforeer: Lengte / Perforated: Length 6 m @ per m		
TOTALE KOSTE / TOTAL COST		

G. Voering/Casing

Indien boorgat onsuksesvol is, meld of voering nie herwin kan word nie of op versoek van applikant in boorgat gelaat is
If borehole is unsuccessful please state whether casing is irrecoverable or left in borehole at request of applicant: N/A.

L.W.—Voering wat in onsuksesvolle gate gelaat word is nie subsidieerbaar nie/N.B.—Casing left in unsuccessful boreholes is not subsidisable.

H. Verklaring deur boorkontrakteur en boorinspekteur: Ek verklaar dat die inligting hierbo verstrek waar en juis is.
Declaration by boring contractor and boring inspector: I declare that the information supplied above is true and correct.

Handtekening van boorkontrakteur / Signature of boring contractor: [signature]
Datum / Date: 13-9-93
Adres / Address: AQUATECH (PTY) LTD. P.O. BOX 556 OKAHANDJA TEL: 06221-2239

Handtekening van boorinspekteur / Signature of boring inspector: [signature]
Datum / Date: 02/09/93
Inspektoraat / Inspectorate: INTERCONSULT NAMIBIA

L.W.—Sien keersy vir verklaring en onderneming deur applikant/N.B.—See reverse side for declaration and undertaking by applicant.

ANNEX 1 – BOREHOLE DESCRIPTION LOGS

G.P. S.52981—1974-75—30 000 (M-S

DW 57

Verwysing / Reference No. 211/

BOORGATVOLTOOIINGSVERSLAG (Privaat Kontrakteur)
BOREHOLE COMPLETION REPORT (Private Contractor)

(Goewermentskennisgewing R. 74 van 14 Januarie 1966, soos gewysig)
(Government Notice R. 74 of 14 January 1966, as amended)

WW 34851

Instruksie: 'n Afsonderlike verslag moet vir elke boorgat voltooi word.
Instruction: A separate report to be completed in respect of each borehole.

Algemeen/General

1. Volle naam van applikant / Full name of applicant: Booysen T & D
2. Plaas / Farm: Gam area
3. No.
4. Distrik / District: Hereroland East
5. Boorterrein aangewys deur / Boring site selected by: ICN
6. Geologiese terrein No. / Geological site No.: T65-3
7. Boorgat No. / Borehole No.: WW ~~33692~~
8. Poging / Attempt*: 1 [X] 2 3 4
9. Datum van begin van werk / Date of commencement of work: 09-09-94
10. Datum van voltooiing van werk / Date of completion of work: 14-09-94
11. Boorwerk gestaak na goeddunke van / Boring stopped at discretion of*: Applikant / Applicant: — Inspekteur / Inspector: X
12. Gee 'n kort beskrywing van ligging van boorgat (bv. 100 meter noordwes van woonhuis) / Give a short description of site of borehole (e.g. 100 metres north-west of dwelling-house): 20°07,22' S 20°18,91' E

* Merk toepaslike blok met 'n kruis/Mark applicable block with a cross.

Geologie/Geology

Diepte van oppervlakte (meter) / Depth from surface (metres)	Strata	Dikte / Thickness (meter/metre)
0	Calcrete	2
1	Recent	
2	Kalahari	
	Sandstone	111
113		
	Gneiss	108
	Grootfontein	
	Complex	
221		
EOH		

C. Deursnee en diepte van boorgat/Diameter and depth of borehole

1. 254 mm van oppervlakte af tot op / mm from surface to 23 m
2. 219 mm van / mm from 23 m af tot op / m to 221 m
3. Totale diepte van oppervlakte af / Total depth from surface: 221 m

D. Water

1. Diepte van oppervlakte af waarop water gevind is / Depth from surface at which water was struck: — m
2. Diepte van oppervlakte af tot waar water styg / Depth from surface to which water rises: RWL 102,00 m
3. Opbrengs per sekonde / Yield per second: SEEPAGE ml
4. Skynbare gehalte van water / Apparent quality of water
5. Doel waarvoor die water gebruik sal word / Purpose for which water will be used

E. Pomptoets/Pumping test

1. Binnedeursnee van pompsilinder / Inside diameter of pump cylinder: mm
2. Lengte van slag / Length of stroke: mm
3. Getal slae per minuut / Number of strokes per minute
4. Diepte waarop pompsilinder geplaas was / Depth to which pump cylinder was inserted: m
5. Begin van toets: Datum / Commencement of test: Date — tyd / time
6. Voltooiing van toets: Datum / Completion of test: Date — tyd / time
7. Duur van toets / Duration of test: uur / hours
8. Nege-uur toets / Nine-hour test: liter tenk gevul in / litre tank filled in: min.

L.W.—'n Skepiepel- of blaastoets is nie aanvaarbaar nie/N.B.—A bailer or air-blast test will not be acceptable.

F. Boorkoste/Drilling costs

	R	c
1. m geboor @ per m / m drilled @ per m		
2. Toets van boorgat / Testing of borehole		
3. Voering in boorgat gelaat na voltooiing / Casing left in borehole on completion:		
(a) Gewoon / Plain: Lengte / Length m @ per m		
(b) Geperforeer / Perforated: Lengte / Length m @ per m		
TOTALE KOSTE / TOTAL COST		

Voering/Casing

Indien boorgat onsuksesvol is, meld of voering nie herwin kan word nie of op versoek van applikant in boorgat gelaat is
If borehole is unsuccessful please state whether casing is irrecoverable or left in borehole at request of applicant

L.W.—Voering wat in onsuksesvolle gate gelaat word is nie subsidieerbaar nie N.B.—Casing left in unsuccessful boreholes is not subsidisable.

Verklaring deur boorkontrakteur en boorinspekteur: Ek verklaar dat die inligting hierbo verstrek waar en juis is.
Declaration by boring contractor and boring inspector: I declare that the information supplied above is true and correct.

Handtekening van boorkontrakteur / Signature of boring contractor: Booysen
Handtekening van boorinspekteur / Signature of boring inspector: F Schmidt
Datum / Date:
Datum / Date: 15-09-94
Adres / Address:
Inspektoraat / Inspectorate: ICN

L.W.—Sien keersy vir verklaring en onderneming deur applikant/N.B.—See reverse side for declaration and undertaking by applicant.

ANNEX 1 – BOREHOLE DESCRIPTION LOGS

PERCUSSION DRILL FIELD LOG

DATE DRILLED: 14-12-94
DATE LOGGED: 14-12-94
GEOLOGIST: F.Schmidt
GRID/GRID COORDS: 20°03,197'S
INCLINATION: 20°07,517'E

HOLE NO.: WW 34873
PROJECT: Hereroland East
FARM: T 75 B
LO COORDS.: Y..... X.....
AZIMUTH: ....

from	to	lengt	ROCK TYPE	DESCRIPTION	S.NO.
0	21		sand	red, f-gr, dune sand	
21	68		sand	yellow, f-mgr, grading into yellowish-orange	
~~68~~	~~81~~		~~sandstone~~ ?		
68	81		? sandstone	greyish, f-mgr	
81	91		? gravel-layer	multi-coloured rounded-subrounded quartz grains, slightly clayey	
91	96		? quartz	red oxidation, very clayey, weathering effect	
96	175		? quartz	brownish (dry), clayey, red (wet) strongly weathered	
175	250 EOH		Ultramafic rock ↓ probably a basalt	green, dolerite, red speckles, ferruginized, strongly magnetic, relatively fresh, but possibly worked out, coarse crystalline	

Due to improper drilling and sampling by the driller neither the lithology nor the contacts could be identified properly

F.Schmidt

ANNEX 1 – BOREHOLE DESCRIPTION LOGS

PERCUSSION DRILL FIELD LOG

34876

DATE DRILLED: 16-12-94
DATE LOGGED: 16-12-94
GEOLOGIST: F. Schmidt
GRID/GRID COORDS: 20°17,391'S
INCLINATION: 20°31,422'E

HOLE NO.: WW 34876
PROJECT: Hereroland East
FARM: T 69-3
LO COORDS.: Y..... X.....
AZIMUTH: ....

R
K
D

from	to	lengt	ROCK TYPE	DESCRIPTION	S.NO.
0	2		sand	surface sand, brown	
2	12		sandstone	beige, f-gr., orange ot	
12	32		-"-	beige + pink, f-gr.	
32	46		? mica-schist	dark-grey, black speckled, gneissoid	
				37-40 ferruginous	
				45-46 greenish mica->? chlorite, vein qz	
46	51		? dolomite	greyish, c-gr., orange ot, soft, big chunks	
51	54		? mica-schist	reddish, black speckled	
54	76		mica-schist	greyish-black, in parts very micaceous layering but no real foliation	
76	84		-"-	brownish, black speckled, mildly weathered and oxidized micaceous scales, but no real micaceous texture	
84	92		-"-	more greyish-dark, ferruginized in places, partly very mica-rich, 90-92 very weathered	
92	104		-"-	darkish, quite ferruginized, partly very mica-rich	
104	112		-"-	blackish 107-108 qz vein	
112	143		-"-	blackish, ferruginized	
143	146		-"-	blackish + greyish, black speckled ferruginized, soft	
146	160		-"-	blackish, gneissoid	
160	363		-"-	darkish, schistose, pyrite, partly abundant (± 10-15%)	
	EOH				

ANNEX 1 – BOREHOLE DESCRIPTION LOGS

FORMATION LOG SHEET

Page 1 of 1

Date drilled: 28/4 – 29/4/95
Date logged: 28/4 – 29/4/95
Geologist: J. Engelbrecht
Latitude: 20° 20,15' S

Hole number: T 95.B / WW35037
Project: GAM F1/6 – 1/94
Location: EAST HERERO
Longitude: 20° 21,3' E

KALAHARI

From	To	Rock Type	Description
0 m	5 m	SAND + DRIL MUD	
5 m	32 m	Fine-Med sand	pale yellowish-brown – khakhi sand
			(subrounded not well sorted, slightly
			clayey,
		Nb [illegible]-32	more reddish in colour; some pieces
			of calcrete. polymict
32 m	81 m	Fine- coarse sand stone	whitish, beige, buff, yellow brown, med sorted.
			(subrounded fragments; some clayey horizons
		Nb 60-63m	~~some~~ quartzite fragments.
		Nb 63-67m.	clay in sandy matrix (fine-coarse sand)
81m -	181 m	Ox. Mica schist.	greyish brown oxidised mica schist /phylite.
		Nb. 100,5-103	white Quartz vein
		Nb [illegible] 128-129	fine grained "damp" zones in schist/phylite
		131 - 131	" "
		135 - 137	white Quartz vein
		144 - 145	~~fine grain~~ Driller reports hammer blocking.
			(no evidence in samples.)
		159 - 160	Quartz vein
		Nb whole zone is characterised by some alternation of	
		slightly more	oxidised and slightly less oxidised bands
181 m -	201 m	Fresh grey mica schist.	
	EOH		

ANNEX 1 – BOREHOLE DESCRIPTION LOGS

FORMATION LOG SHEET

Page __ of __

Date drilled: 26-5/95 –
Date logged: 26/5/95 – 31/5/95
Geologist: EdE
Latitude: 20° 26,6265'S

Hole number: T100 C = WW35039.
Project: GAm
Location: 545 m 025 off 20°,448°S / 20.775°E
Longitude: 20°46.527'E

From	To	Rock Type	Description
0	2 m	Soil / overburden.	
2	11 m	Grey-khaki white sand	coarse – fine (silty) sands; poor sorting subangular – rounded fragments loosly consolidated (probably some calcitic cement).
11	22	yellow brown Sand	to whitish-grayish brown fine-coarse sized; subangular-rounded loosly consolidated; Quartz in coated Iron oxid?
22	29	Silicified Calcrete	in white sandy matrix; consolidated brecciated fragments up to pebble size (ø up to 10-15 cm); some laminatia.
29	107	Oxidised, weathered chlorite schist	x fine schistosity; greenish grey fragments white bands: Calcitic (HCL: foams) x rost brown bands: limonite? / Iron oxide
		NB 54 m	Quartz band, smaller bands do occur elsewhere
107	125	less weathered chlorite schist	more bluish grey in colour Schistosity; silk glow; pyrite up to 3% (±)
125	206 (EOH)	"fresh" chlorite schist	pyrite; calcite; (foams with HCl) Quartz etc. N.B. graphitic in some places

K
A
L
A
H
A
R
I

ANNEX 1 – BOREHOLE DESCRIPTION LOGS

FORMATION LOG SHEET

Page 1 of __

Date drilled: 12/6/95 – 14/6/95
Date logged: 12/6/95 – 14/6/95
Geologist: EdE
Latitude: 20° 28'.16 S

Hole number: WW 35040.
Project: GAM
Location: JIGT 95b/2
Longitude: 20° 21.15 E

From	To	Rock Type	Description
0	1	Soil	
1	5	Calcrete in sand matrix	Calcrete in fine-coarse white sand matrix
			(sub)angular – rounded fragments Calcite
			Cement. Quartz sand
5	10	white sand	sand idem to above; less calcite
			cement. loosely consolidated
10	16	yellow brown sand	idem; no Calcite cement / reddish coating around
16	32	reddish ~~bro~~ sand	some of Quartz grains (cont idem)
32	39	yellow sand	clean fine-coarse sand; (sub)rounded
			reason well sorted No calcite cement
39	45	white-pinkish white	sorting poor silt – fine sand, some
		sand	coarser fragments; no Cement; Quartz
			not coated.
45	56	light reddish sands.	idem
56	63	reddish sandstones.	fine – medium grained sandstones,
63	74	yellow	(sub)rounded; mainly Quartz grains
74	82	white	some calcite cement and silcrete fragments
82	83	red brown transition	greyish brown – reddish brown oxidised
83	185	weathered/oxidised	mica schist (almost phyllitic)
		mica schists	very fine (dusty) material, only small
			amount of larger chips.
		NB Minor Quartz – Feldspathic bands at	100-101 m / 107-109 m / 136-137 m
			167-167 m: larger (in scale) Quartz + Feldspathic fragments
		NB Some more "fresher" zones: more grey in colour	
			113-115 m / 138-139 m / 145-160 m
185	205	"Fresh" mica schist	grey in colour.
	EOM		

Ox. weathered Mica Schist

Fresh Schist

ANNEX 1 – BOREHOLE DESCRIPTION LOGS

FORMATION LOG SHEET

Page __ of __

Date drilled: 29/7/95 - 31/7/95
Date logged: 29/7/95 - 31/7/95
Geologist: EdE
Latitude: 20° 21.49' S

Hole number: WW35044
Project: GAw
Location: TGT 96C
Longitude: 20° 26.30' E

From	To	Rock Type	Description
0	10	Aeolian unconsolidated	Orange-yellow; (unconsolidated) mainly fine - some coarser
		orange yellow sand	particles: poorly sorted, well rounded grains
			mostly Quartz, showing orange coating.
			N.b. silt-clay rich
10	13	Calcrete in sand	sand: idem, as above.
			Calcrete.
13	45	White consolidated sandstone	Consolidated (carbonate cement: foams with HCL)
			fine-coarse sand: with silty-clayey matrix
			poorly sorted. most grains slightly coated: orange
			hard "lumps" (granule size) of clay present.
			Nb grains: well rounded, usually quartz.
			Some silcrete fragments (e.g. 18m)
45	98	black-grey oxidised schist.	black grey schist; soft: friable: very micaceous
			slightly oxidised-weathered; Nb biotite rich.
			some small veins = Quartzo-Feldspatic material
		*	No magnetic material
		*	No calcitic "
		Nb 98.5m Strike	Almost clean water, even during drilling
			first indication (after drilling) = 38-39mm on V ≈ 1.5m³/h
98	103	Quartzite	red-whitish Quartzite: large fragments
103	110	fresh mica schist.	
	EOH		

ANNEX 1 – BOREHOLE DESCRIPTION LOGS

FORMATION LOG SHEET

Page __ of __

Date drilled: 2/8/95 - 4/8/95
Date logged: 2/8/95 - 4/8/95
Geologist: EdE
Latitude: 20° 18.355'S

Hole number: T85b WW35045
Project: GAM
Location: T85b
Longitude: 20° 06.620'E

From	To	Rock Type	Description
0	1	Soil	
1	19	unconsolidated sand	white, yellow, beige unconsolidated very
			silty-clayey medium-coarse sand.
			subrounded, mainly quartzitic grains
		Nb 3m	Calcitic cement;
19	48	white-pinkish sandstone	Semi consolidated sandstone; clay-silt rich
			Quartzitic, subrounded grains, poorly sorted
			Calcitic cement (HCl: foams)
		nb 41.	~~wet~~ with clay fragments: pebble size.
		41-48	more cemented → harder.
48	49	Transition zone	Sandstone + schist mixture
49	104	Granitic banded Gneiss	banded gneiss; very rich in quartz and
		+ Schist.	k-feldspar → Granitic
			* micaceous, muscovite rich schist; biotite
		71. nb 73, 74	Pyrite very dark in colour => 2 m schist band.
		Nb 75	large (cm scale) muscovite flakes
		Nb	Not magnetic.
		95-96 Nb 96-97	muscovite flakes. damp.
		98	Strike in very fine quartz. I 35-36 mm V: ≈ 1.2 m³/h
104	116	fresh Schist.	

ANNEX 2 – BOREHOLE SPECTRAL MEASUREMENTS TABLES

Borehole WW34851

Depth	Band 1	Band 2	Band 3	Band 4	Band 5	Band 6	Band 7	Band 8	Band 9	Ferric oxide content	Ferric oxide composition	Ferrous iron index	Opaque index	AlOH group content	AlOH group composition	Kaolin group index	FeOH group content	MgOH group content	MgOH group composition	Ferrous iron content in MgOH
0-2	0.289	0.346	0.406	0.495	0.436	0.417	0.401	0.378	0.362	1.219	1.198	0.881	0.583	2.010	1.086	0.956	1.980	0.999	1.061	0.881
2-9	0.318	0.376	0.451	0.546	0.465	0.418	0.404	0.391	0.358	1.211	1.183	0.852	0.583	2.081	1.153	0.898	2.004	0.976	1.031	0.852
9-36	0.350	0.435	0.502	0.561	0.472	0.428	0.438	0.414	0.370	1.117	1.245	0.841	0.623	2.128	1.076	0.907	1.919	0.936	1.060	0.841
36-47	0.475	0.561	0.613	0.687	0.631	0.587	0.582	0.548	0.511	1.119	1.183	0.919	0.691	2.067	1.083	0.930	1.950	0.971	1.062	0.919
47-60	0.211	0.371	0.447	0.583	0.494	0.458	0.485	0.451	0.407	1.305	1.758	0.847	0.361	2.140	1.018	0.926	1.872	0.924	1.077	0.847
60-63	0.264	0.374	0.438	0.519	0.424	0.382	0.396	0.368	0.325	1.186	1.417	0.817	0.508	2.150	1.070	0.900	1.891	0.924	1.077	0.817
63-65	0.289	0.409	0.492	0.580	0.453	0.403	0.428	0.387	0.336	1.178	1.418	0.781	0.497	2.184	1.060	0.890	1.849	0.907	1.104	0.781
65-93	0.349	0.415	0.449	0.485	0.426	0.391	0.391	0.352	0.305	1.079	1.190	0.879	0.720	2.086	1.090	0.919	1.903	0.938	1.110	0.879
93-113	0.188	0.246	0.271	0.334	0.317	0.305	0.282	0.267	0.278	1.229	1.307	0.951	0.563	1.963	1.125	0.962	2.028	1.062	1.057	0.951
113-132	0.278	0.331	0.367	0.450	0.419	0.366	0.370	0.351	0.345	1.227	1.191	0.932	0.617	2.158	1.133	0.872	1.936	0.986	1.055	0.932
132-150	0.299	0.325	0.345	0.400	0.381	0.335	0.344	0.331	0.320	1.161	1.088	0.952	0.747	2.161	1.107	0.881	1.938	0.970	1.038	0.952
170-190	0.216	0.232	0.243	0.303	0.276	0.222	0.229	0.212	0.201	1.250	1.070	0.910	0.713	2.270	1.207	0.805	1.900	0.961	1.078	0.910
190-210	0.288	0.309	0.322	0.372	0.358	0.313	0.318	0.303	0.294	1.154	1.074	0.962	0.773	2.159	1.126	0.874	1.940	0.977	1.047	0.962
210-221	0.285	0.304	0.316	0.353	0.326	0.278	0.285	0.272	0.260	1.119	1.068	0.923	0.807	2.201	1.146	0.851	1.929	0.966	1.048	0.923

Borehole WW34873

Depth	Band 1	Band 2	Band 3	Band 4	Band 5	Band 6	Band 7	Band 8	Band 9	Ferric oxide content	Ferric oxide composition	Ferrous iron index	Opaque index	AlOH group content	AlOH group composition	Kaolin group index	FeOH group content	MgOH group content	MgOH group composition	Ferrous iron content in MgOH
0-21	0.097	0.243	0.313	0.455	0.389	0.366	0.395	0.368	0.343	1.455	2.508	0.856	0.213	2.142	0.987	0.940	1.860	0.930	1.072	0.856
21-68	0.187	0.300	0.365	0.448	0.387	0.348	0.355	0.326	0.295	1.226	1.608	0.864	0.418	2.132	1.089	0.900	1.898	0.943	1.089	0.864
68-81	0.240	0.331	0.372	0.436	0.405	0.382	0.376	0.347	0.324	1.172	1.380	0.929	0.549	2.046	1.076	0.943	1.936	0.976	1.086	0.929
81-91	0.167	0.227	0.255	0.294	0.280	0.265	0.261	0.235	0.228	1.155	1.360	0.954	0.567	2.041	1.073	0.947	1.916	0.994	1.110	0.954
91-96	0.173	0.264	0.305	0.368	0.334	0.303	0.304	0.276	0.250	1.204	1.530	0.910	0.470	2.105	1.101	0.906	1.906	0.954	1.101	0.910
96-175	0.165	0.267	0.346	0.446	0.417	0.386	0.390	0.359	0.330	1.292	1.622	0.935	0.369	2.092	1.071	0.924	1.911	0.956	1.086	0.935
175-250	0.108	0.127	0.126	0.146	0.103	0.100	0.095	0.089	0.086	1.159	1.183	0.707	0.737	1.973	1.087	0.973	1.990	1.015	1.072	0.707

WW34876

Depth	Band 1	Band 2	Band 3	Band 4	Band 5	Band 6	Band 7	Band 8	Band 9	Ferric oxide content	Ferric oxide composition	Ferrous iron index	Opaque index	AlOH group content	AlOH group composition	Kaolin group index	FeOH group content	MgOH group content	MgOH group composition	Ferrous iron content in MgOH
0-2	0.137	0.270	0.381	0.569	0.460	0.425	0.459	0.423	0.382	1.494	1.973	0.807	0.240	2.164	1.001	0.924	1.845	0.914	1.087	0.807
2-12	0.348	0.427	0.483	0.562	0.471	0.427	0.439	0.394	0.341	1.163	1.228	0.838	0.619	2.132	1.072	0.906	1.870	0.921	1.114	0.838
12-32	0.292	0.393	0.450	0.572	0.541	0.512	0.511	0.466	0.427	1.270	1.345	0.946	0.511	2.057	1.059	0.945	1.912	0.960	1.097	0.946
32-46	0.193	0.244	0.261	0.323	0.306	0.283	0.284	0.257	0.243	1.236	1.260	0.948	0.600	2.083	1.075	0.927	1.900	0.973	1.107	0.948
46-51	0.170	0.189	0.187	0.158	0.142	0.138	0.136	0.129	0.129	0.844	1.111	0.901	1.080	2.012	1.045	0.973	1.961	1.011	1.059	0.901
51-54	0.178	0.229	0.240	0.254	0.225	0.211	0.215	0.198	0.191	1.055	1.288	0.886	0.700	2.079	1.046	0.941	1.907	0.974	1.084	0.886
54-76	0.182	0.219	0.230	0.257	0.234	0.217	0.225	0.206	0.191	1.114	1.202	0.913	0.709	2.119	1.043	0.924	1.879	0.946	1.093	0.913
76-84	0.120	0.139	0.138	0.137	0.127	0.124	0.122	0.118	0.116	0.989	1.164	0.927	0.874	2.004	1.039	0.979	1.984	1.001	1.035	0.927
84-92	0.132	0.153	0.153	0.158	0.148	0.144	0.141	0.135	0.132	1.032	1.159	0.936	0.836	2.012	1.045	0.973	1.974	0.997	1.044	0.936
92-104	0.115	0.145	0.145	0.135	0.118	0.114	0.113	0.107	0.105	0.932	1.264	0.876	0.850	2.037	1.046	0.960	1.952	0.991	1.055	0.876
104-112	0.140	0.146	0.142	0.129	0.117	0.115	0.115	0.112	0.110	0.909	1.045	0.908	1.084	2.014	1.024	0.981	1.980	0.996	1.026	0.908
112-143	0.135	0.157	0.155	0.151	0.143	0.140	0.138	0.134	0.131	0.974	1.162	0.945	0.893	2.002	1.036	0.982	1.987	1.001	1.031	0.945
143-146	0.119	0.142	0.140	0.134	0.125	0.123	0.122	0.119	0.118	0.955	1.194	0.931	0.886	2.009	1.025	0.983	1.987	0.999	1.021	0.931
146-160	0.123	0.140	0.139	0.131	0.121	0.117	0.117	0.114	0.113	0.944	1.144	0.921	0.937	2.020	1.035	0.974	1.982	1.000	1.026	0.921
160-190	0.122	0.125	0.122	0.112	0.104	0.102	0.102	0.100	0.099	0.912	1.025	0.933	1.092	2.013	1.021	0.984	1.986	0.996	1.018	0.933
190-220	0.131	0.133	0.130	0.123	0.115	0.114	0.112	0.111	0.110	0.941	1.017	0.936	1.065	1.998	1.023	0.990	2.000	1.004	1.013	0.936
220-250	0.102	0.103	0.100	0.088	0.081	0.080	0.079	0.077	0.076	0.880	1.015	0.919	1.153	2.005	1.034	0.981	1.992	1.001	1.023	0.919
250-280	0.092	0.091	0.088	0.079	0.073	0.072	0.071	0.069	0.069	0.894	0.996	0.927	1.167	1.999	1.033	0.985	1.997	1.006	1.020	0.927
280-310	0.148	0.156	0.154	0.153	0.146	0.143	0.140	0.136	0.134	0.997	1.054	0.950	0.964	2.003	1.038	0.981	1.986	1.003	1.032	0.950
310-340	0.146	0.151	0.148	0.140	0.132	0.130	0.128	0.125	0.124	0.945	1.035	0.944	1.046	1.997	1.032	0.986	1.994	1.004	1.024	0.944
340-363	0.174	0.186	0.185	0.185	0.174	0.172	0.170	0.167	0.166	0.999	1.070	0.942	0.939	2.004	1.026	0.985	1.991	1.003	1.020	0.942

ANNEX 2 – BOREHOLE SPECTRAL MEASUREMENTS TABLES

WW35037

Depth	Band 1	Band 2	Band 3	Band 4	Band 5	Band 6	Band 7	Band 8	Band 9	Ferric oxide content	Ferric oxide composition	Ferrous iron index	Opaque index	AlOH group content	AlOH group composition	Kaolin group index	FeOH group content	MgOH group content	MgOH group composition	Ferrous iron content in MgOH
0-5	0.223	0.283	0.355	0.486	0.412	0.370	0.367	0.339	0.302	1.367	1.265	0.848	0.460	2.108	1.121	0.897	1.930	0.951	1.082	0.848
5-14	0.255	0.312	0.375	0.418	0.336	0.297	0.301	0.276	0.239	1.115	1.224	0.806	0.611	2.145	1.119	0.883	1.906	0.930	1.089	0.806
14-32	0.211	0.343	0.402	0.452	0.370	0.329	0.342	0.313	0.271	1.125	1.625	0.819	0.468	2.162	1.083	0.890	1.879	0.917	1.093	0.819
32-37	0.266	0.370	0.426	0.462	0.399	0.358	0.363	0.337	0.296	1.085	1.392	0.865	0.576	2.130	1.099	0.897	1.911	0.934	1.080	0.865
37-44	0.433	0.495	0.535	0.540	0.453	0.426	0.402	0.347	0.331	1.008	1.144	0.840	0.803	2.008	1.128	0.939	1.923	1.011	1.158	0.840
44-55	0.351	0.405	0.444	0.444	0.361	0.328	0.306	0.264	0.260	0.999	1.155	0.814	0.791	2.036	1.180	0.908	1.933	1.031	1.160	0.814
55-63	0.389	0.447	0.474	0.480	0.407	0.377	0.368	0.321	0.290	1.013	1.148	0.848	0.811	2.057	1.108	0.925	1.897	0.968	1.146	0.848
63-67	0.263	0.376	0.416	0.462	0.406	0.375	0.370	0.328	0.296	1.110	1.428	0.878	0.570	2.069	1.098	0.924	1.902	0.962	1.127	0.878
67-81	0.265	0.348	0.383	0.435	0.392	0.369	0.354	0.321	0.307	1.137	1.312	0.902	0.610	2.022	1.107	0.941	1.948	1.002	1.105	0.902
81-100	0.118	0.178	0.214	0.380	0.375	0.342	0.356	0.328	0.317	1.777	1.504	0.987	0.311	2.134	1.054	0.913	1.885	0.965	1.084	0.987
100-103	0.138	0.204	0.240	0.399	0.393	0.360	0.372	0.345	0.337	1.664	1.472	0.984	0.346	2.125	1.058	0.915	1.897	0.972	1.076	0.984
103-112	0.105	0.161	0.187	0.304	0.298	0.274	0.283	0.262	0.256	1.626	1.531	0.980	0.345	2.124	1.056	0.917	1.894	0.972	1.079	0.980
112-127	0.122	0.199	0.226	0.346	0.332	0.308	0.317	0.297	0.291	1.531	1.634	0.960	0.352	2.109	1.048	0.926	1.907	0.976	1.069	0.960
127-130	0.124	0.203	0.223	0.313	0.298	0.278	0.284	0.267	0.262	1.404	1.640	0.952	0.397	2.097	1.049	0.931	1.917	0.980	1.064	0.952
130-133	0.125	0.218	0.247	0.385	0.380	0.357	0.365	0.342	0.334	1.556	1.747	0.987	0.325	2.088	1.041	0.939	1.915	0.977	1.066	0.987
133-135	0.153	0.228	0.244	0.309	0.297	0.283	0.286	0.272	0.269	1.265	1.495	0.962	0.494	2.060	1.041	0.951	1.943	0.990	1.050	0.962
135-137	0.140	0.197	0.206	0.243	0.227	0.215	0.216	0.205	0.201	1.180	1.404	0.936	0.577	2.059	1.051	0.947	1.942	0.989	1.057	0.936
137-140	0.144	0.212	0.223	0.270	0.252	0.242	0.243	0.232	0.229	1.210	1.474	0.936	0.533	2.051	1.037	0.958	1.945	0.992	1.051	0.936
140-144	0.162	0.220	0.228	0.264	0.247	0.236	0.238	0.228	0.225	1.157	1.359	0.935	0.614	2.053	1.035	0.958	1.950	0.989	1.044	0.935
144-145	0.145	0.210	0.219	0.257	0.241	0.230	0.233	0.222	0.219	1.176	1.443	0.936	0.565	2.056	1.034	0.957	1.945	0.986	1.047	0.936
145-149	0.148	0.202	0.208	0.237	0.219	0.210	0.212	0.204	0.202	1.141	1.366	0.924	0.622	2.051	1.032	0.960	1.951	0.990	1.042	0.924
149-151	0.154	0.221	0.232	0.281	0.267	0.255	0.258	0.247	0.244	1.213	1.435	0.947	0.546	2.055	1.032	0.958	1.947	0.988	1.044	0.947
151-159	0.170	0.217	0.221	0.230	0.208	0.200	0.202	0.194	0.192	1.042	1.276	0.904	0.741	2.047	1.032	0.962	1.957	0.991	1.037	0.904
159-160	0.253	0.320	0.334	0.345	0.318	0.312	0.310	0.302	0.300	1.032	1.265	0.922	0.734	2.016	1.025	0.980	1.977	1.000	1.029	0.922
160-164	0.150	0.199	0.202	0.210	0.191	0.184	0.185	0.179	0.178	1.040	1.323	0.908	0.716	2.043	1.031	0.964	1.962	0.994	1.033	0.908
164-165	0.151	0.203	0.208	0.222	0.205	0.198	0.199	0.193	0.191	1.066	1.348	0.923	0.681	2.043	1.027	0.966	1.960	0.992	1.033	0.923
165-174	0.154	0.199	0.201	0.204	0.187	0.180	0.182	0.175	0.172	1.015	1.292	0.918	0.756	2.045	1.030	0.964	1.955	0.988	1.039	0.918
174-181	0.147	0.197	0.197	0.186	0.165	0.160	0.160	0.155	0.154	0.945	1.338	0.888	0.792	2.038	1.031	0.967	1.966	0.992	1.031	0.888
181-201	0.130	0.146	0.142	0.125	0.111	0.108	0.107	0.104	0.102	0.882	1.121	0.889	1.038	2.029	1.036	0.969	1.969	0.994	1.036	0.889

WW35039

Depth	Band 1	Band 2	Band 3	Band 4	Band 5	Band 6	Band 7	Band 8	Band 9	Ferric oxide content	Ferric oxide composition	Ferrous iron index	Opaque index	AlOH group content	AlOH group composition	Kaolin group index	FeOH group content	MgOH group content	MgOH group composition	Ferrous iron content in MgOH
0-2	0.128	0.154	0.201	0.388	0.336	0.301	0.304	0.284	0.250	1.933	1.208	0.867	0.330	2.126	1.105	0.896	1.924	0.937	1.071	0.867
2-11	0.244	0.284	0.329	0.359	0.275	0.242	0.245	0.226	0.197	1.093	1.161	0.765	0.680	2.148	1.122	0.880	1.911	0.931	1.084	0.765
11-22	0.231	0.356	0.410	0.449	0.354	0.315	0.321	0.291	0.257	1.094	1.536	0.789	0.516	2.139	1.104	0.891	1.890	0.936	1.103	0.789
22-29	0.280	0.317	0.338	0.330	0.267	0.244	0.234	0.213	0.194	0.976	1.130	0.810	0.851	2.052	1.143	0.914	1.956	0.982	1.097	0.810
29-41	0.249	0.291	0.316	0.334	0.289	0.269	0.263	0.240	0.230	1.058	1.170	0.865	0.744	2.054	1.097	0.931	1.932	0.991	1.097	0.865
41-49	0.230	0.269	0.286	0.293	0.258	0.238	0.235	0.215	0.206	1.026	1.170	0.880	0.785	2.073	1.097	0.922	1.925	0.985	1.095	0.880
49-65	0.156	0.180	0.182	0.182	0.162	0.155	0.151	0.142	0.139	0.997	1.153	0.890	0.860	2.017	1.072	0.958	1.969	1.003	1.062	0.890
65-83	0.164	0.188	0.189	0.174	0.151	0.145	0.144	0.135	0.131	0.922	1.143	0.868	0.943	2.042	1.051	0.956	1.942	0.988	1.066	0.868
83-107	0.135	0.164	0.163	0.159	0.139	0.134	0.133	0.127	0.124	0.976	1.214	0.875	0.848	2.029	1.048	0.963	1.965	0.993	1.046	0.875
107-125	0.147	0.155	0.151	0.146	0.129	0.122	0.122	0.115	0.112	0.968	1.054	0.880	1.003	2.068	1.053	0.943	1.932	0.984	1.064	0.880
125-153	0.137	0.141	0.137	0.121	0.109	0.107	0.106	0.104	0.103	0.883	1.030	0.905	1.133	2.009	1.030	0.981	1.989	1.001	1.022	0.905
153-176	0.138	0.150	0.148	0.136	0.121	0.118	0.117	0.114	0.112	0.916	1.088	0.893	1.018	2.020	1.033	0.975	1.979	0.996	1.028	0.893
176-191	0.153	0.162	0.158	0.137	0.123	0.120	0.119	0.115	0.113	0.867	1.064	0.898	1.113	2.013	1.039	0.975	1.979	1.000	1.035	0.898

ANNEX 2 – BOREHOLE SPECTRAL MEASUREMENTS TABLES

WW35040

Depth	Band 1	Band 2	Band 3	Band 4	Band 5	Band 6	Band 7	Band 8	Band 9	Ferric oxide content	Ferric oxide composition	Ferrous iron index	Opaque index	AlOH group content	AlOH group composition	Kaolin group index	FeOH group content	MgOH group content	MgOH group composition	Ferrous iron content in MgOH
0-1	0.156	0.232	0.316	0.523	0.435	0.397	0.404	0.376	0.336	1.653	1.486	0.831	0.299	2.110	1.077	0.914	1.917	0.940	1.073	0.831
1-5	0.349	0.418	0.482	0.522	0.433	0.396	0.391	0.365	0.334	1.083	1.198	0.830	0.669	2.082	1.106	0.915	1.944	0.965	1.073	0.830
5-10	0.300	0.376	0.456	0.509	0.411	0.362	0.371	0.343	0.302	1.117	1.252	0.807	0.589	2.160	1.107	0.881	1.899	0.931	1.083	0.807
10-16	0.200	0.294	0.362	0.417	0.322	0.284	0.295	0.265	0.235	1.154	1.470	0.771	0.479	2.173	1.092	0.881	1.863	0.926	1.110	0.771
16-32	0.162	0.310	0.383	0.471	0.376	0.333	0.349	0.314	0.276	1.232	1.914	0.797	0.344	2.175	1.077	0.887	1.856	0.918	1.110	0.797
32-39	0.289	0.407	0.477	0.538	0.464	0.414	0.418	0.385	0.338	1.127	1.411	0.863	0.536	2.130	1.110	0.892	1.912	0.937	1.086	0.863
39-45	0.485	0.568	0.628	0.658	0.570	0.534	0.514	0.456	0.425	1.048	1.172	0.865	0.737	2.029	1.109	0.938	1.927	0.989	1.127	0.865
45-56	0.364	0.463	0.529	0.585	0.510	0.456	0.460	0.425	0.373	1.106	1.272	0.872	0.623	2.128	1.108	0.894	1.915	0.936	1.082	0.872
56-63	0.399	0.438	0.455	0.447	0.383	0.357	0.351	0.311	0.281	0.982	1.099	0.857	0.892	2.058	1.090	0.932	1.902	0.963	1.128	0.857
63-74	0.276	0.380	0.425	0.475	0.432	0.406	0.400	0.362	0.332	1.119	1.379	0.910	0.580	2.048	1.082	0.940	1.923	0.968	1.103	0.910
74-82	0.304	0.382	0.415	0.466	0.421	0.393	0.391	0.356	0.324	1.122	1.257	0.905	0.652	2.064	1.079	0.934	1.919	0.960	1.097	0.905
82-95	0.177	0.258	0.314	0.560	0.566	0.523	0.543	0.507	0.496	1.781	1.457	1.012	0.317	2.123	1.043	0.923	1.896	0.970	1.072	1.012
95-110	0.126	0.194	0.236	0.430	0.442	0.410	0.424	0.397	0.392	1.825	1.539	1.028	0.293	2.112	1.042	0.928	1.903	0.976	1.068	1.028
110-120	0.139	0.224	0.263	0.473	0.472	0.432	0.448	0.415	0.403	1.794	1.611	0.998	0.294	2.127	1.052	0.917	1.889	0.968	1.082	0.998
120-129	0.150	0.241	0.277	0.468	0.472	0.438	0.452	0.424	0.418	1.691	1.600	1.008	0.321	2.107	1.042	0.930	1.906	0.977	1.067	1.008
129-138	0.152	0.236	0.260	0.394	0.389	0.367	0.377	0.357	0.351	1.517	1.553	0.988	0.385	2.086	1.032	0.944	1.920	0.979	1.057	0.988
138-145	0.164	0.252	0.273	0.400	0.393	0.373	0.382	0.362	0.355	1.465	1.538	0.983	0.410	2.078	1.029	0.949	1.922	0.979	1.057	0.983
145-155	0.146	0.202	0.210	0.257	0.240	0.228	0.231	0.218	0.214	1.224	1.388	0.934	0.568	2.068	1.038	0.950	1.931	0.984	1.057	0.934
155-175	0.149	0.209	0.222	0.289	0.273	0.261	0.264	0.249	0.247	1.302	1.409	0.946	0.514	2.059	1.037	0.954	1.933	0.991	1.059	0.946
175-185	0.166	0.237	0.249	0.295	0.280	0.270	0.274	0.263	0.260	1.186	1.428	0.949	0.562	2.054	1.023	0.963	1.947	0.986	1.040	0.949
185-205	0.129	0.160	0.160	0.160	0.144	0.139	0.140	0.135	0.134	0.998	1.237	0.903	0.808	2.039	1.031	0.966	1.960	0.995	1.038	0.903

WW35044

Depth	Band 1	Band 2	Band 3	Band 4	Band 5	Band 6	Band 7	Band 8	Band 9	Ferric oxide content	Ferric oxide composition	Ferrous iron index	Opaque index	AlOH group content	AlOH group composition	Kaolin group index	FeOH group content	MgOH group content	MgOH group composition	Ferrous iron content in MgOH
0-10	0.200	0.361	0.437	0.548	0.520	0.502	0.523	0.503	0.484	1.252	1.803	0.949	0.365	2.078	0.995	0.965	1.924	0.961	1.038	0.949
10-13	0.252	0.363	0.418	0.496	0.424	0.389	0.396	0.366	0.328	1.187	1.437	0.853	0.508	2.105	1.070	0.919	1.908	0.941	1.081	0.853
13-20	0.369	0.451	0.488	0.533	0.475	0.445	0.439	0.390	0.360	1.092	1.224	0.891	0.692	2.052	1.083	0.937	1.905	0.971	1.124	0.891
20-34	0.259	0.365	0.404	0.471	0.442	0.418	0.417	0.384	0.355	1.164	1.406	0.938	0.551	2.052	1.060	0.947	1.926	0.966	1.085	0.938
34-45	0.323	0.407	0.457	0.556	0.534	0.516	0.505	0.466	0.450	1.215	1.260	0.961	0.582	2.014	1.058	0.966	1.945	0.994	1.083	0.961
45-50	0.161	0.174	0.183	0.214	0.207	0.197	0.189	0.176	0.172	1.168	1.080	0.969	0.756	2.007	1.095	0.953	1.973	1.012	1.076	0.969
50-85	0.193	0.221	0.232	0.249	0.216	0.203	0.199	0.184	0.168	1.072	1.146	0.869	0.776	2.052	1.086	0.936	1.939	0.968	1.084	0.869
85-94	0.174	0.191	0.197	0.212	0.197	0.188	0.184	0.174	0.163	1.076	1.100	0.926	0.818	2.025	1.067	0.957	1.963	0.981	1.061	0.926
94-98	0.193	0.233	0.244	0.300	0.291	0.281	0.278	0.261	0.252	1.226	1.210	0.973	0.644	2.029	1.047	0.964	1.945	0.989	1.068	0.973
98-103	0.163	0.199	0.209	0.301	0.330	0.315	0.289	0.258	0.259	1.443	1.223	1.095	0.540	1.963	1.141	0.956	1.984	1.050	1.120	1.095
103-110	0.124	0.136	0.138	0.170	0.176	0.172	0.166	0.158	0.156	1.235	1.099	1.036	0.731	1.983	1.061	0.979	1.989	1.016	1.053	1.036

WW35045

Depth	Band 1	Band 2	Band 3	Band 4	Band 5	Band 6	Band 7	Band 8	Band 9	Ferric oxide content	Ferric oxide composition	Ferrous iron index	Opaque index	AlOH group content	AlOH group composition	Kaolin group index	FeOH group content	MgOH group content	MgOH group composition	Ferrous iron content in MgOH
0	0.272	0.360	0.440	0.524	0.446	0.401	0.412	0.380	0.336	1.189	1.327	0.852	0.519	2.139	1.084	0.899	1.897	0.932	1.084	0.852
19	0.329	0.410	0.459	0.534	0.493	0.463	0.458	0.413	0.381	1.162	1.246	0.924	0.616	2.056	1.077	0.938	1.912	0.968	1.109	0.924
40	0.385	0.460	0.514	0.640	0.590	0.550	0.534	0.473	0.470	1.245	1.196	0.921	0.601	2.042	1.105	0.933	1.916	1.013	1.129	0.921
48	0.144	0.157	0.162	0.233	0.282	0.244	0.245	0.210	0.206	1.436	1.086	1.213	0.621	2.158	1.153	0.866	1.856	0.990	1.164	1.213
62	0.114	0.121	0.121	0.145	0.165	0.145	0.155	0.141	0.134	1.195	1.067	1.139	0.788	2.210	1.061	0.879	1.841	0.941	1.101	1.139
72	0.109	0.120	0.124	0.182	0.261	0.262	0.256	0.242	0.247	1.471	1.101	1.432	0.599	1.973	1.018	1.005	1.968	1.020	1.058	1.432
74	0.190	0.206	0.222	0.252	0.236	0.202	0.223	0.204	0.194	1.135	1.086	0.937	0.755	2.271	1.056	0.857	1.819	0.926	1.094	0.937
95	0.334	0.354	0.380	0.569	0.596	0.515	0.571	0.516	0.497	1.496	1.059	1.048	0.587	2.266	1.044	0.864	1.807	0.931	1.105	1.048
98	0.207	0.221	0.233	0.324	0.302	0.228	0.279	0.232	0.215	1.390	1.069	0.932	0.637	2.551	1.082	0.754	1.649	0.865	1.201	0.932
103	0.146	0.146	0.147	0.205	0.260	0.251	0.239	0.216	0.221	1.396	0.999	1.267	0.711	1.987	1.089	0.966	1.957	1.038	1.105	1.267

ANNEX 3 – BOREHOLE BAND RATIO COMBINATION GRAPHS

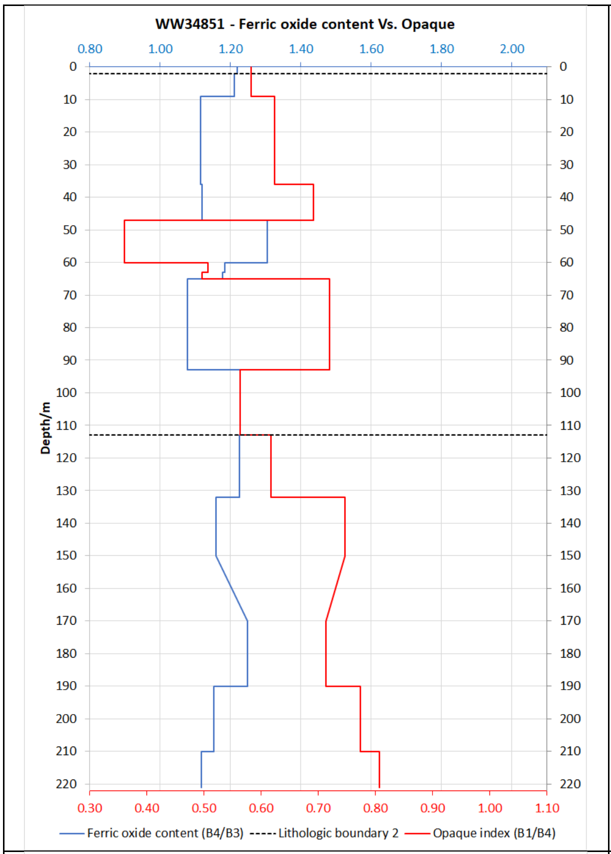

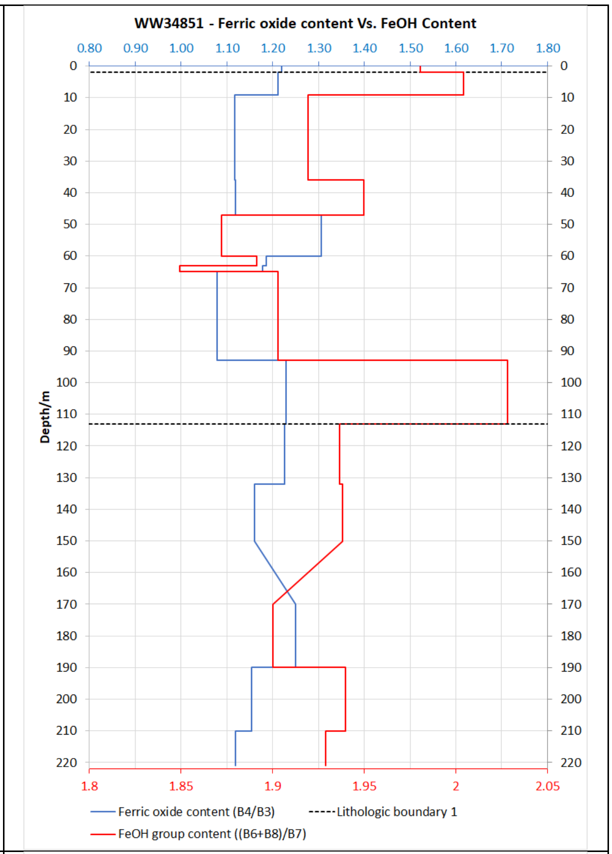

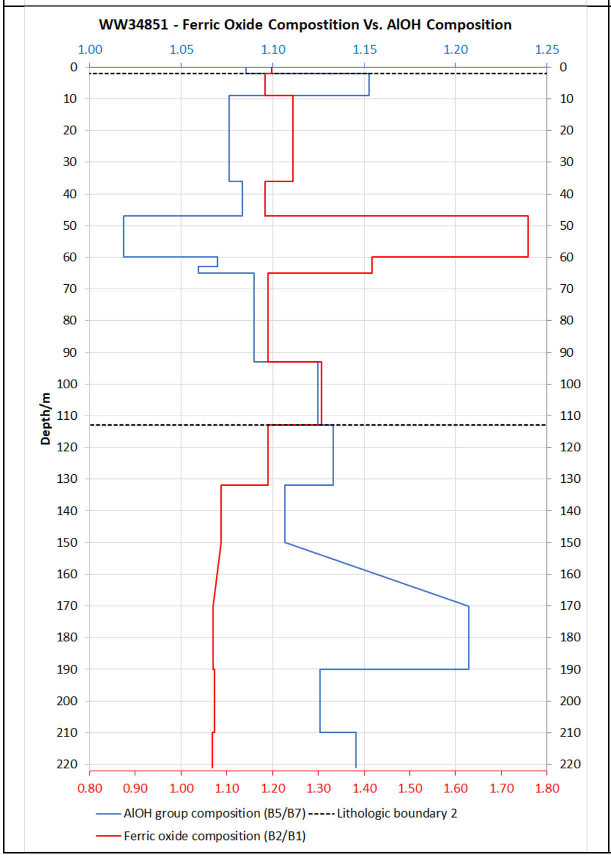

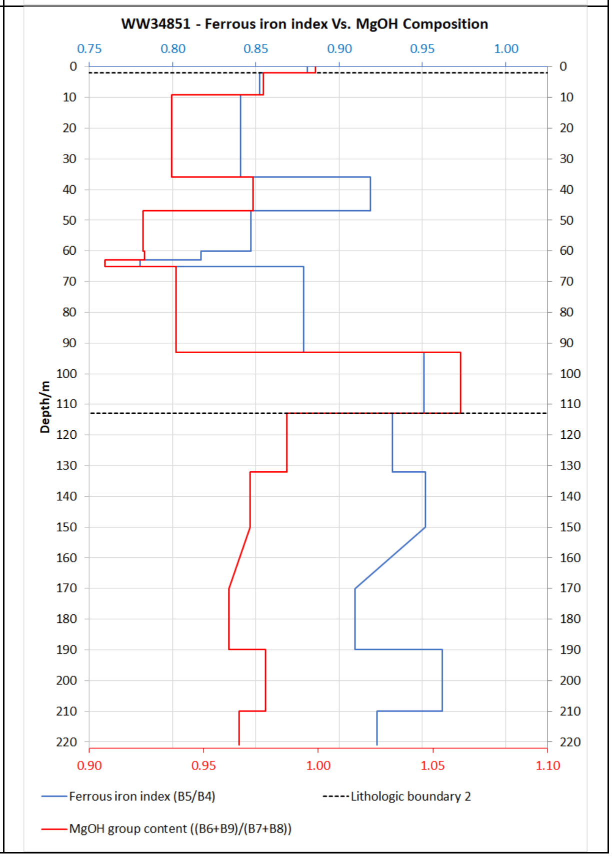

ANNEX 3 – BOREHOLE BAND RATIO COMBINATION GRAPHS

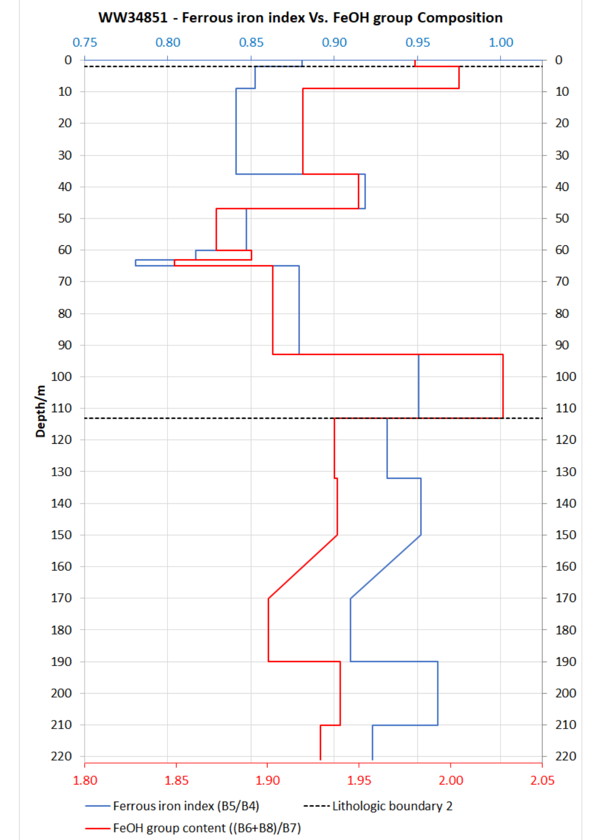

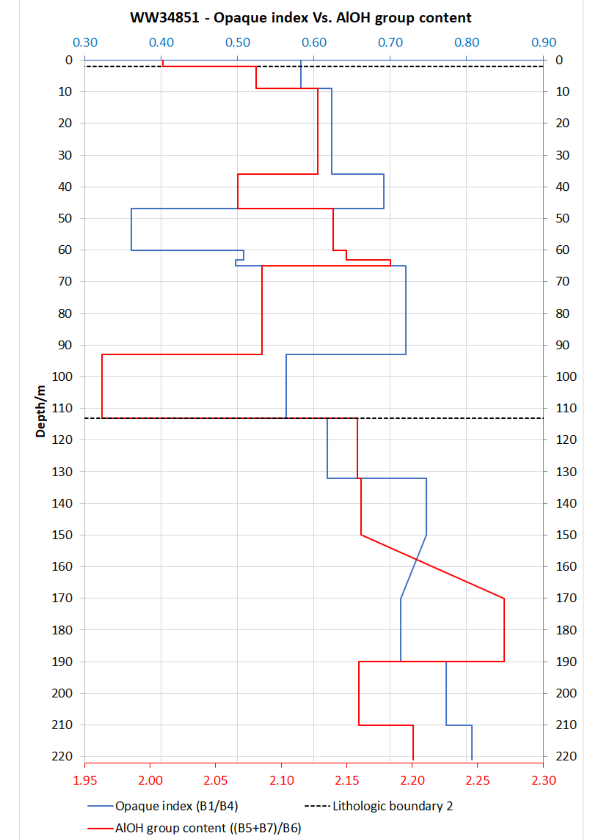

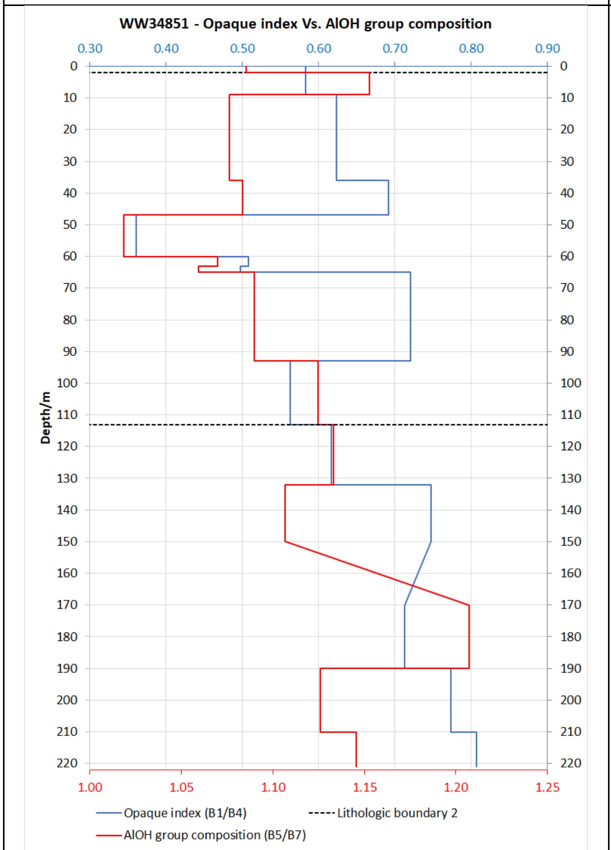

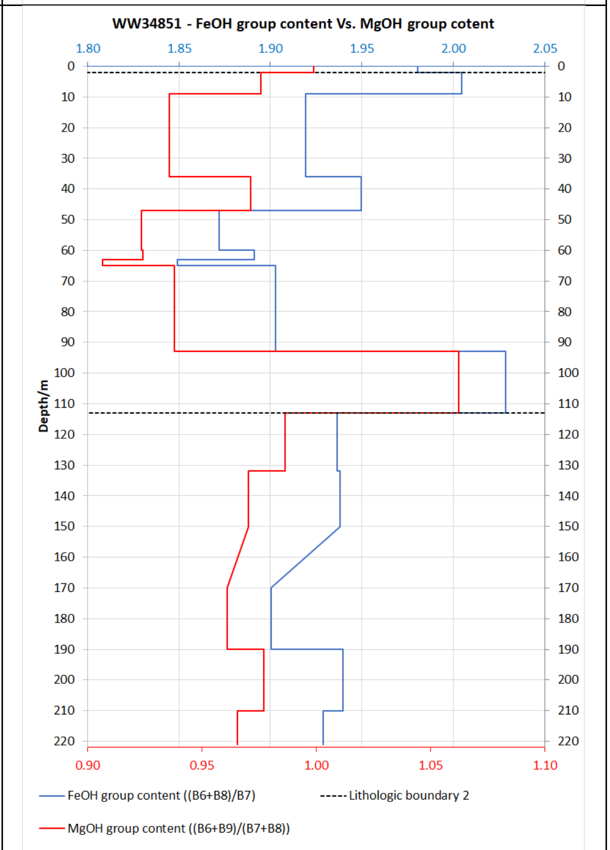

ANNEX 3 – BOREHOLE BAND RATIO COMBINATION GRAPHS

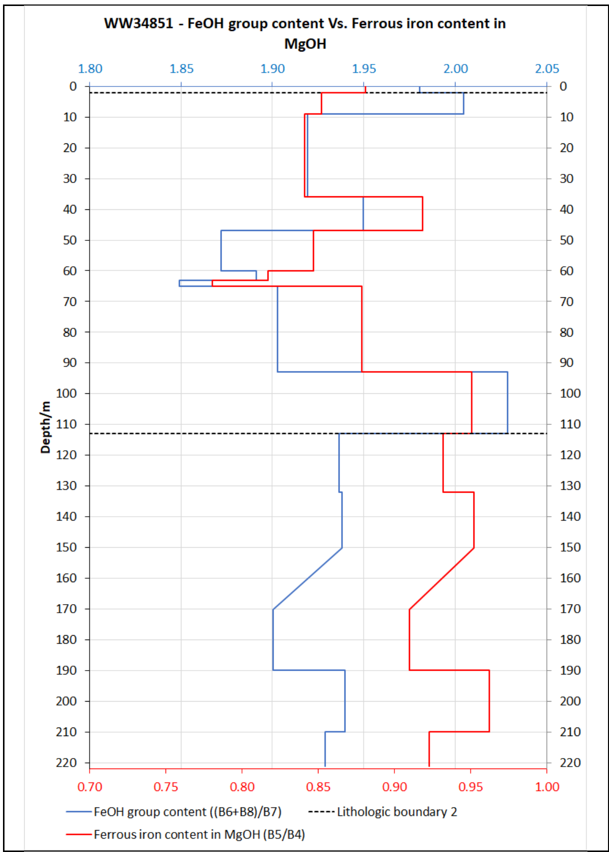

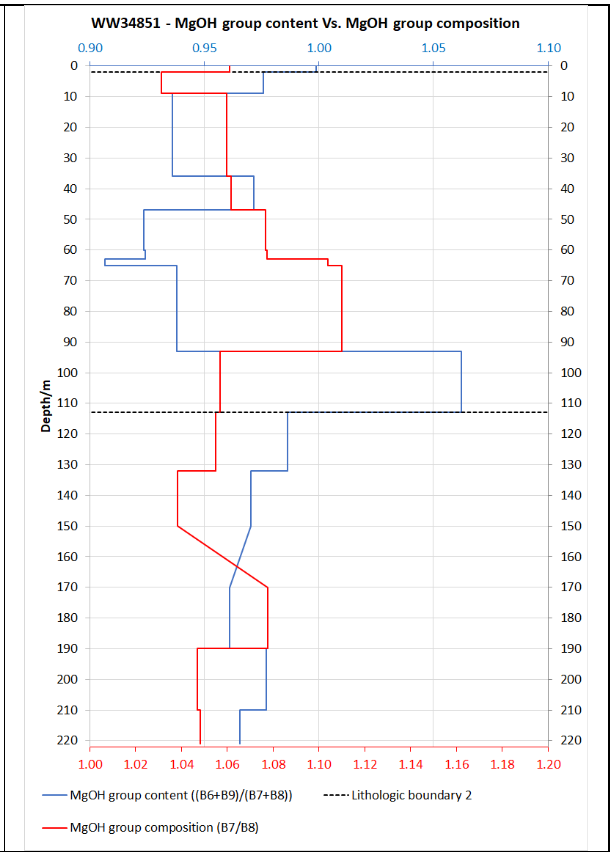

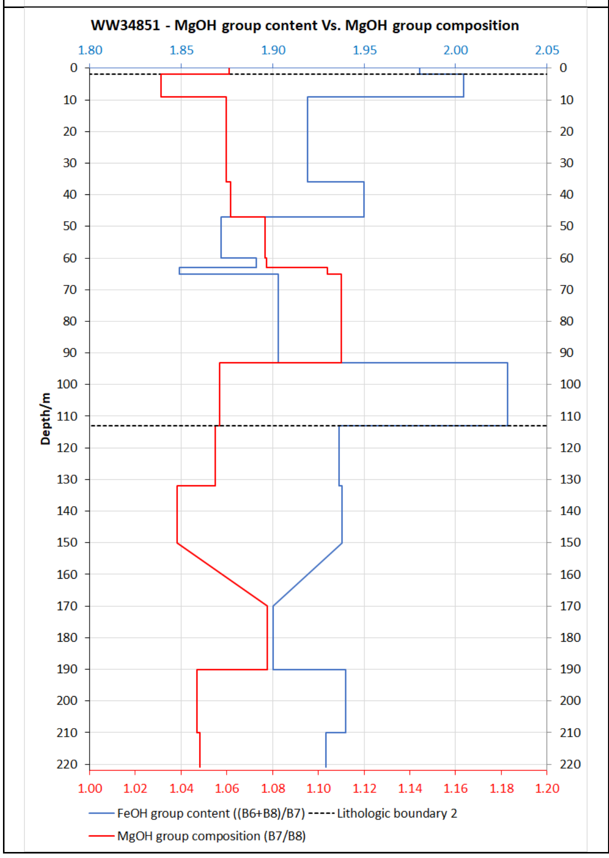

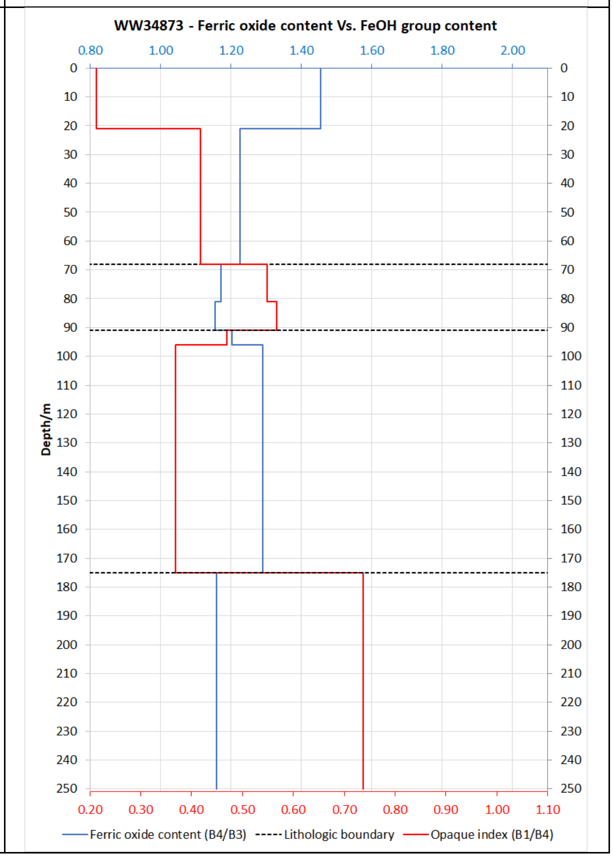

ANNEX 3 – BOREHOLE BAND RATIO COMBINATION GRAPHS

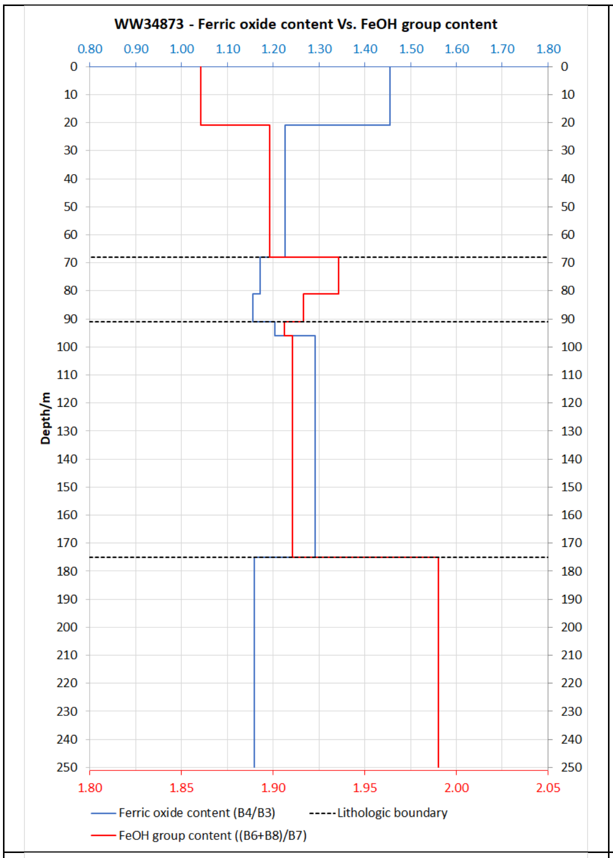

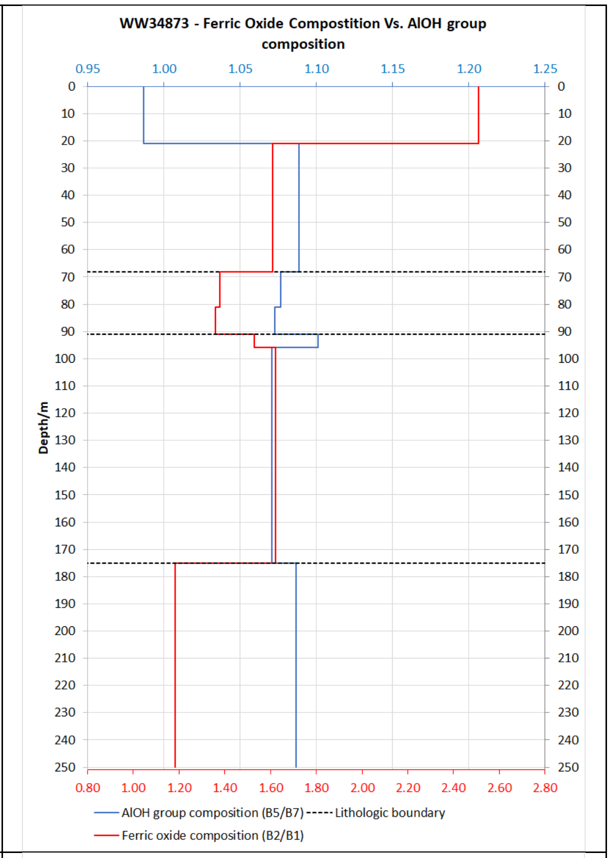

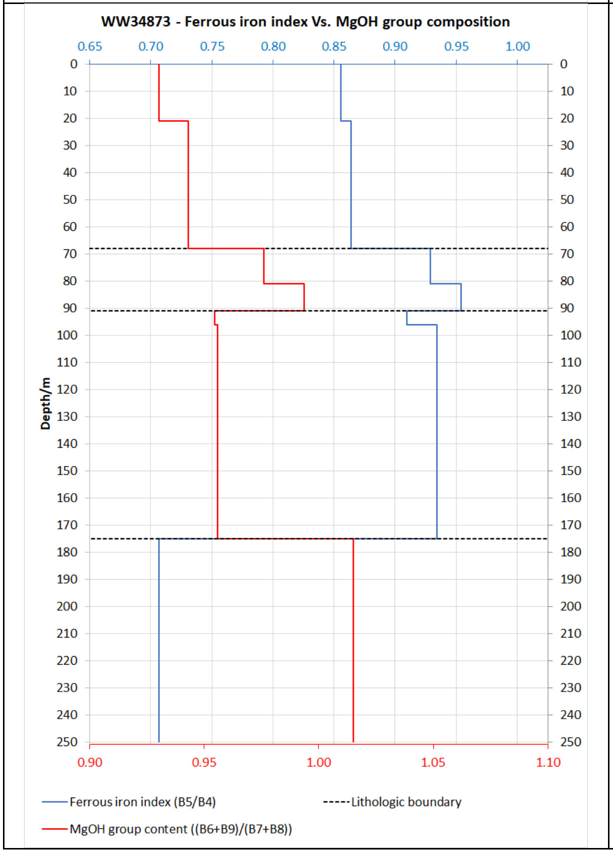

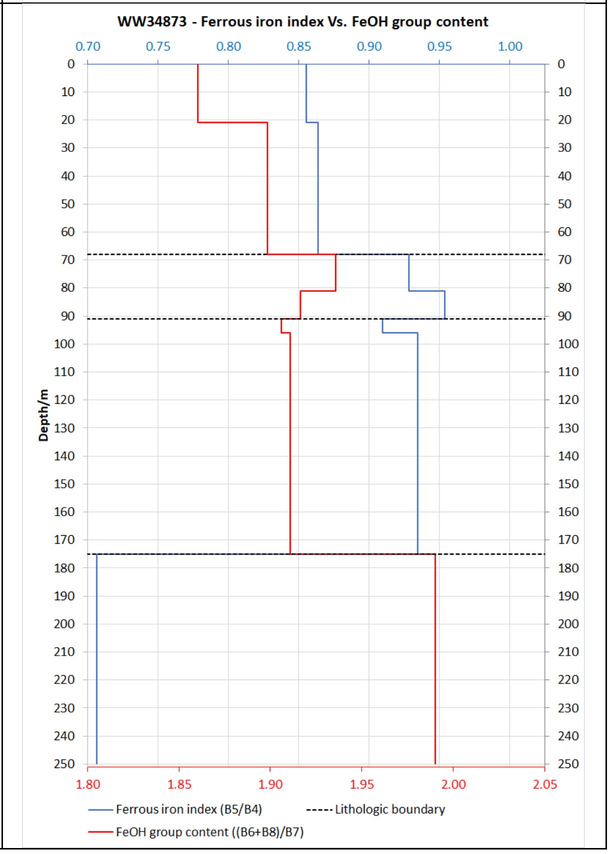

ANNEX 3 – BOREHOLE BAND RATIO COMBINATION GRAPHS

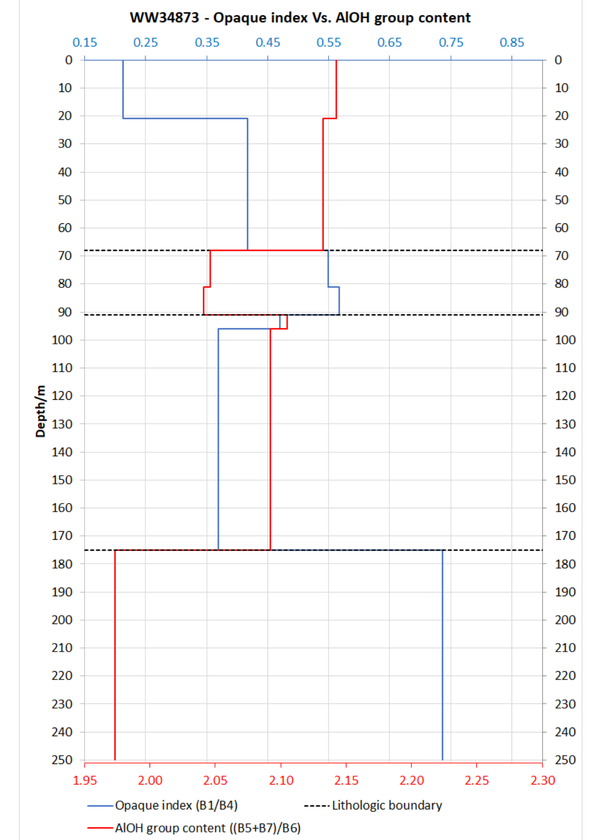

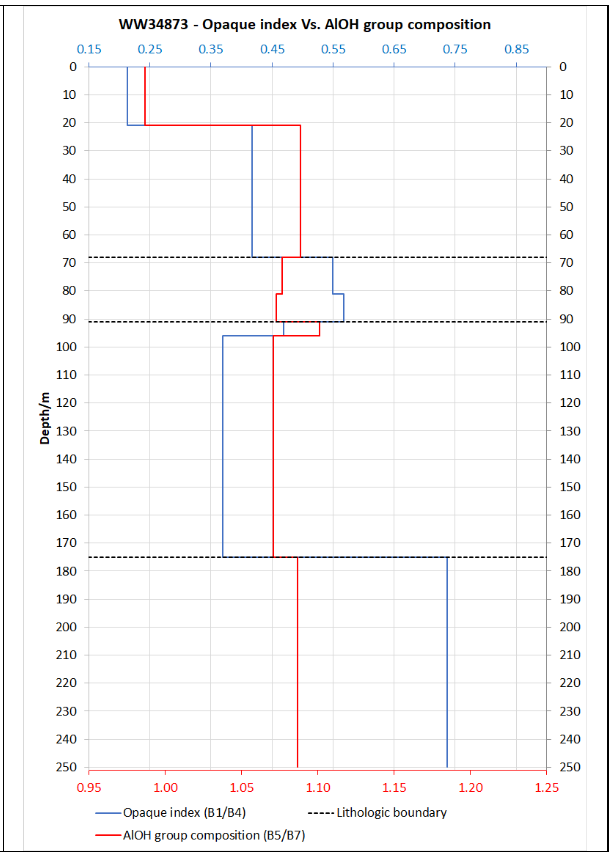

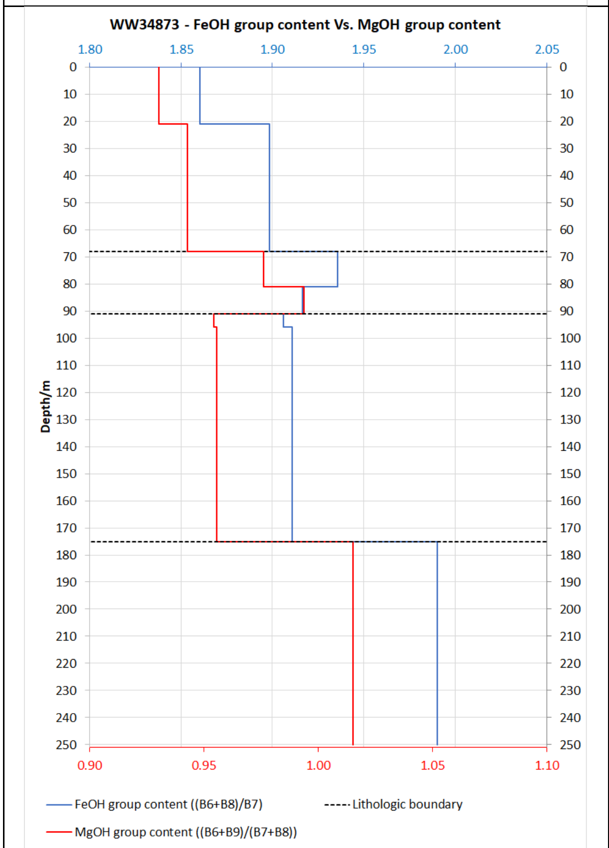

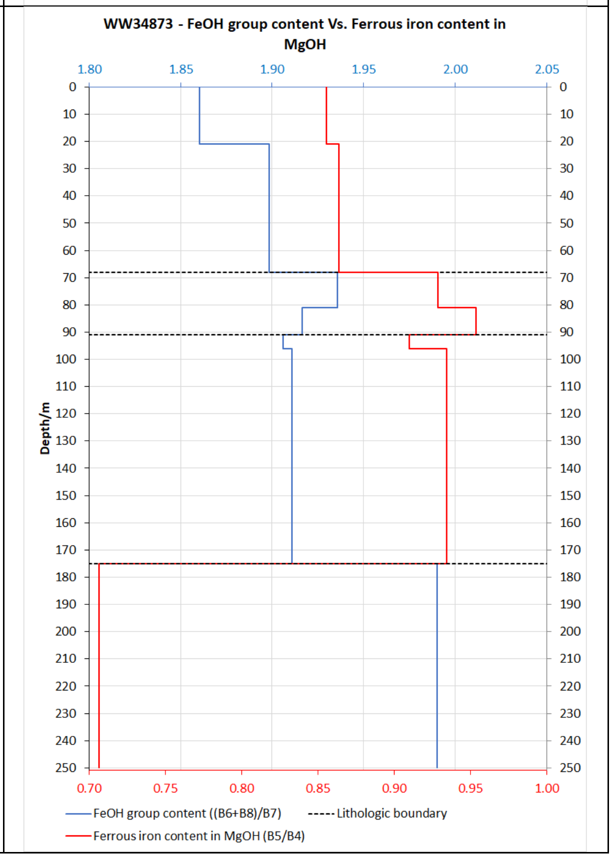

ANNEX 3 – BOREHOLE BAND RATIO COMBINATION GRAPHS

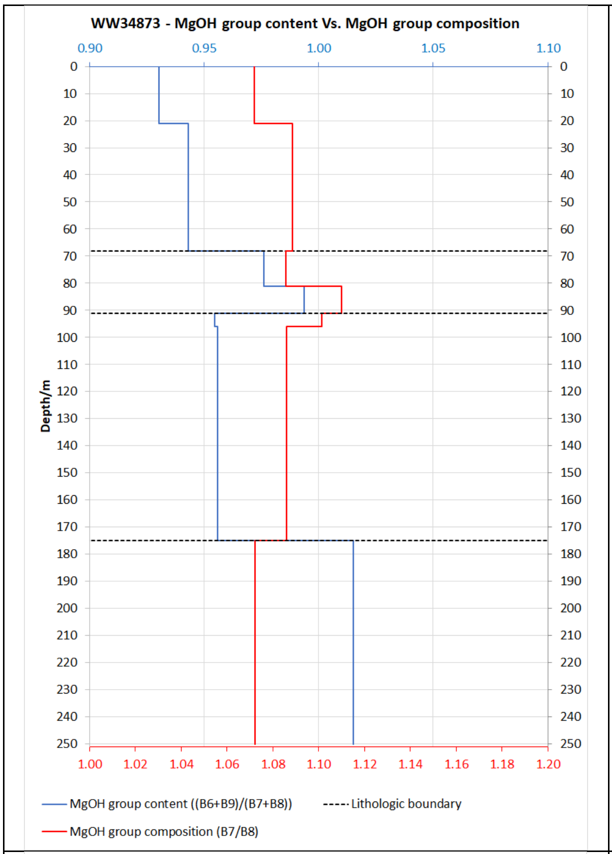

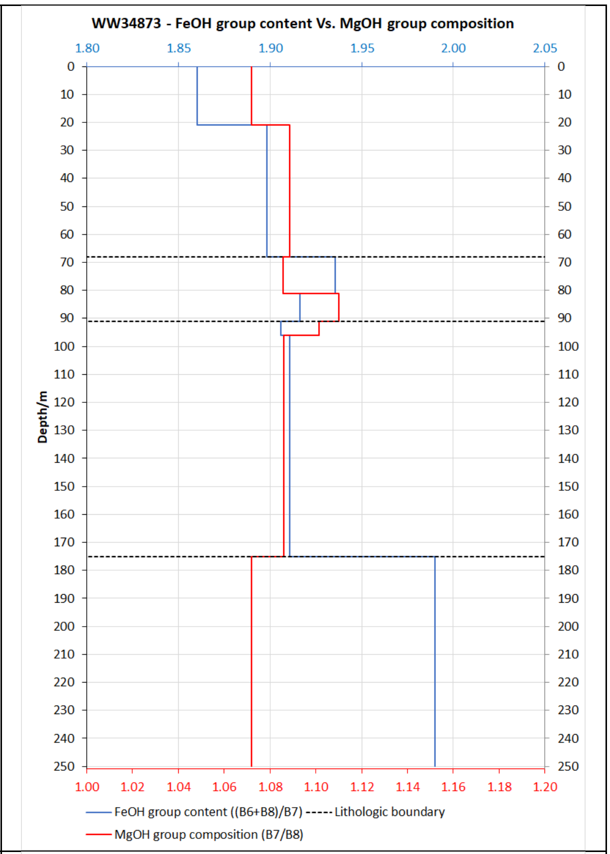

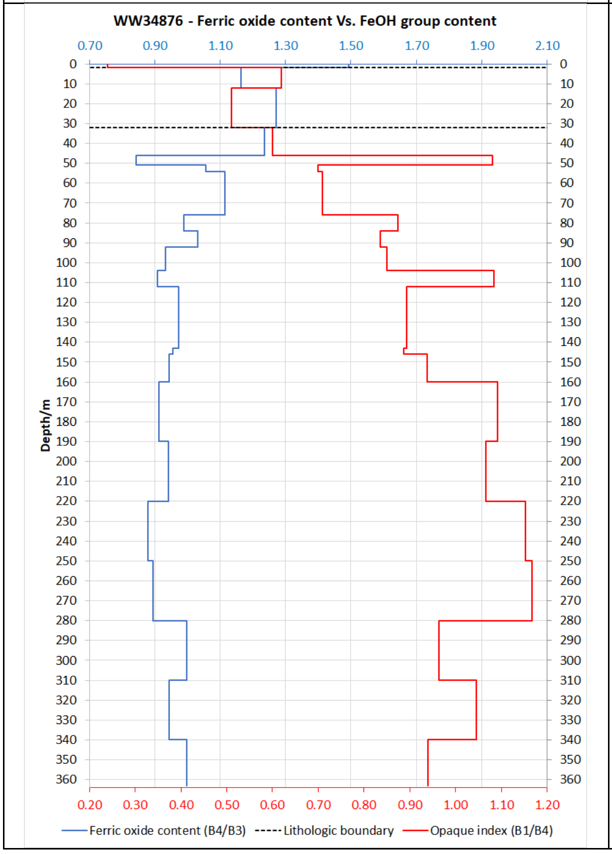

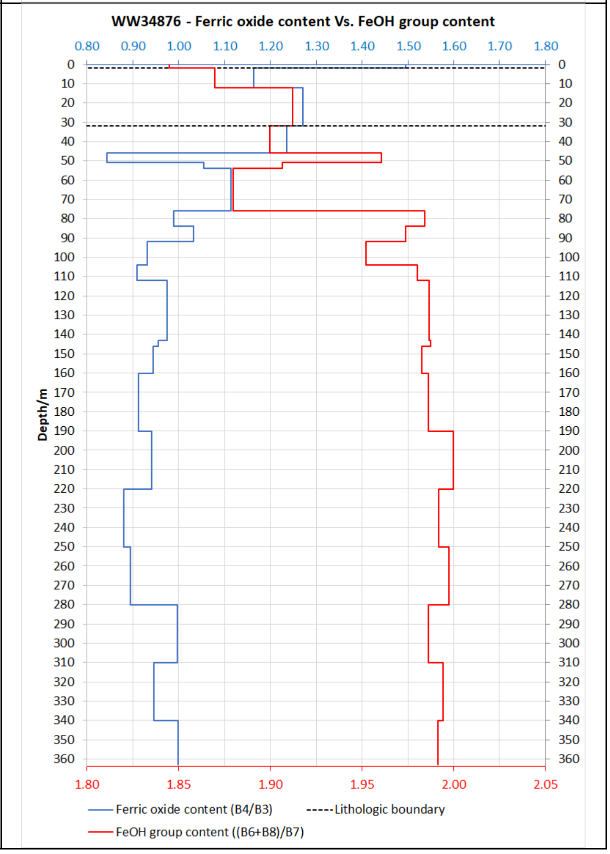

ANNEX 3 – BOREHOLE BAND RATIO COMBINATION GRAPHS

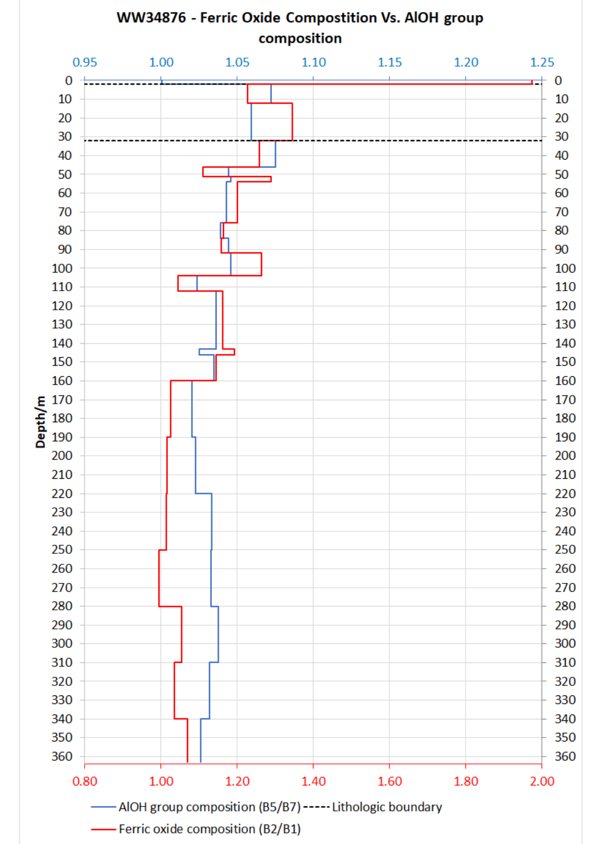

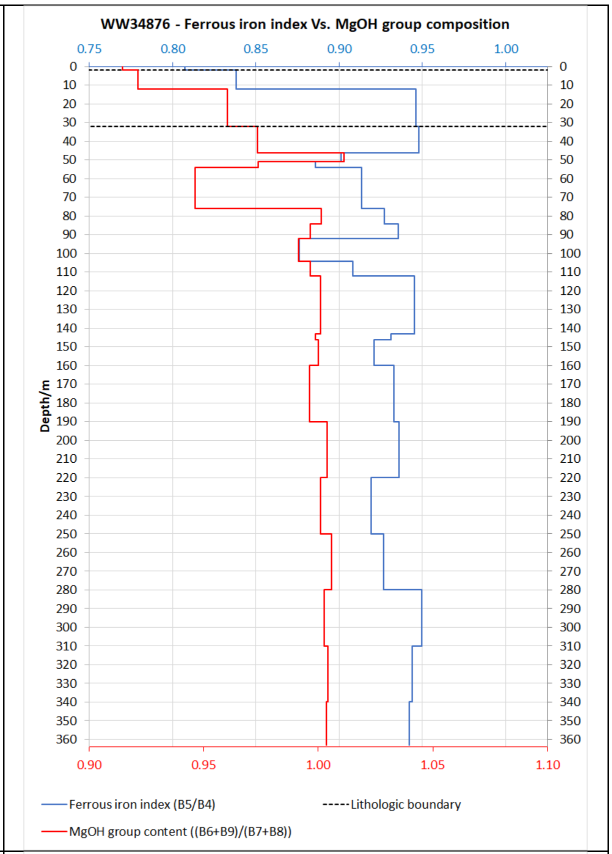

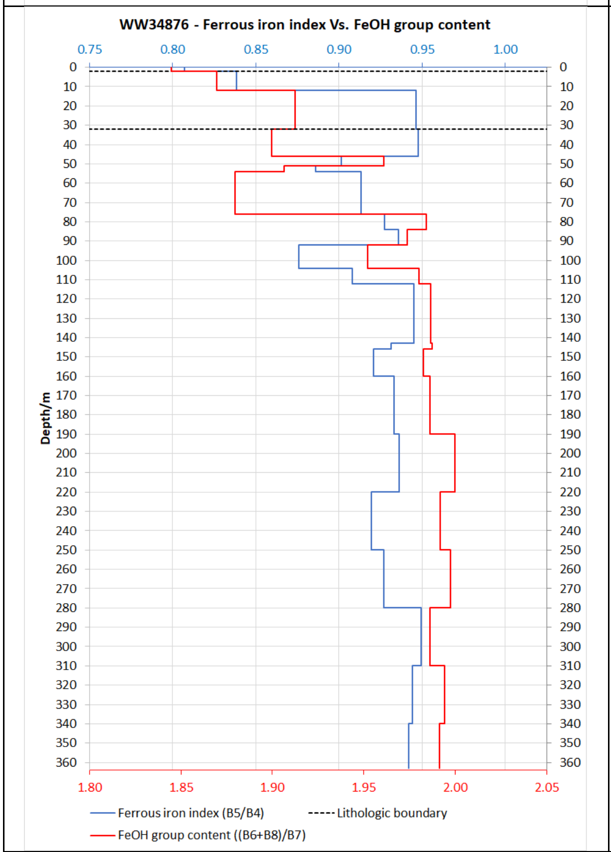

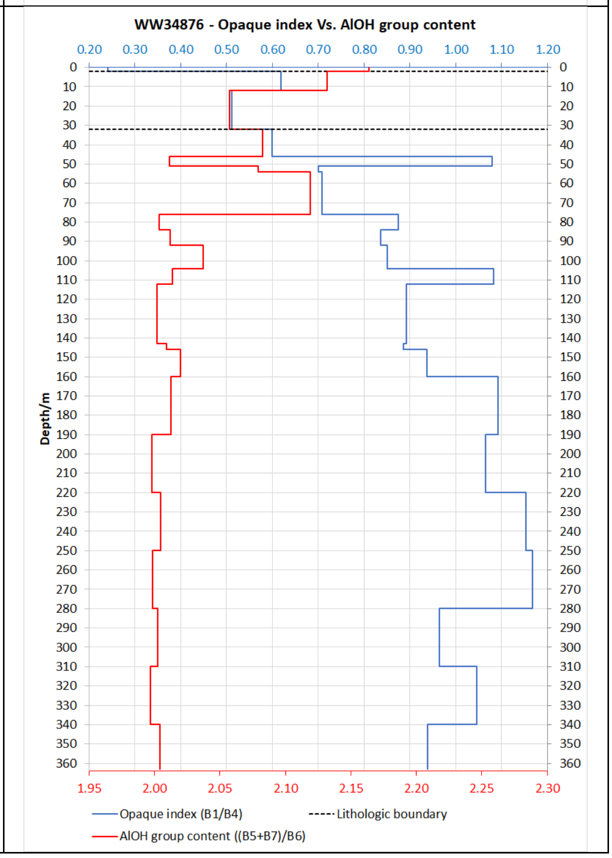

ANNEX 3 – BOREHOLE BAND RATIO COMBINATION GRAPHS

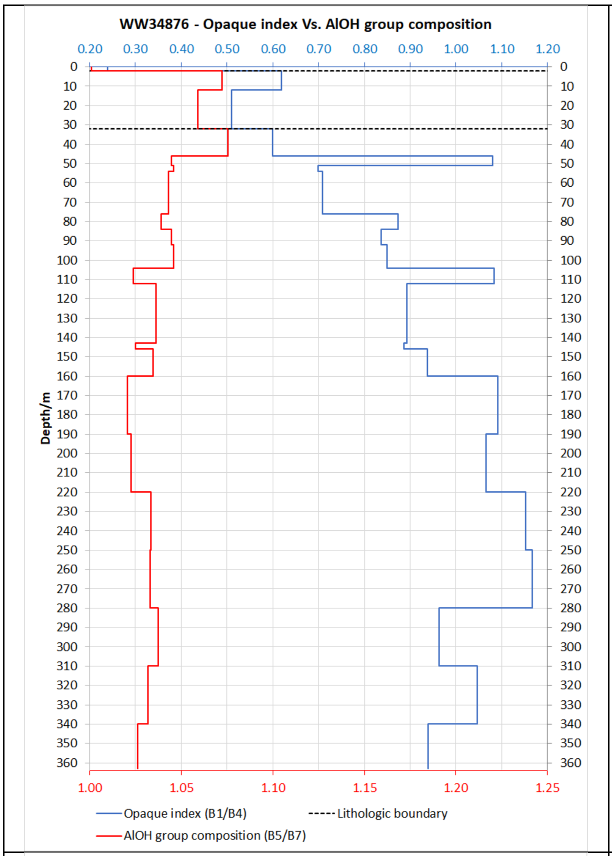

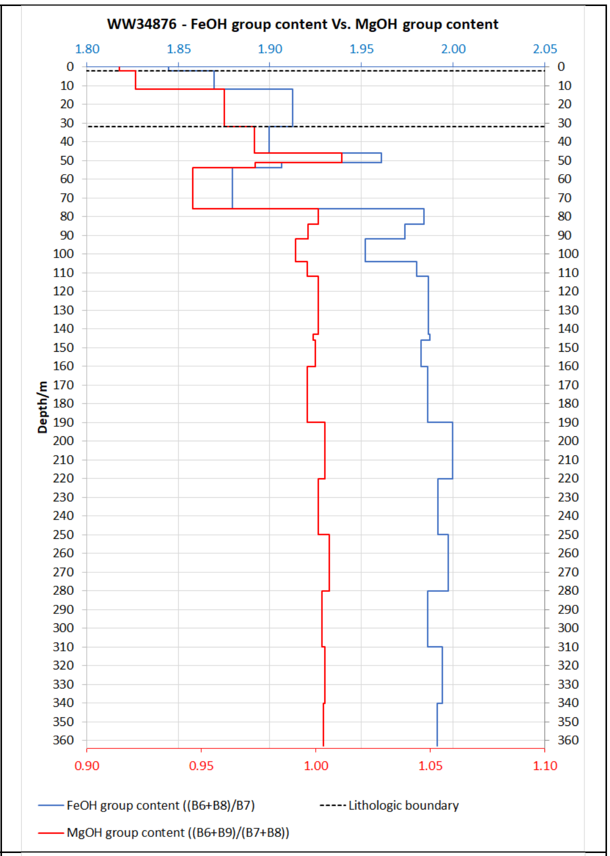

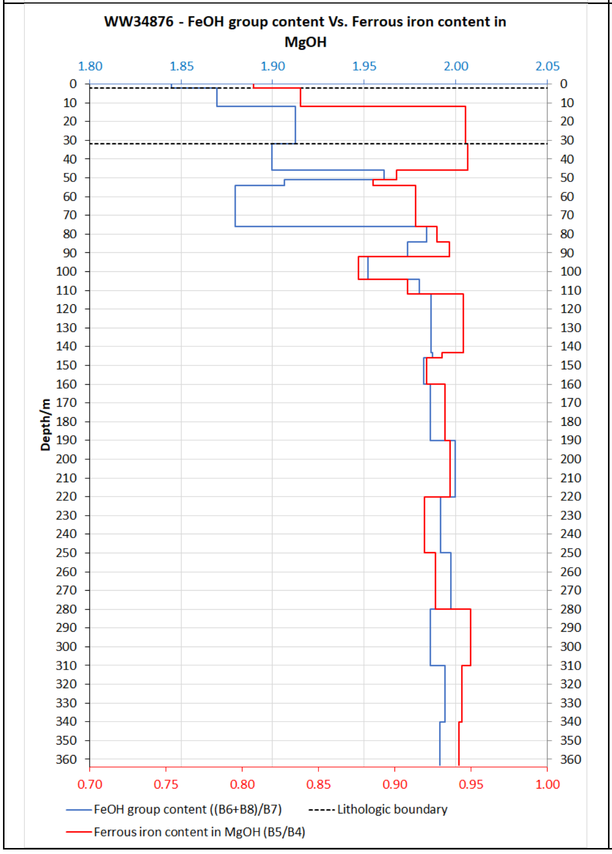

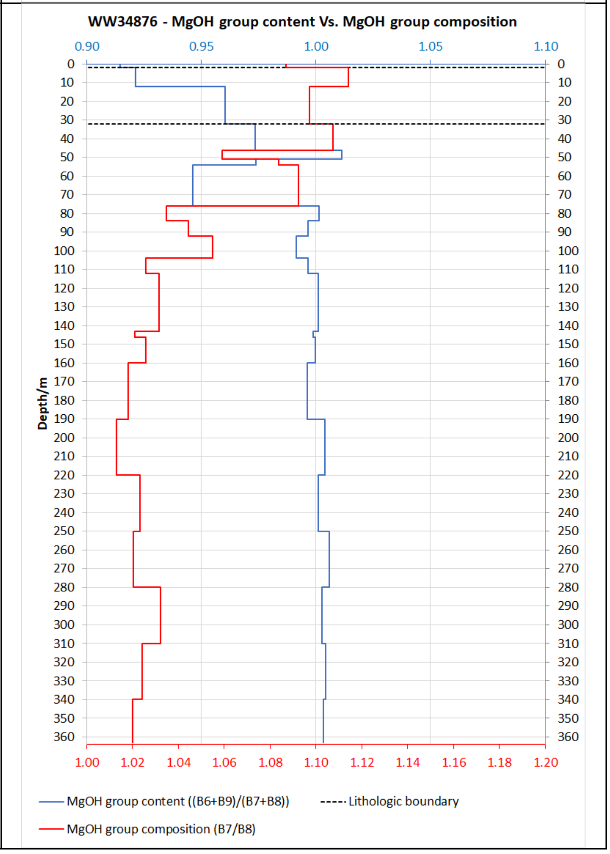

ANNEX 3 – BOREHOLE BAND RATIO COMBINATION GRAPHS

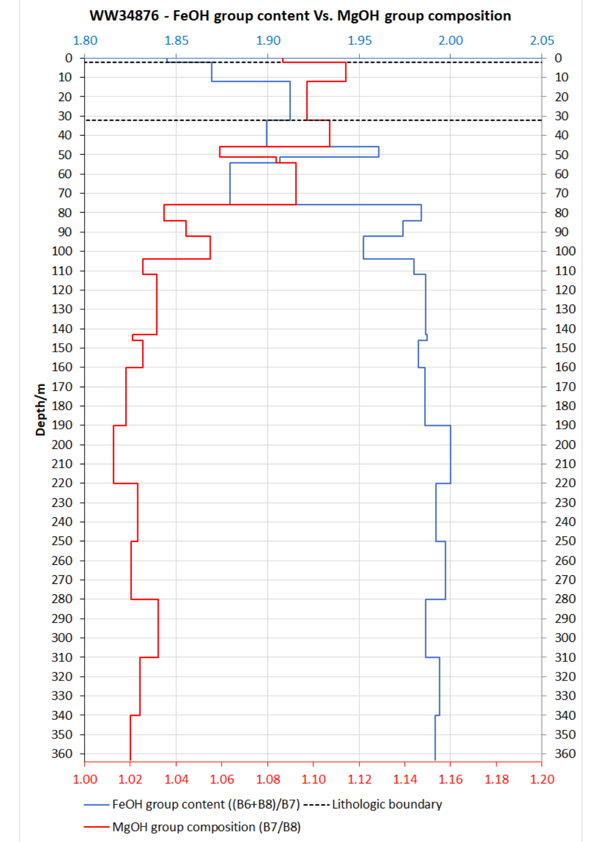

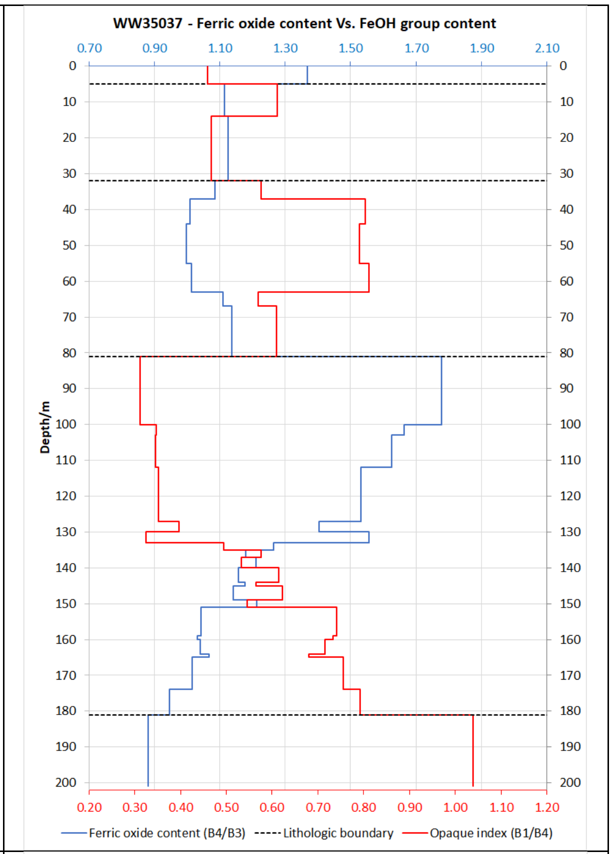

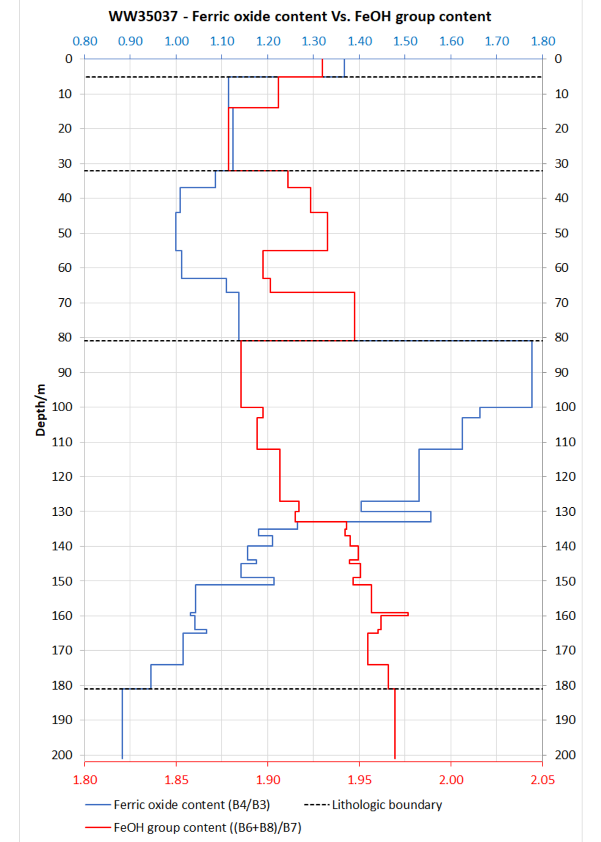

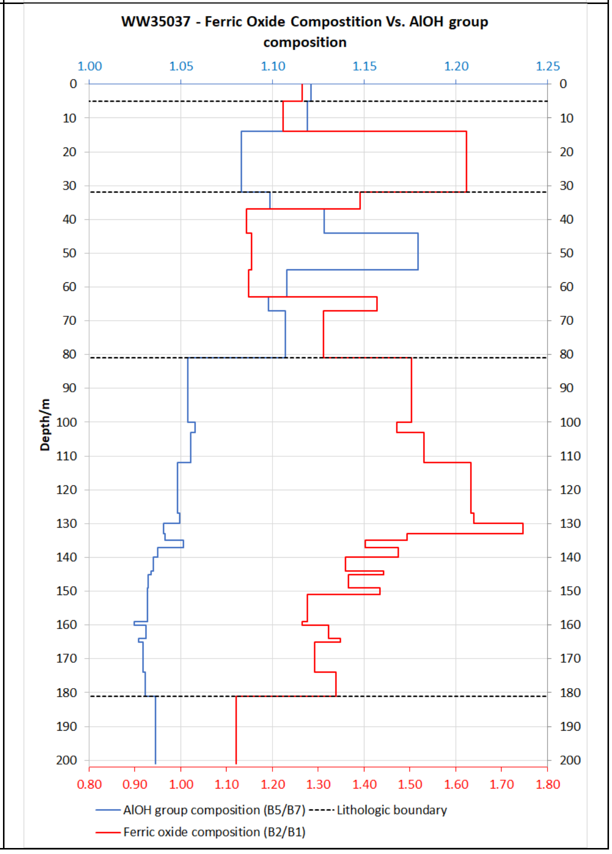

ANNEX 3 – BOREHOLE BAND RATIO COMBINATION GRAPHS

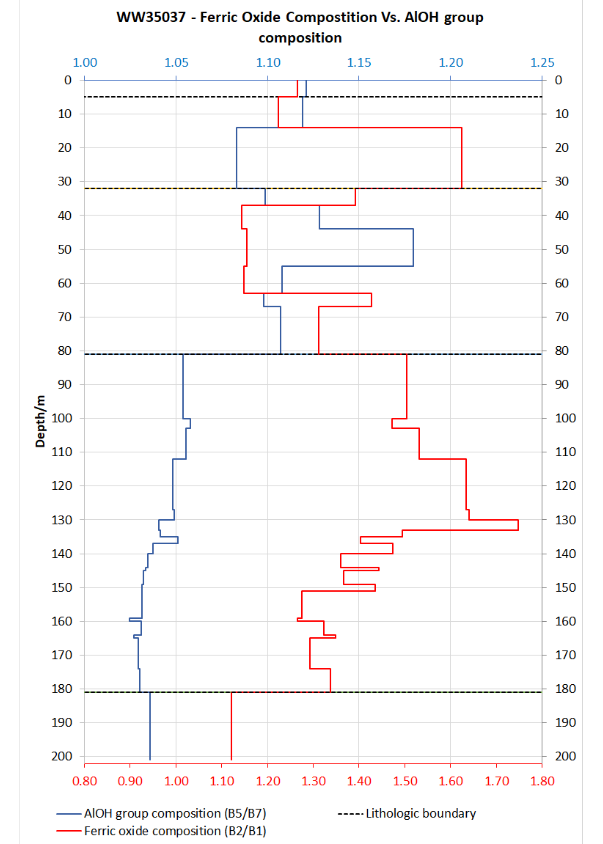

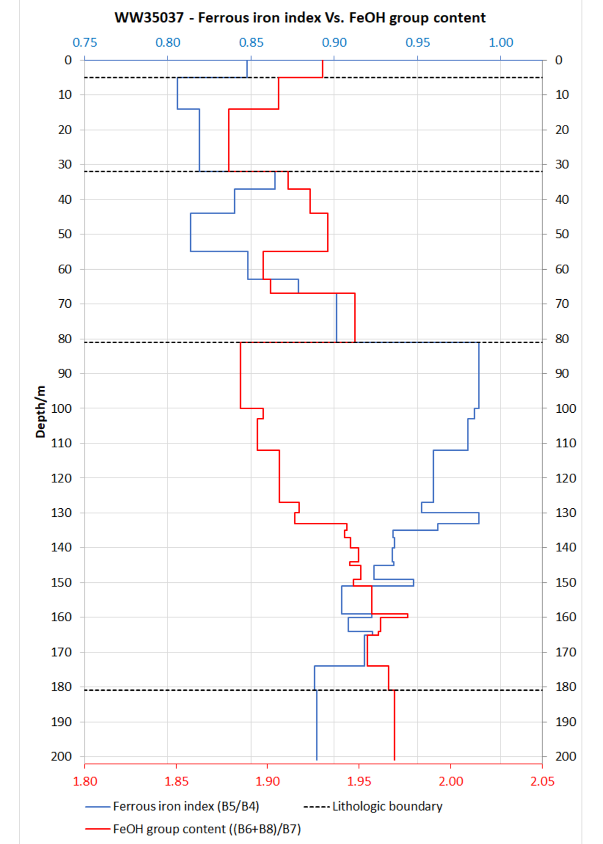

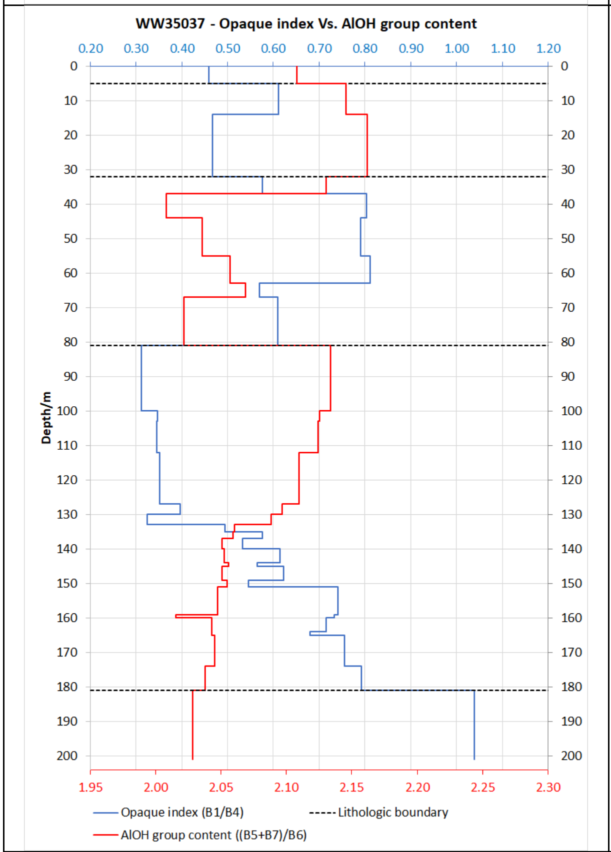

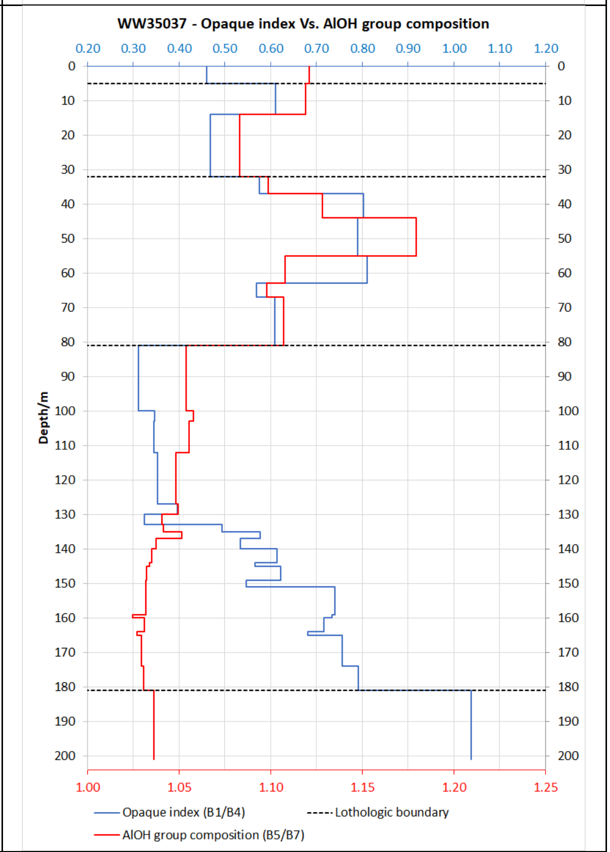

ANNEX 3 – BOREHOLE BAND RATIO COMBINATION GRAPHS

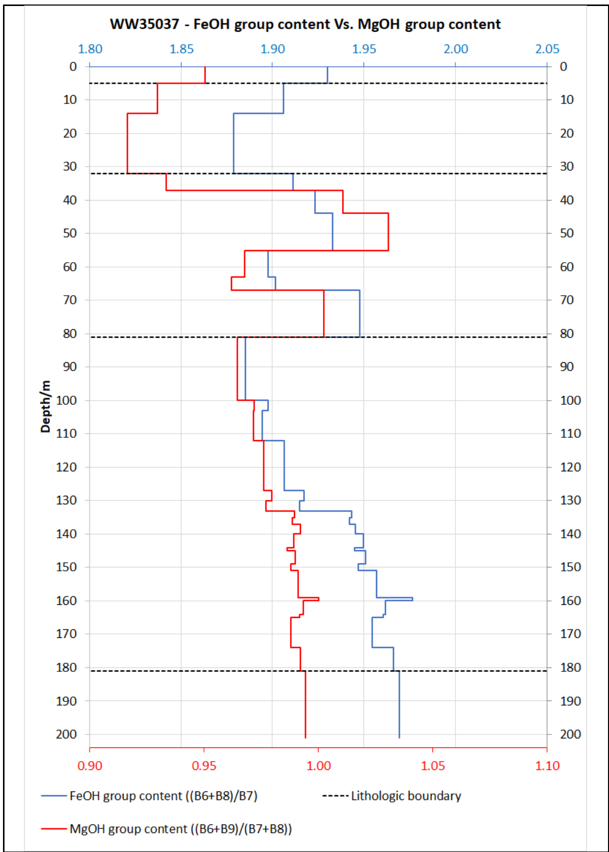

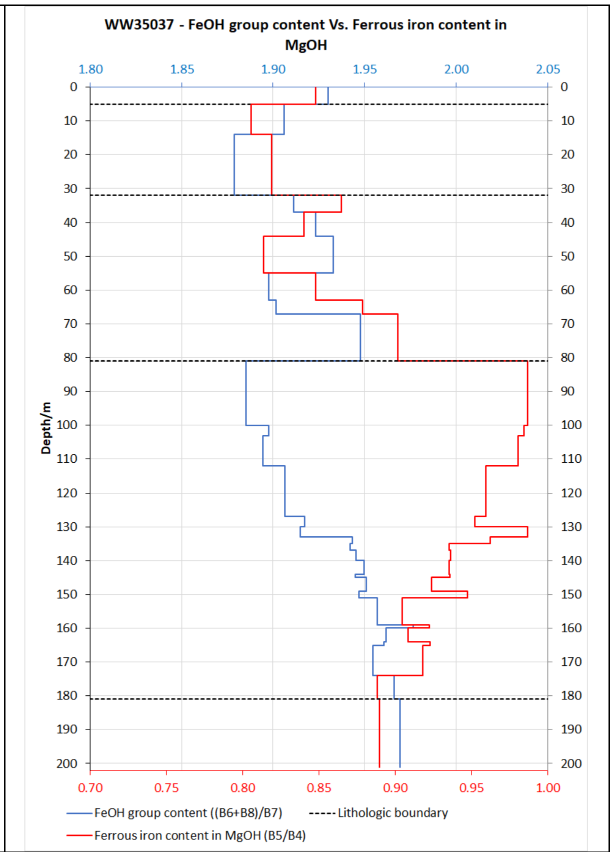

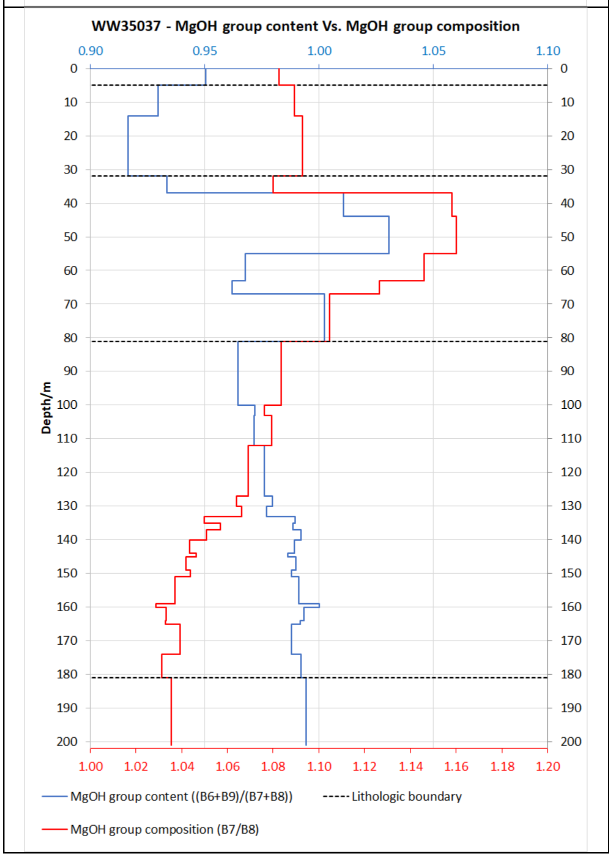

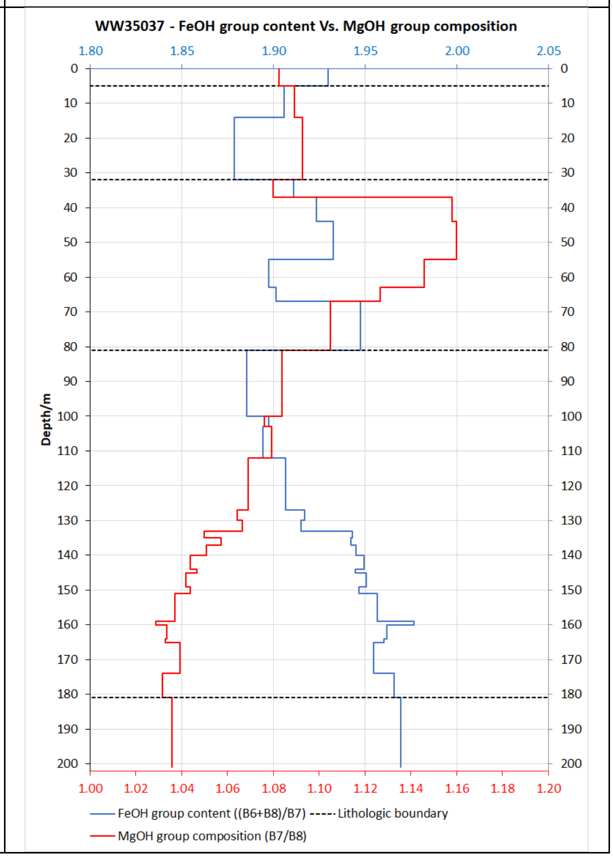

ANNEX 3 – BOREHOLE BAND RATIO COMBINATION GRAPHS

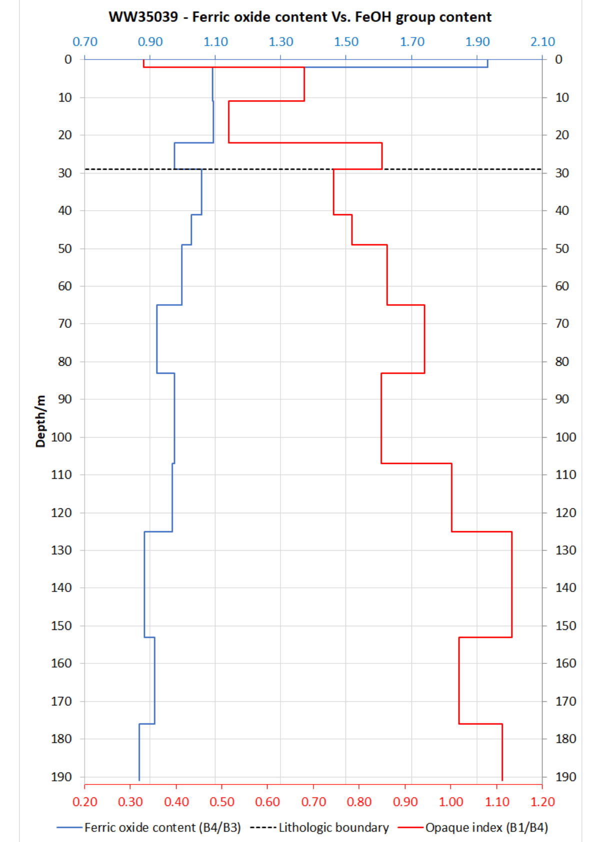

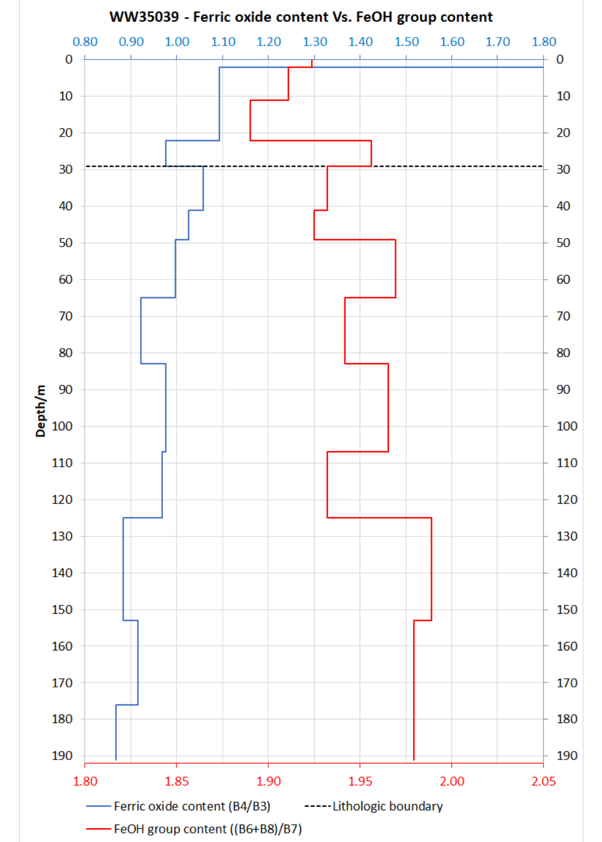

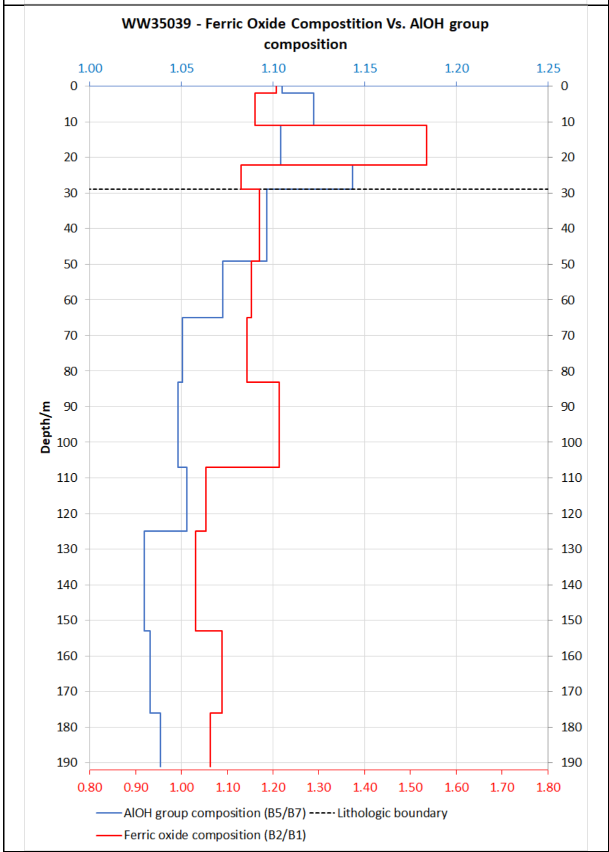

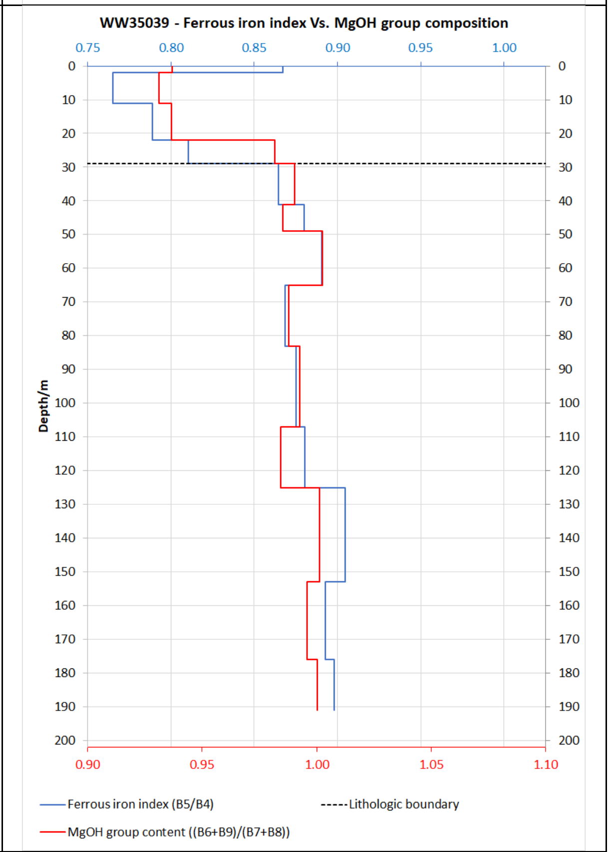

ANNEX 3 – BOREHOLE BAND RATIO COMBINATION GRAPHS

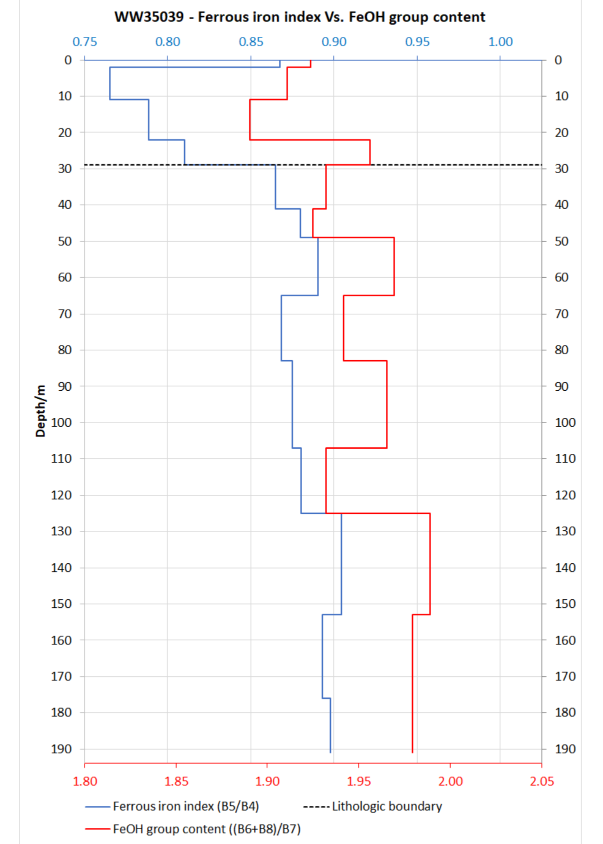

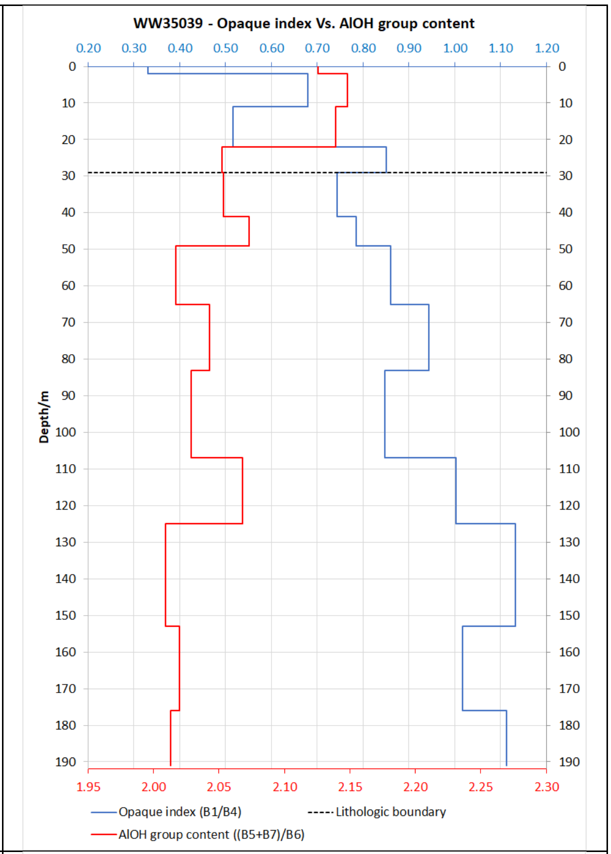

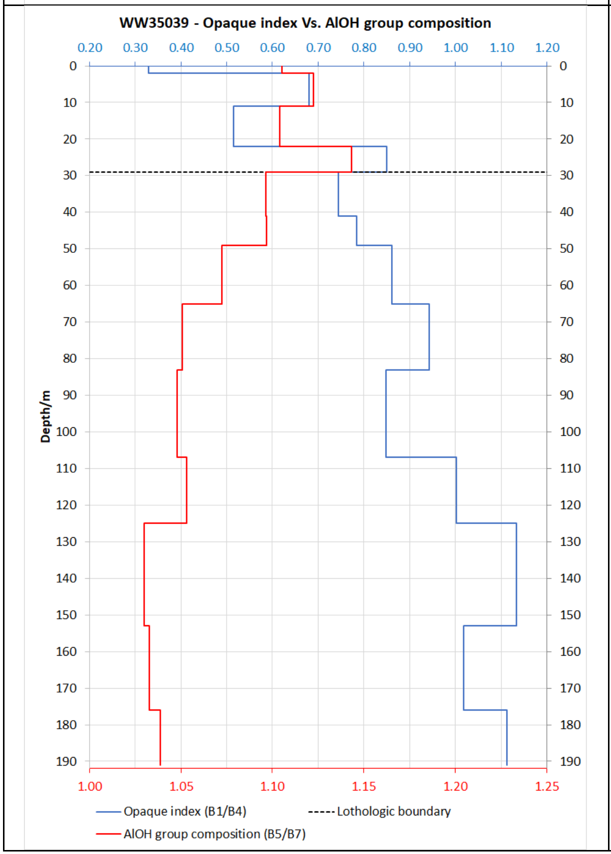

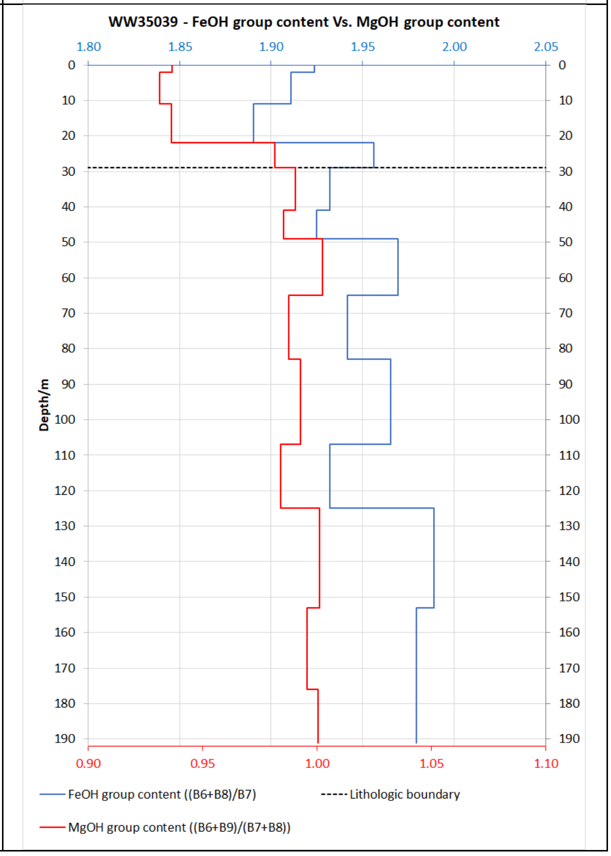

ANNEX 3 – BOREHOLE BAND RATIO COMBINATION GRAPHS

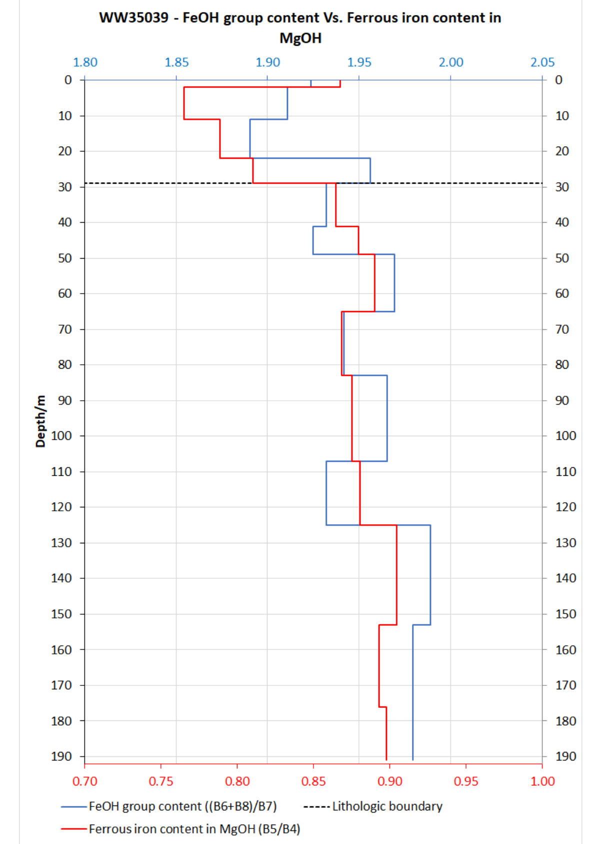

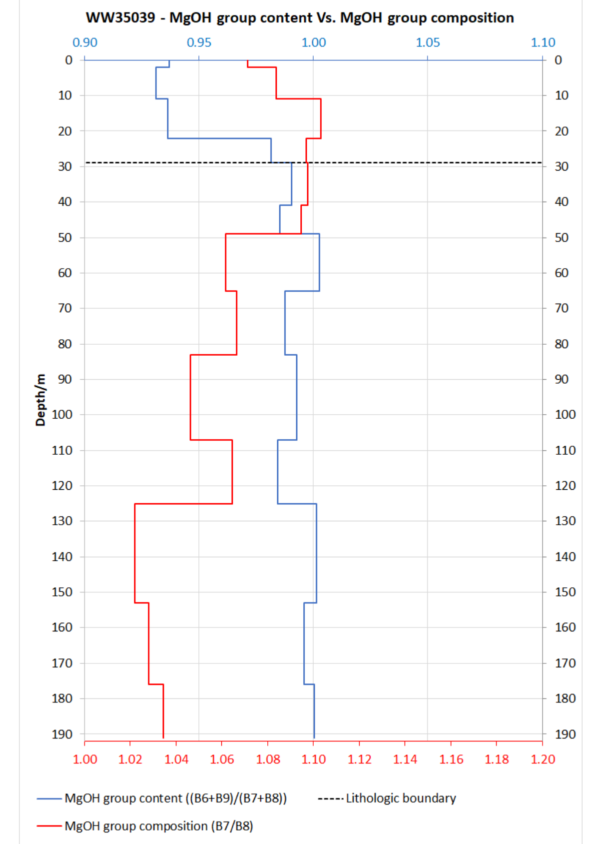

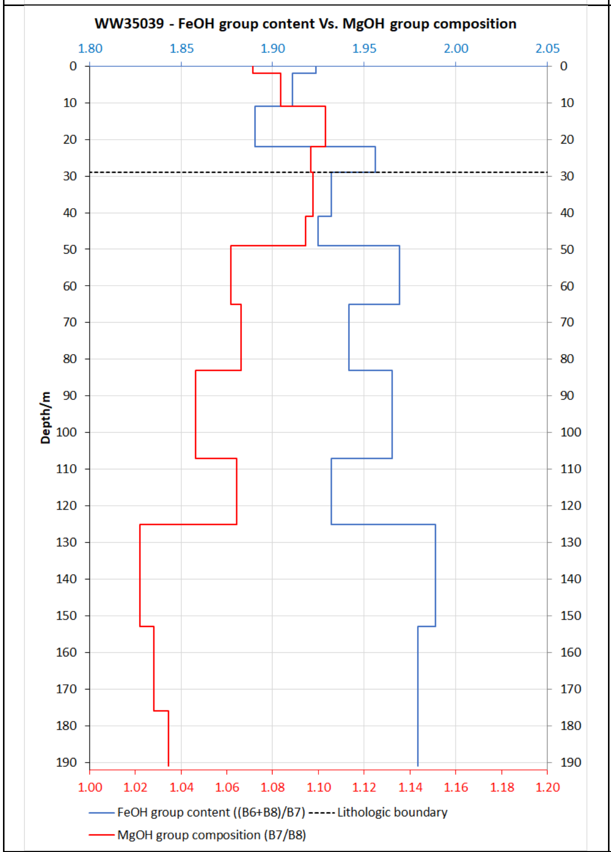

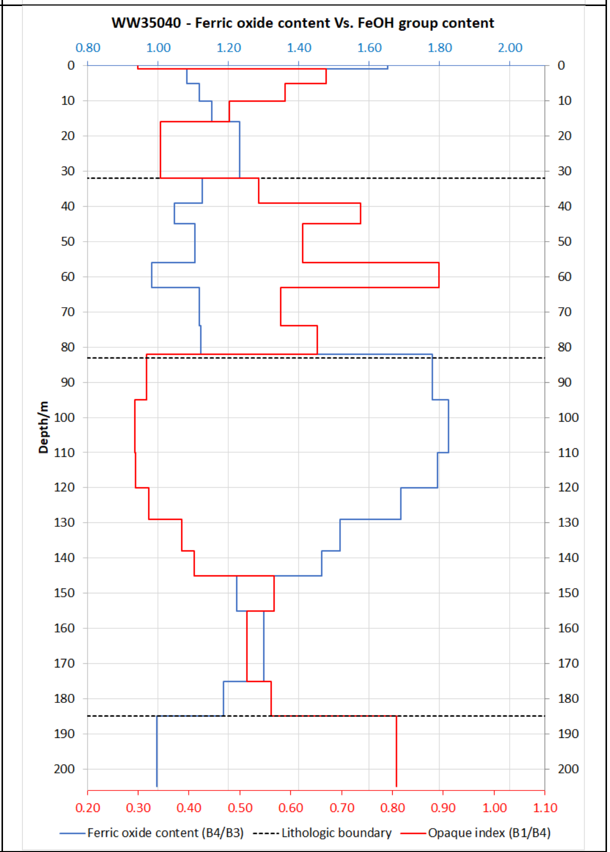

ANNEX 3 – BOREHOLE BAND RATIO COMBINATION GRAPHS

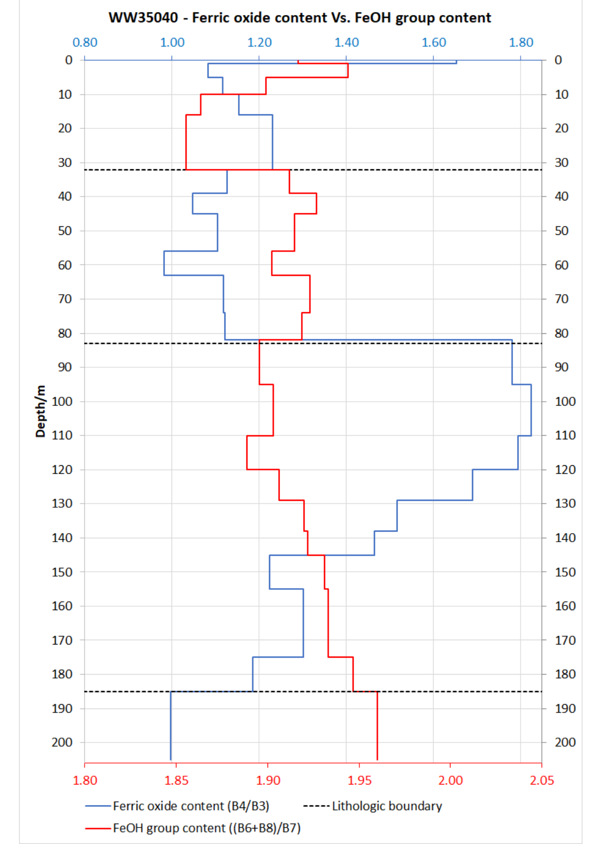

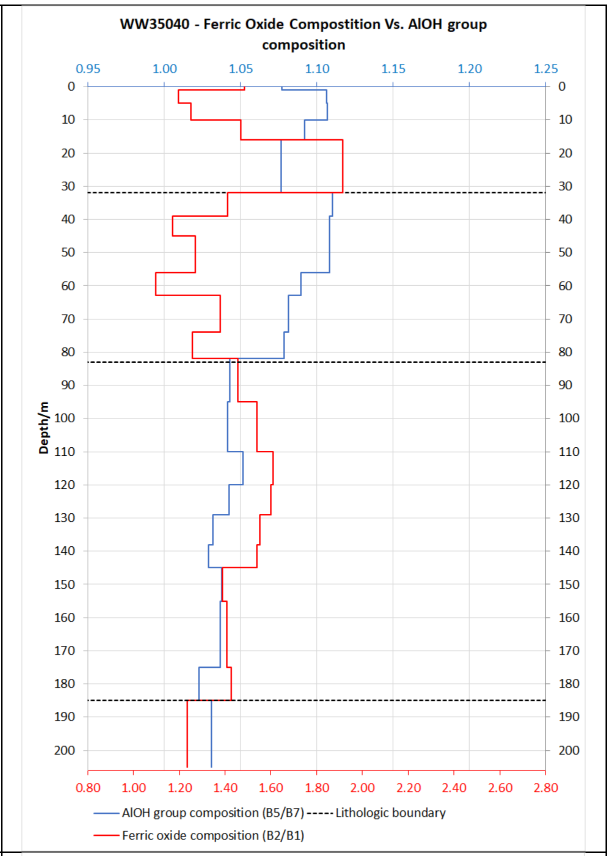

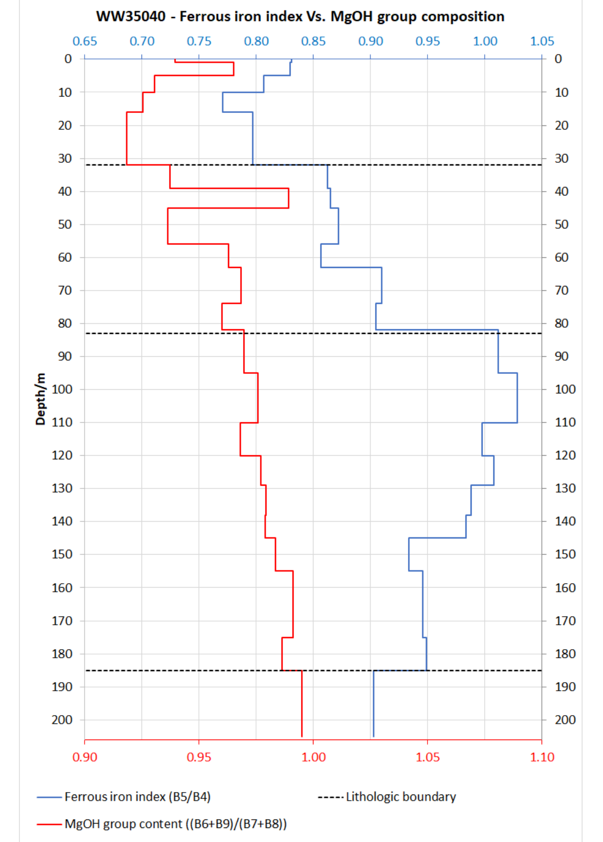

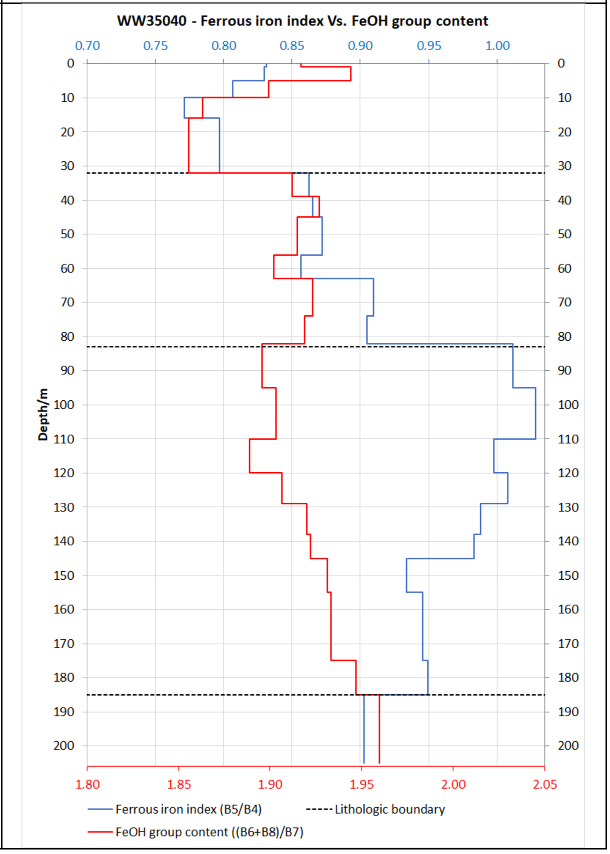

ANNEX 3 – BOREHOLE BAND RATIO COMBINATION GRAPHS

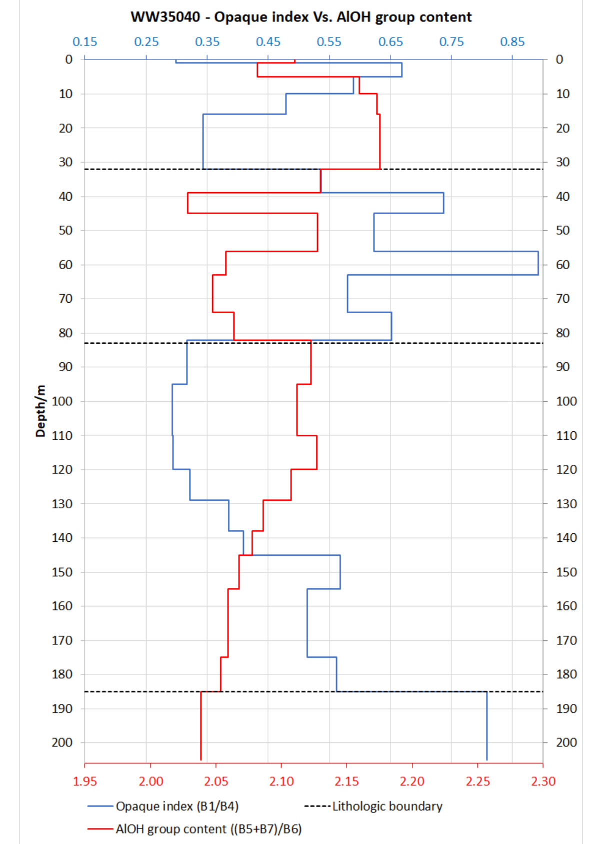

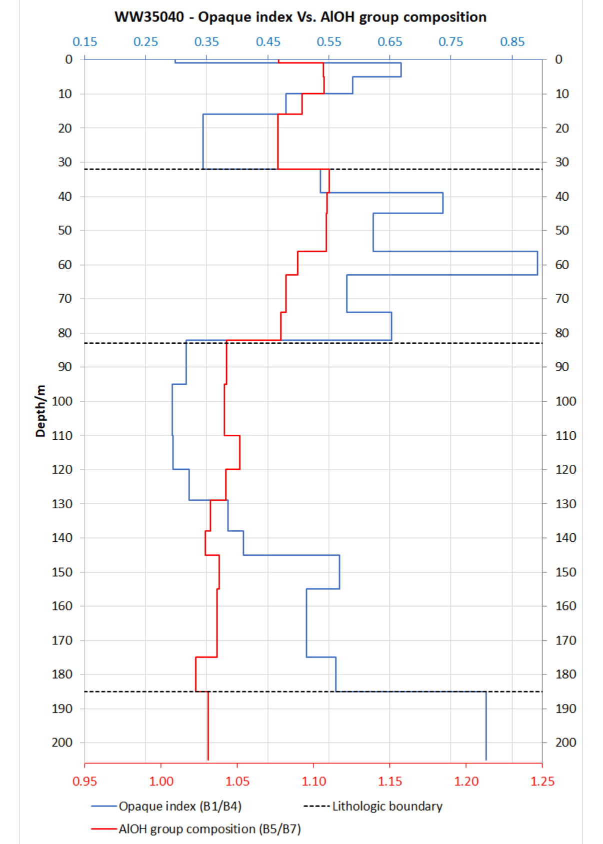

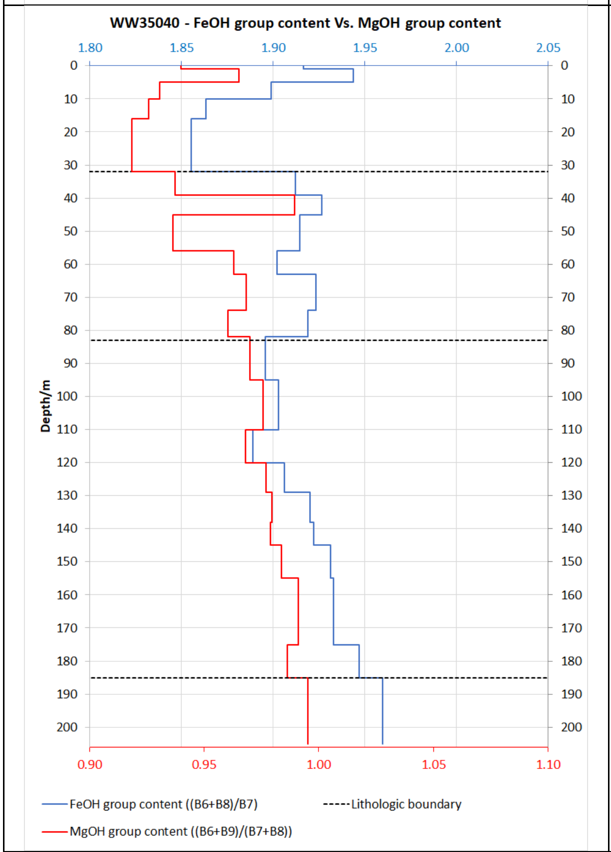

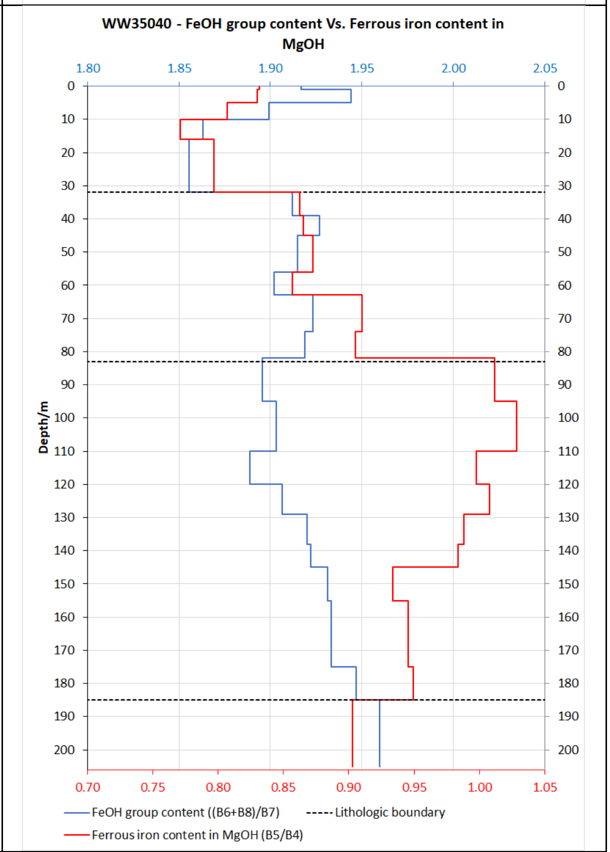

ANNEX 3 – BOREHOLE BAND RATIO COMBINATION GRAPHS

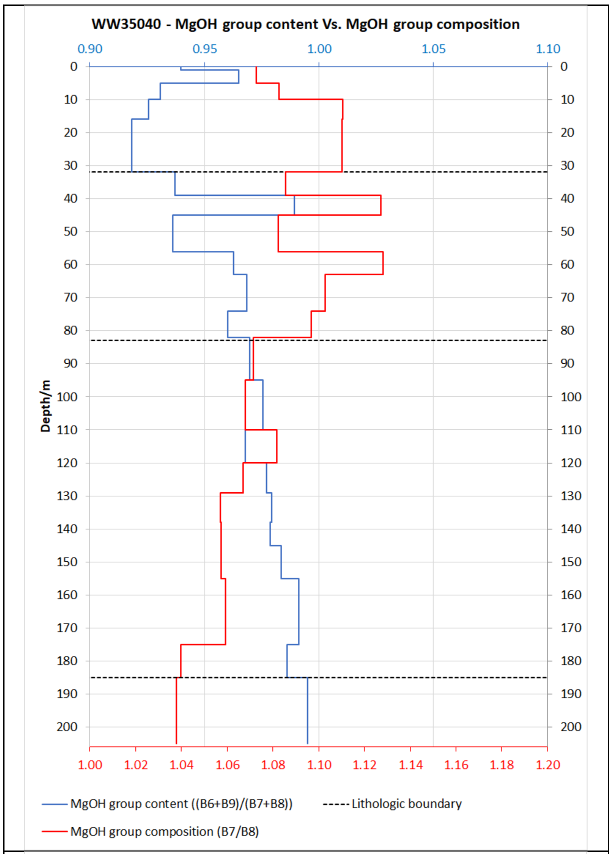

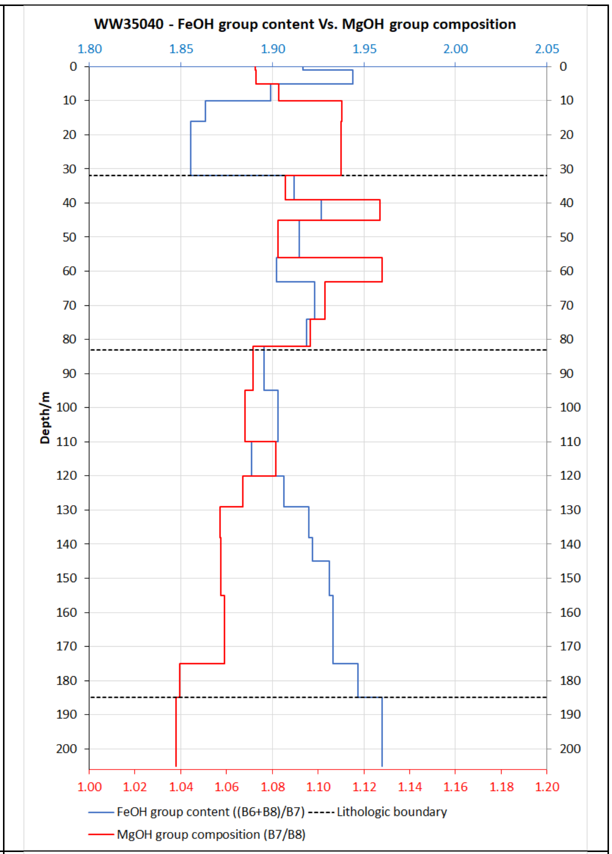

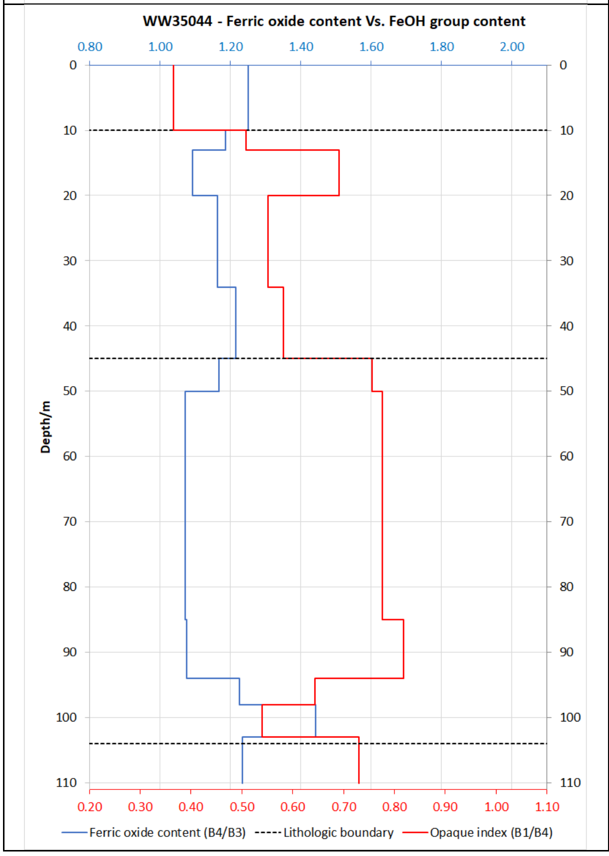

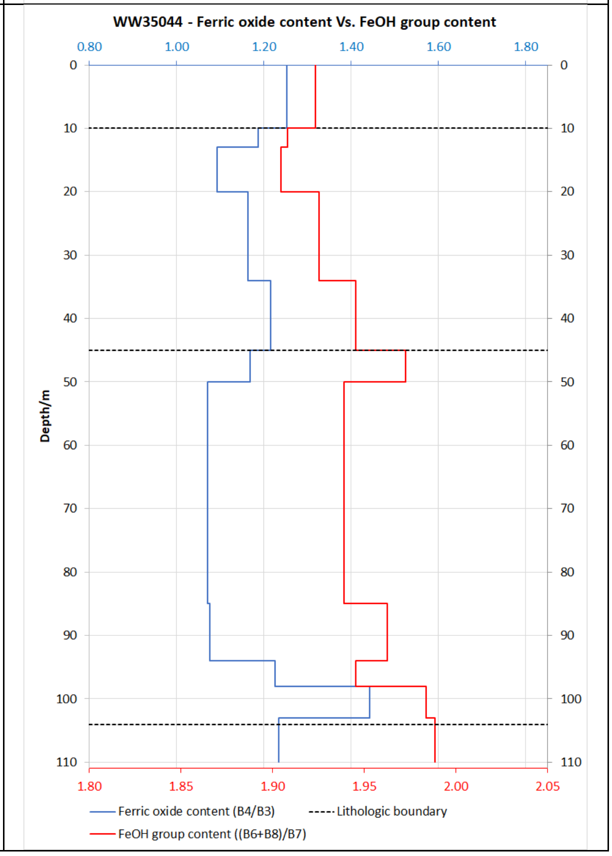

ANNEX 3 – BOREHOLE BAND RATIO COMBINATION GRAPHS

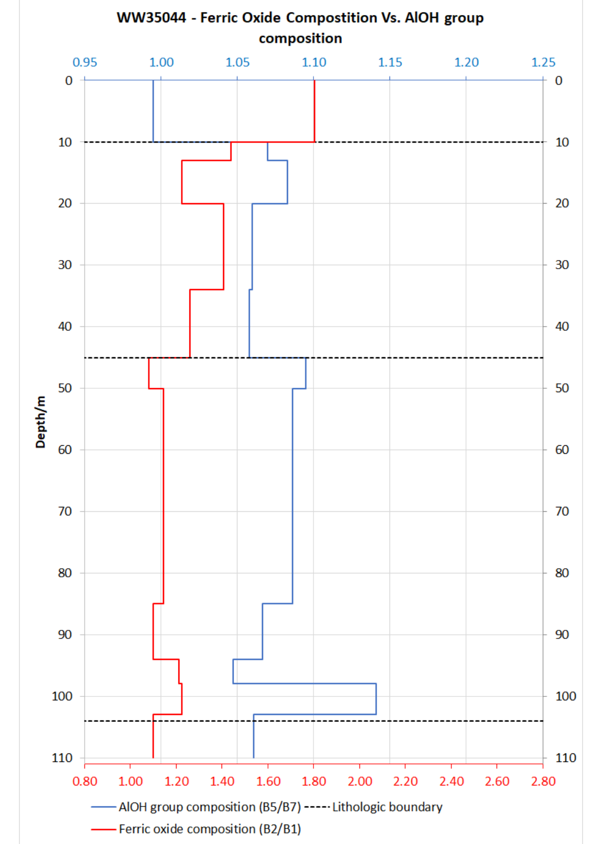

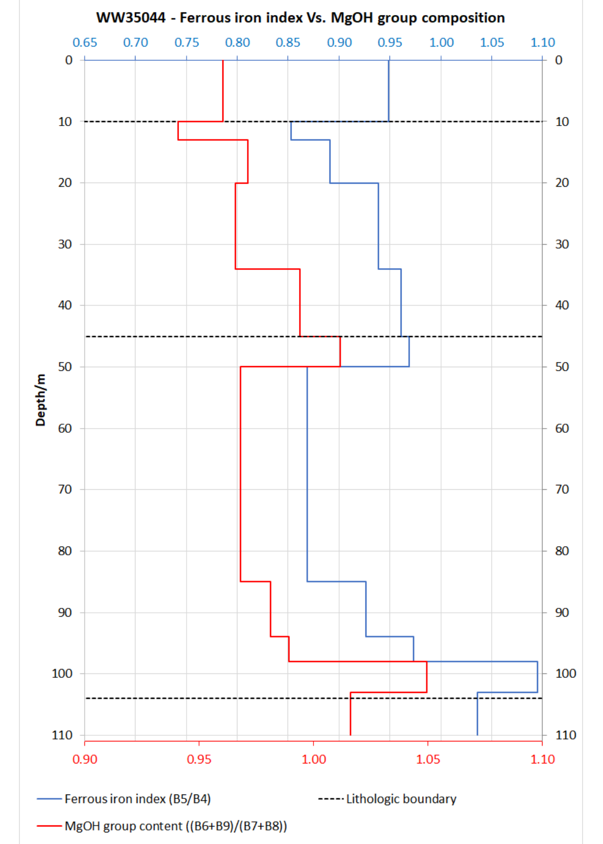

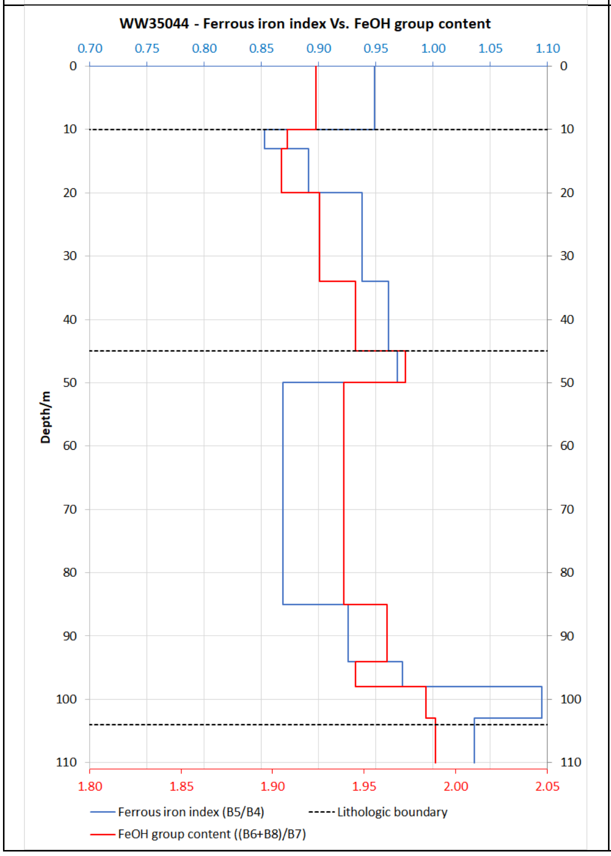

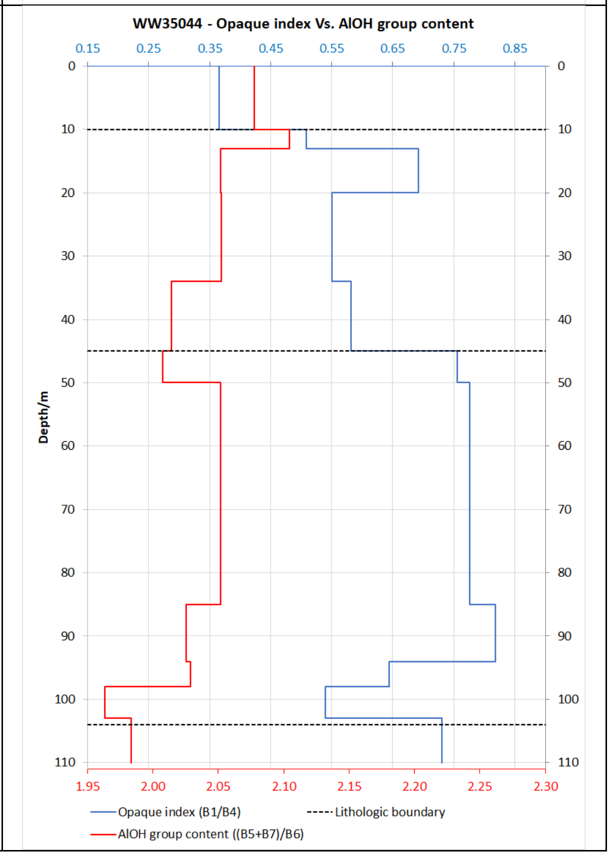

ANNEX 3 – BOREHOLE BAND RATIO COMBINATION GRAPHS

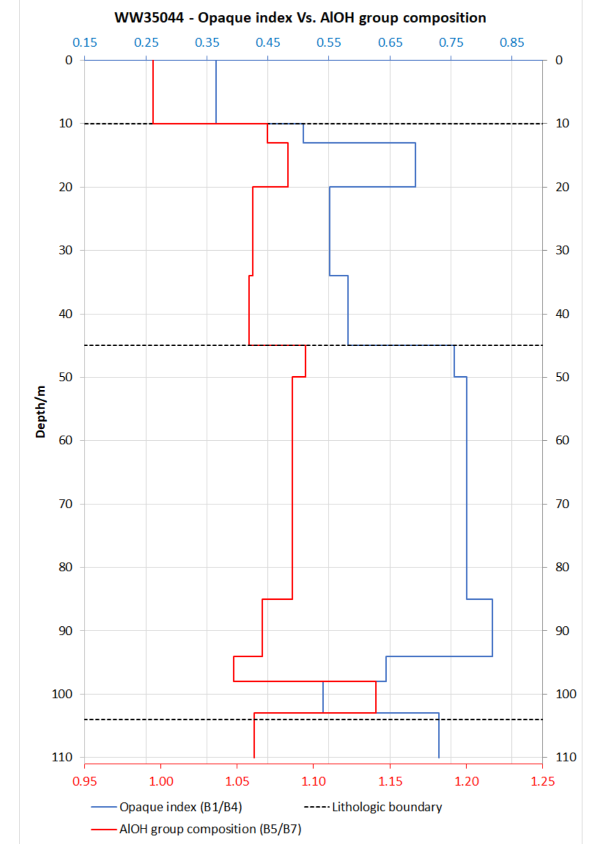

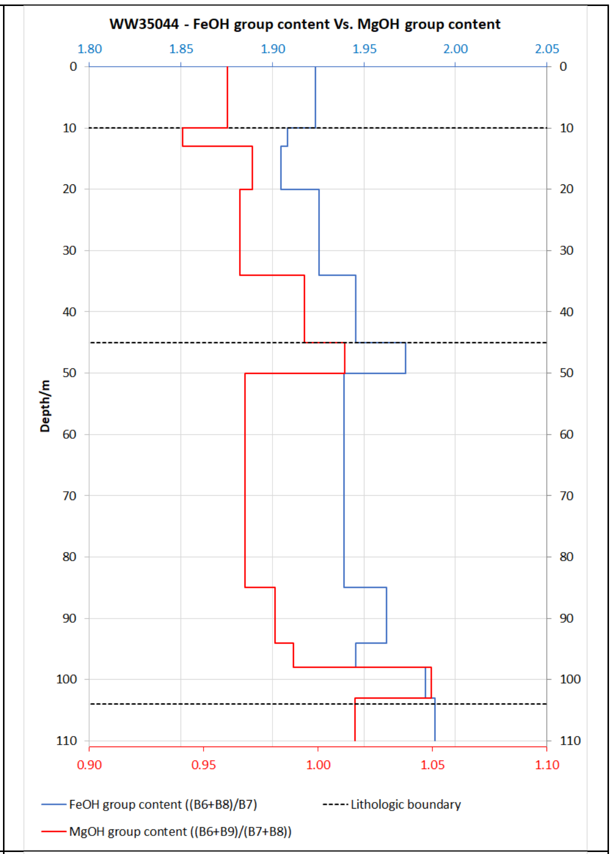

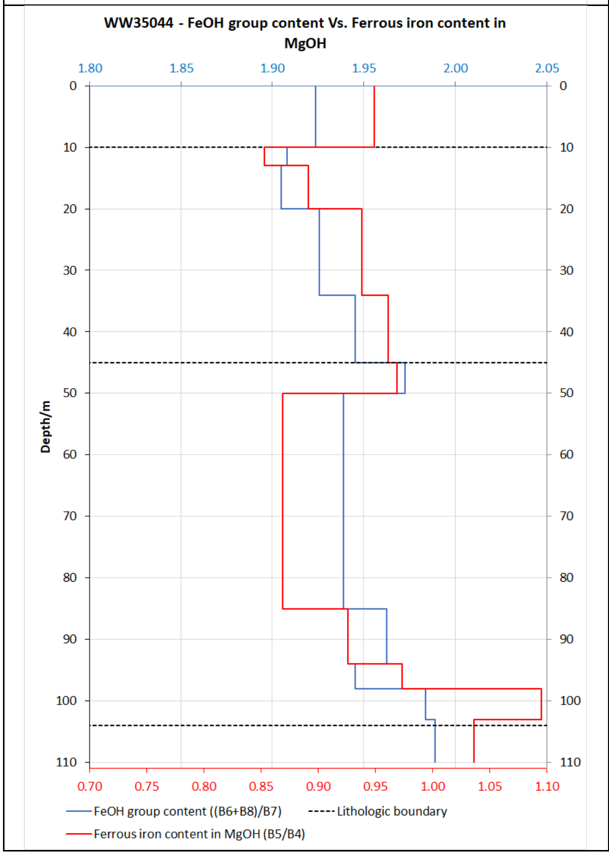

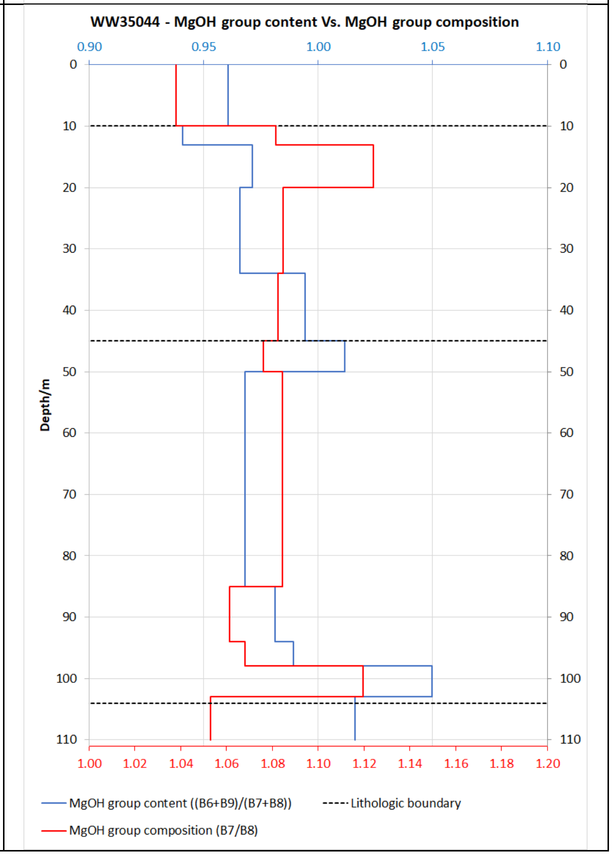

ANNEX 3 – BOREHOLE BAND RATIO COMBINATION GRAPHS

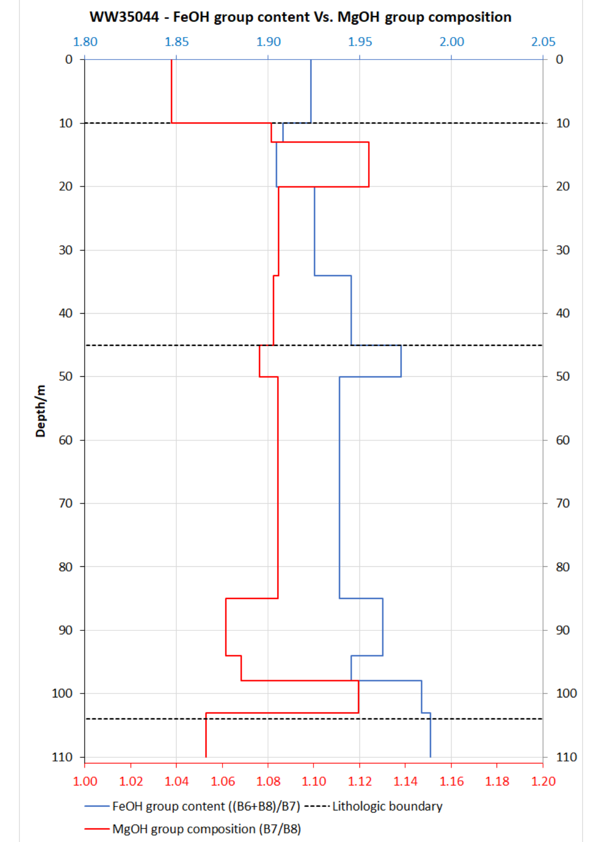

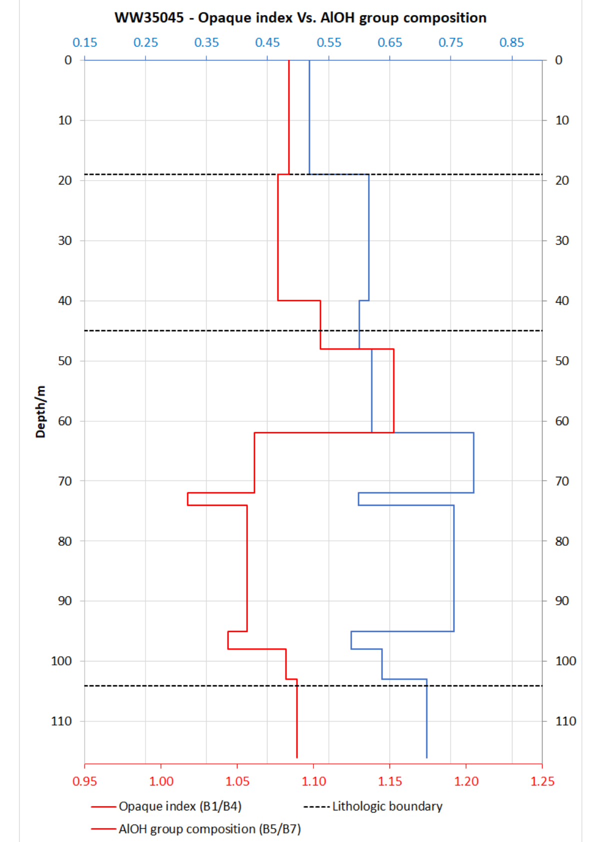

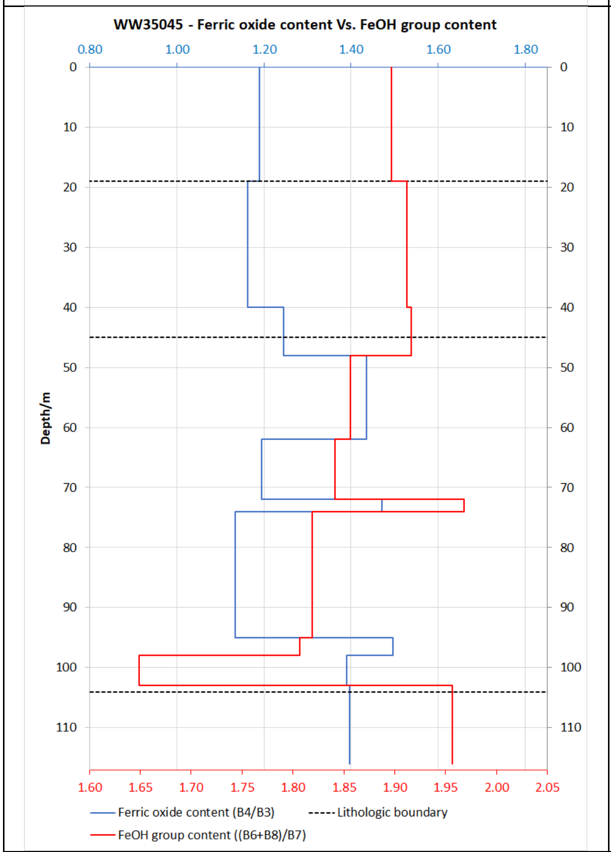

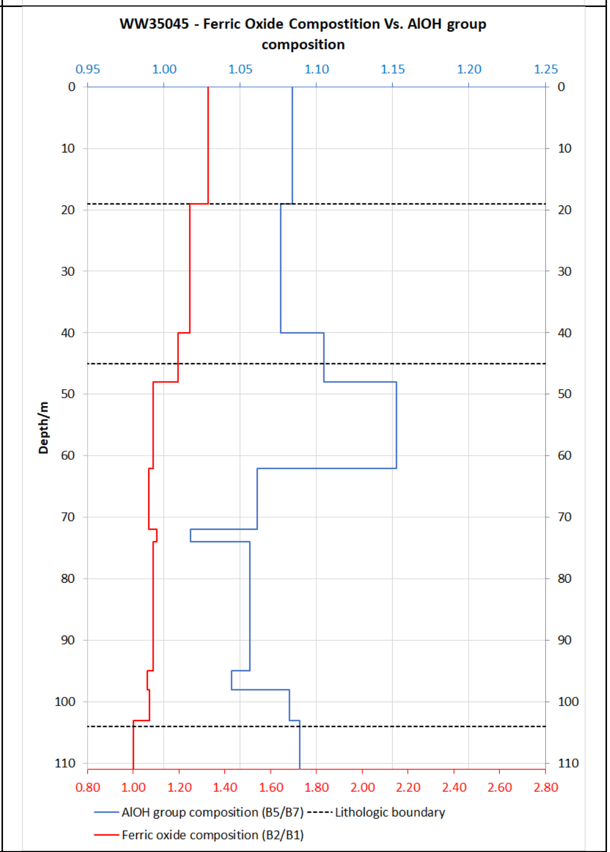

ANNEX 3 – BOREHOLE BAND RATIO COMBINATION GRAPHS

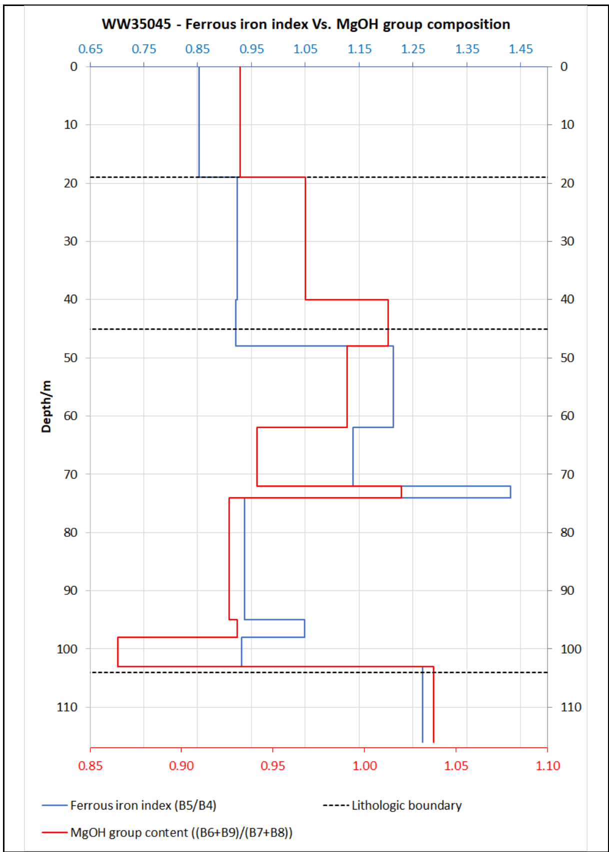

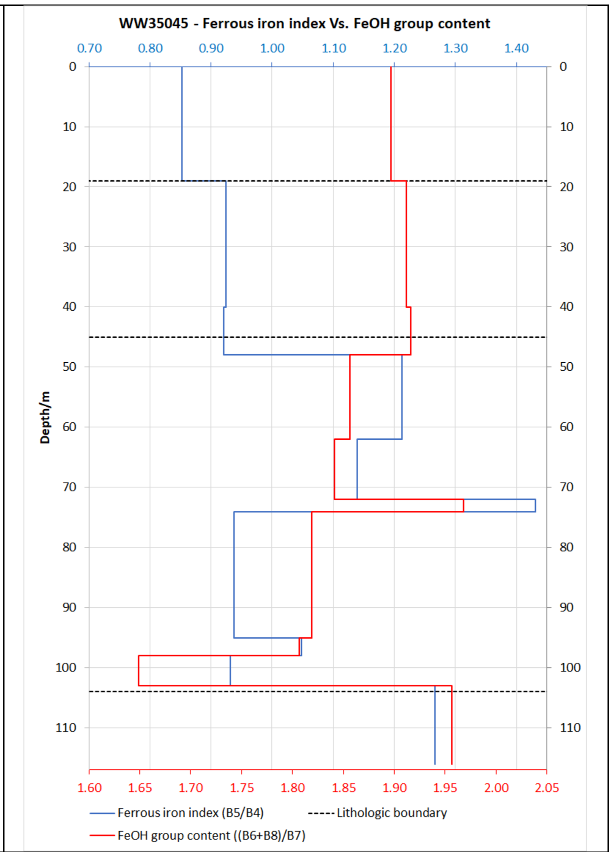

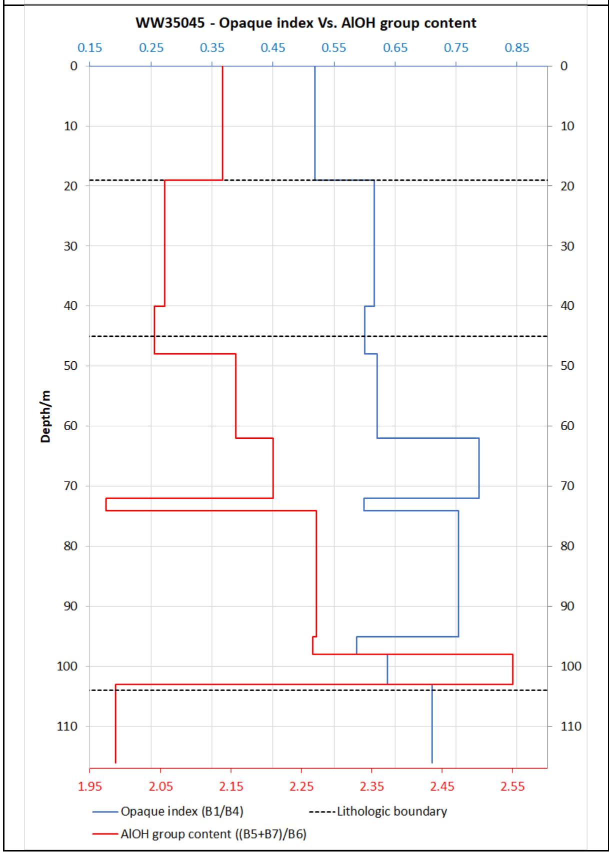

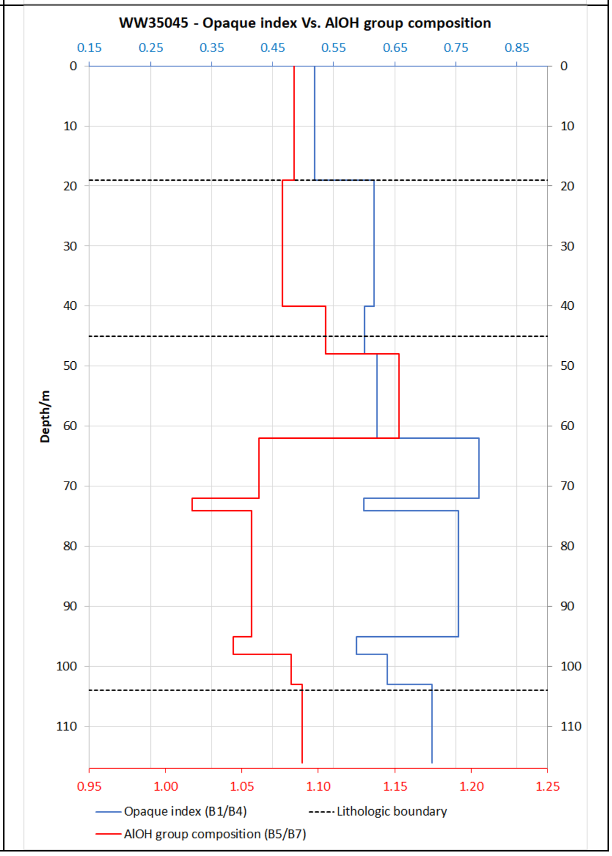

ANNEX 3 – BOREHOLE BAND RATIO COMBINATION GRAPHS

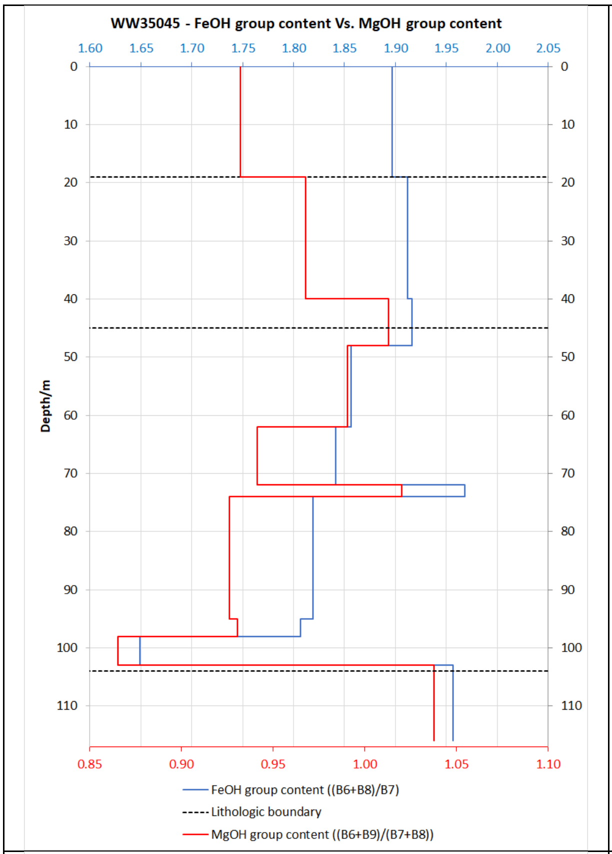

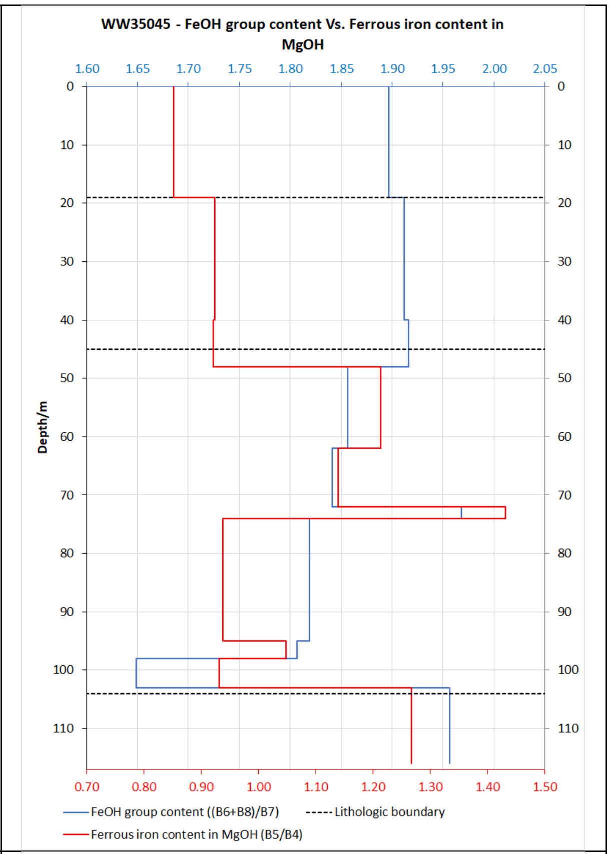

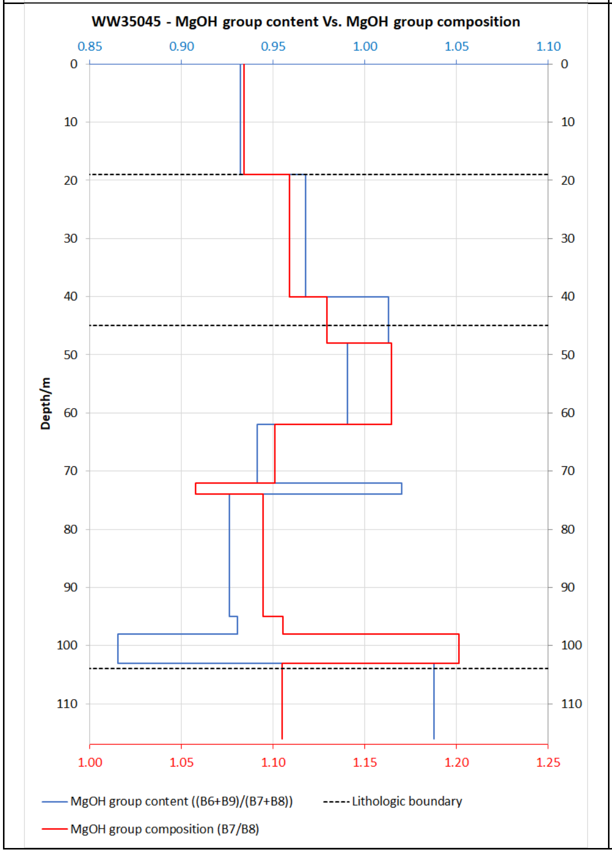

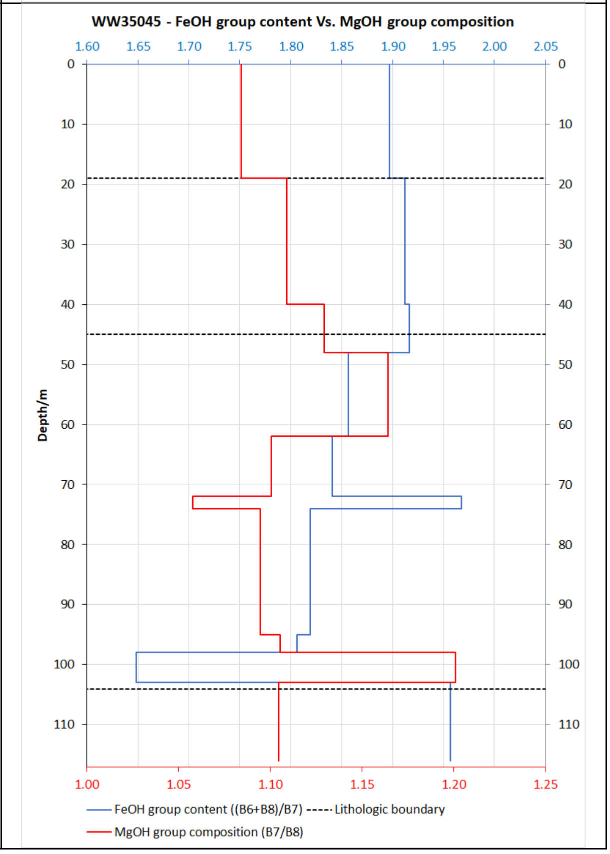

ANNEX 4 – DEPTH RANGE EULER DECONVOLUTION MAPS

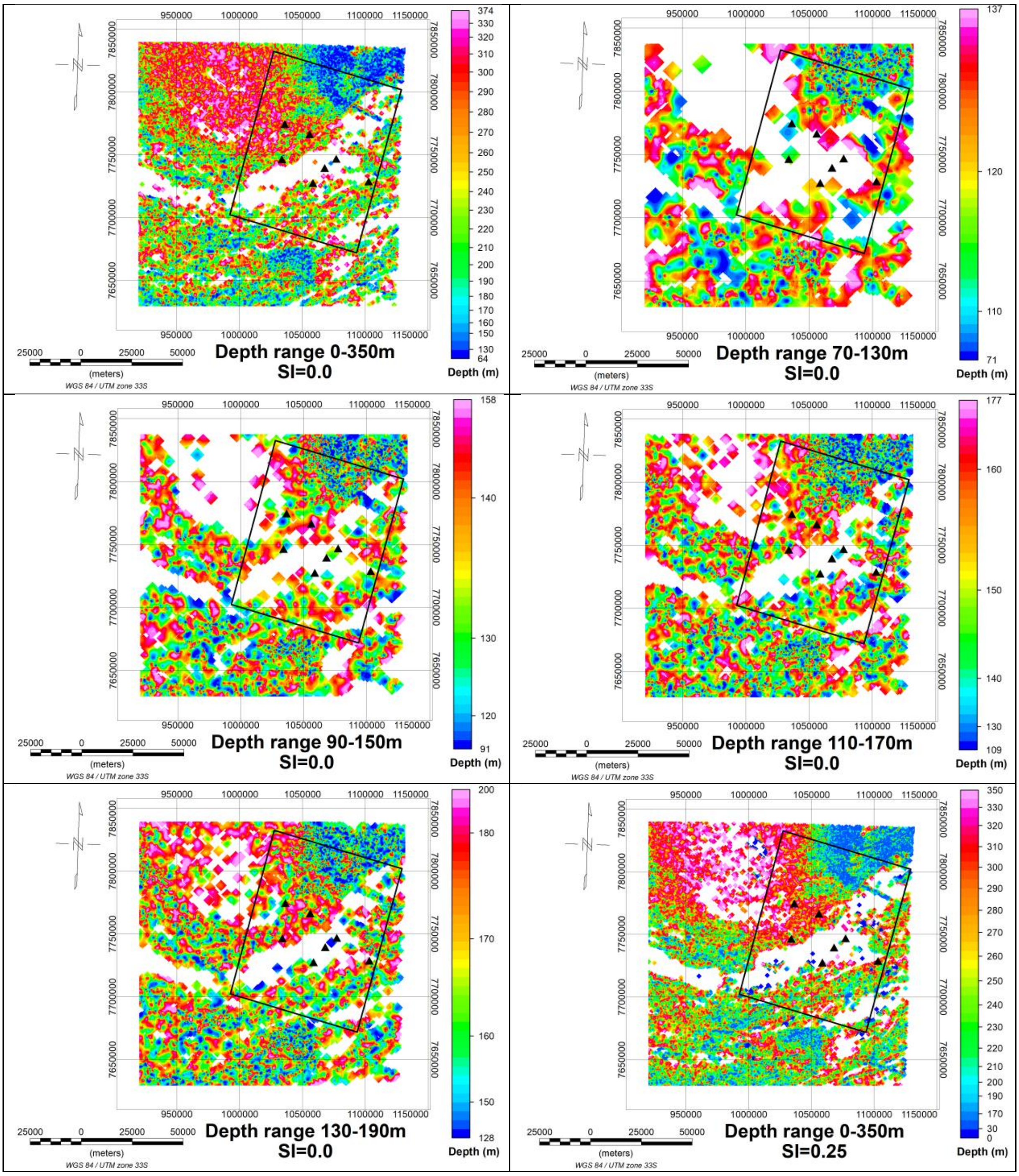

ANNEX 4 – DEPTH RANGE EULER DECONVOLUTION MAPS

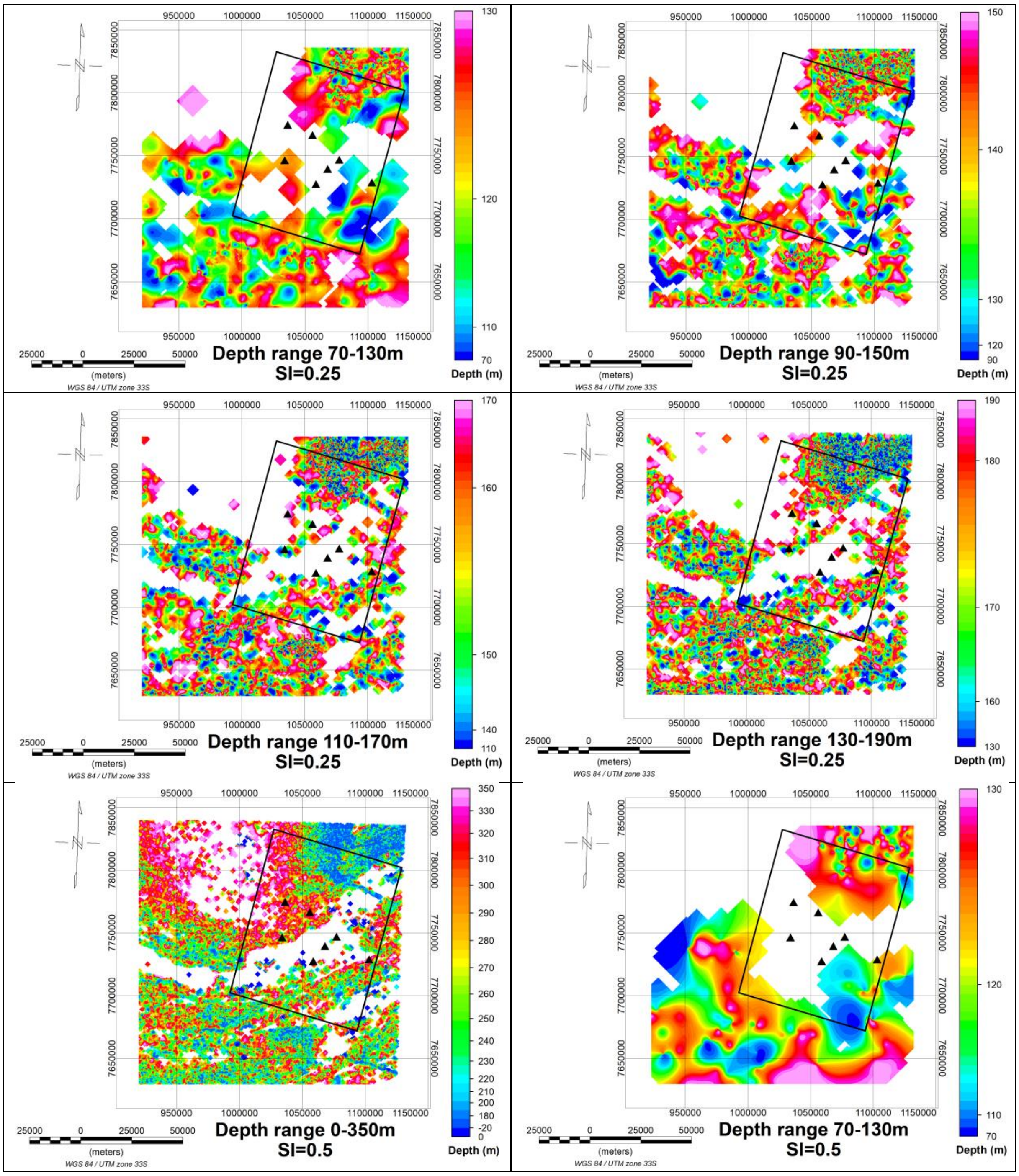

ANNEX 4 – DEPTH RANGE EULER DECONVOLUTION MAPS

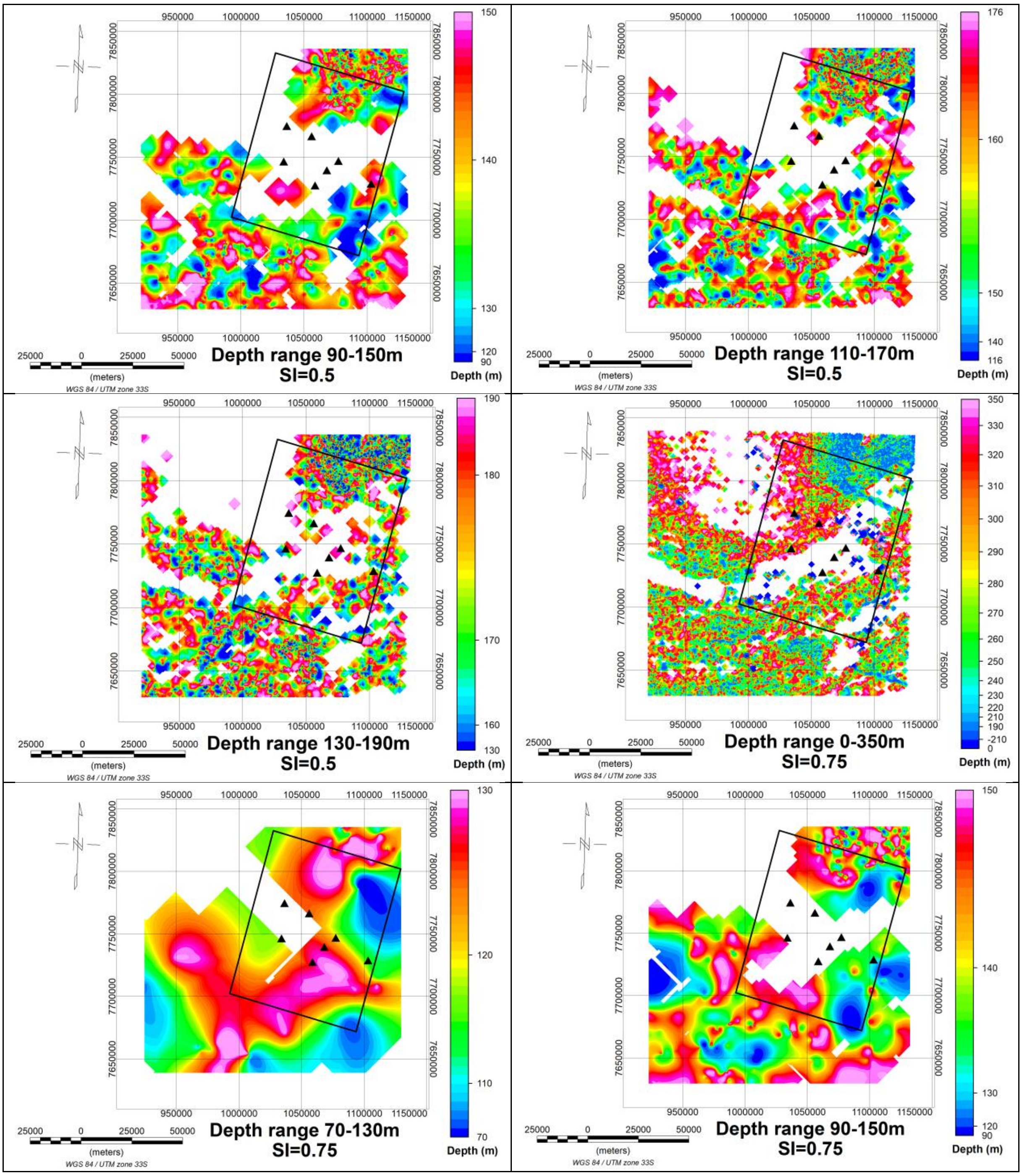

ANNEX 4 – DEPTH RANGE EULER DECONVOLUTION MAPS